

## **Laser Medicine and Biomedical Optical Imaging**

### **RLE Groups**

Optics and Quantum Electronics Group

### **Academic Staff**

Professor James G. Fujimoto

### **Research Staff and Visiting Scientists**

Dr. Yu Chen, Dr. Iwona Gorczynska, Dr. Robert Huber (Ludwig Maximilians University, Munich, Germany)

### **Scientific Collaborators**

Dr. Peter M. Andrews (Georgetown University), Dr. David Boas (Massachusetts General Hospital), Dr. Sven Bursell (Joslin Diabetes Center), Alex Cable (Thorlabs, Inc.), Royce Chen (New England Eye Center), Dr. Alan Clermont (Joslin Diabetes Center), Dr. James Connolly (Beth Israel Deaconess Medical Center), Dr. Anna Devor (Massachusetts General Hospital), Dr. Jay Duker (New England Eye Center), Dr. Edward Feener (Joslin Diabetes Center), Dr. James Jiang (Thorlabs, Inc.), Dr. Hiroshi Mashimo (Veteran's Administration Boston Medical Center), Brian Monson (New England Eye Center), Lana Ruvinskaya (Massachusetts General Hospital), Dr. Joseph Schmitt (LightLab Imaging), Dr. Joel Schuman (University of Pittsburgh Medical Center)

### **Graduate Students**

Desmond C. Adler, Aaron D. Aguirre, Shu-Wei Huang, Jonathan J. Liu, Vivek J. Srinivasan

### **Technical and Support Staff**

Dorothy A. Fleischer, Donna L. Gale

### **Research Areas and Projects**

1. Optical coherence tomography (OCT) technology
  - 1.1 Ultrahigh resolution OCT
  - 1.2 High speed OCT using Fourier domain detection
    - 1.2.1 Spectral domain OCT
    - 1.2.2 Swept source OCT imaging
2. Ophthalmic OCT
  - 2.1 Technology for clinical ophthalmic OCT
  - 2.2 Ultrahigh resolution OCT study of retinal pathologies
  - 2.3 Three-dimensional visualization methods for ophthalmic imaging
  - 2.4 Small animal retinal imaging
  - 2.5 Swept source/Fourier domain OCT retinal imaging
3. Optical Biopsy using OCT
  - 3.1 Ultrahigh-speed 3D endomicroscopy
  - 3.2 Endoscopic imaging of Barrett's esophagus
  - 3.3 OCT imaging of kidney microanatomy ex vivo
4. Optical Coherence Microscopy (OCM)
  - 4.1 Swept-source OCM
  - 4.2 Line-scanning optical coherence microscopy (OCM)
5. Functional brain imaging with OCT

## 1. Optical Coherence Tomography (OCT) Technology

### Sponsors

Air Force Office of Scientific Research - FA9550-040-1-0011, FA9550-040-1-0046  
National Institutes of Health - RO1-EY011289-21, RO1-CA75289-08  
National Science Foundation - BES-0522845, ECS-0501478, BES-0119494, ECS-0119452  
German Research Foundation (DFG) – HU 1006/1-1  
Natural Sciences and Engineering Research Council of Canada – CGS D2-331643-2006  
The Whitaker Foundation

### Project Staff

Prof. James G. Fujimoto, Dr. Yu Chen, Dr. Iwona Gorczynska, Dr. Robert Huber (Ludwig Maximilians University, Munich, Germany), Alex Cable (Thorlabs Inc.), Dr. James Jiang (Thorlabs Inc), Dr. Joseph Schmitt (LightLab Imaging), Desmond C. Adler, Aaron D. Aguirre, Shu-Wei Huang, Jonathan Liu, Vivek J. Srinivasan

Optical coherence tomography (OCT) is an emerging medical imaging and diagnostic technology, developed by our research group and collaborators in 1991 [1]. Since then, OCT has been investigated for applications in many biomedical areas [2]. OCT enables the visualization of tissue microstructure *in situ* and in real time with resolutions in the range of 1-10  $\mu\text{m}$ , approaching to that of histopathology. Previous studies have demonstrated that changes in tissue architectural morphology associated with neoplasia can be identified [3-6]. Clinical OCT systems often use superluminescent diodes (SLDs) that enable imaging with 10-15  $\mu\text{m}$  axial resolution. These resolutions are typically insufficient for identifying neoplastic changes for cancer detection or tissue morphological and structural features for the visualization of other pathologies. Advances in solid-state lasers and nonlinear fiber technology have enabled the development of ultrahigh resolution and spectroscopic OCT techniques that promise to improve tissue differentiation and image contrasts. The recent development of Fourier domain OCT techniques (spectral OCT and swept source OCT) enables high speed three-dimensional imaging of biological tissues *in vivo*, which has strong potential for imaging large tissue volumes for clinical diagnosis.

### 1.1 Ultrahigh-Resolution OCT

The axial resolutions of conventional OCT imaging studies are typically in the range of 10-15  $\mu\text{m}$ . Our group pioneered the development of ultrahigh-resolution OCT imaging, achieving axial resolutions  $\sim 3$   $\mu\text{m}$  in the human eye and  $\sim 1$   $\mu\text{m}$  in other applications [6-8]. The axial resolution in OCT images is inversely proportional to the optical bandwidth and proportional to the square of the central wavelength of the light source. Enhancing the resolution of OCT images continues to be a very active field of research [2, 9]. Ultrahigh resolution OCT requires extremely broad bandwidths because of the  $\lambda^2/\Delta\lambda$  dependence, where  $\Delta\lambda$  is the bandwidth and  $\lambda_0$  is the median wavelength of the light source. This is particularly the case for the spectral region between 1.0  $\mu\text{m}$  and 1.5  $\mu\text{m}$ . This spectral region is of great interest for OCT research because of the high penetration depth in biological tissue and the possibility to perform spectroscopic OCT imaging of functional parameters such as water content and tissue oxygenation [10].

In order to achieve high resolution, broad bandwidth light sources are required. Superluminescent diode light sources are commonly used in OCT because of their compact size and low cost. However, traditional superluminescent diode light sources have limited bandwidths and axial image resolutions are typically 10  $\mu\text{m}$ . Femtosecond lasers are ideal light sources for ultrahigh-resolution OCT because they can generate the extremely broad bandwidths necessary for ultrahigh-resolution imaging. Previously, we demonstrated OCT imaging with resolutions of 1  $\mu\text{m}$  at 800 nm and 5.1  $\mu\text{m}$  at 1300 nm in biological tissue by using solid-state mode-locked lasers as well as nonlinear fiber sources [7, 11, 12]. We have investigated compact, portable light sources for ultrahigh resolution OCT imaging at wavelengths of 890 nm, 1300 nm, and 1500 nm to enable more widespread ultrahigh resolution and spectroscopic OCT imaging to be performed

in clinical settings [13, 14]. Recently, we demonstrated OCT imaging with  $< 5 \mu\text{m}$  resolution in tissue at 1300 nm and  $< 3 \mu\text{m}$  resolution at 800 nm using continuum generation in a single photonic crystal fiber with a parabolic dispersion profile and two closely spaced zero dispersion wavelengths [15].

## 1.2 High speed OCT using Fourier domain detection

Conventional OCT systems perform measurements of the echo time delay of backscattered or backreflected light by using an interferometer with a mechanically scanned optical reference path [1, 16, 17]. Measurements of the echo delay and magnitude of light are performed by mechanically scanning the reference path length, so that light echoes with sequentially different delays are detected at different times as this reference path length is scanned. Hence, these systems are known as "time domain" systems. Recently, novel OCT detection techniques have emerged which do not require mechanical scanning and achieve very high detection sensitivities enabling OCT imaging with a  $\sim 15$  to  $50\times$  increase in imaging speed over standard resolution OCT systems and  $\sim 100\times$  over conventional ultrahigh-resolution OCT systems. These "Fourier/spectral" domain techniques measure the echo time delay of light by Fourier transforming the interference spectrum of the light signal. [18, 19] Different echo time delays of light produce different frequencies of fringes in the interference spectrum. Fourier domain OCT (FdOCT) offers significantly improved sensitivity and imaging speed compared to time domain OCT [20-22]. Fourier domain OCT detection can be performed in two ways: spectral OCT using a spectrometer with a multichannel analyzer [18, 19, 23-25] or swept source OCT using a rapidly tunable laser source [1, 26-30].

Spectral and swept source OCT are especially promising for ultrahigh resolution ophthalmic imaging because they overcome imaging speed limitations of time domain OCT. Therefore, it is possible to use these techniques to form 3-dimensional maps of the macula and optic disk [31, 32]. This also enables cross-registration of three-dimensional data sets with fundus photographs, for more accurate diagnosis of disease and evaluation of treatment. In addition, Fourier domain OCT has the advantage of providing direct access to the spectral fringe pattern, enabling a wide range of novel applications. Fourier domain OCT can be used for absorption measurement [33], Doppler techniques can be used to image blood flow [34, 35], and the complex Fourier domain signal can be directly measured to double the axial measurement scan range [23, 36]. In addition spectral domain and swept source OCT are especially well suited for numerical dispersion compensation. Numerical dispersion compensation is especially powerful for applications such as ultrahigh resolution retinal imaging, because variations in eye length between different subjects can cause dispersion mismatch and therefore resolution loss.

## References

- [1] D. Huang, E. A. Swanson, C. P. Lin, J. S. Schuman, W. G. Stinson, W. Chang, M. R. Hee, T. Flotte, K. Gregory, C. A. Puliafito, and J. G. Fujimoto, "Optical Coherence Tomography," *Science*, vol. 254, pp. 1178-1181, Nov 22 1991.
- [2] J. G. Fujimoto, "Optical coherence tomography for ultrahigh resolution in vivo imaging," *Nature Biotechnology*, vol. 21, pp. 1361-1367, Nov 2003.
- [3] J. G. Fujimoto, M. E. Brezinski, G. J. Tearney, S. A. Boppart, B. Bouma, M. R. Hee, J. F. Southern, and E. A. Swanson, "Optical biopsy and imaging using optical coherence tomography," *Nature Medicine*, vol. 1, pp. 970-972, Sep 1995.
- [4] M. E. Brezinski, G. J. Tearney, B. E. Bouma, J. A. Izatt, M. R. Hee, E. A. Swanson, J. F. Southern, and J. G. Fujimoto, "Optical coherence tomography for optical biopsy. Properties and demonstration of vascular pathology," *Circulation*, vol. 93, pp. 1206-13, Mar 15 1996.
- [5] J. G. Fujimoto, C. Pitris, S. A. Boppart, and M. E. Brezinski, "Optical coherence tomography: an emerging technology for biomedical imaging and optical biopsy," *Neoplasia*, vol. 2, pp. 9-25, Jan-Apr 2000.

- [6] W. Drexler, U. Morgner, R. K. Ghanta, F. X. Kärtner, J. S. Schuman, and J. G. Fujimoto, "Ultra-high-resolution ophthalmic optical coherence tomography," *Nature Medicine*, vol. 7, pp. 502-507, Apr 2001.
- [7] W. Drexler, U. Morgner, F. X. Kartner, C. Pitris, S. A. Boppart, X. D. Li, E. P. Ippen, and J. G. Fujimoto, "In vivo ultra-high-resolution optical coherence tomography," *Optics Letters*, vol. 24, pp. 1221-1223, Sept 1 1999.
- [8] W. Drexler, H. Sattmann, B. Hermann, T. H. Ko, M. Stur, A. Unterhuber, C. Scholda, O. Findl, M. Wirtitsch, J. G. Fujimoto, and A. F. Fercher, "Enhanced visualization of macular pathology with the use of ultra-high-resolution optical coherence tomography," *Archives of Ophthalmology*, vol. 121, pp. 695-706, May 2003.
- [9] W. Drexler, "Ultra-high-resolution optical coherence tomography," *Journal of Biomedical Optics*, vol. 9, pp. 47-74, Jan 2004.
- [10] U. Morgner, W. Drexler, F. X. Kartner, X. D. Li, C. Pitris, E. P. Ippen, and J. G. Fujimoto, "Spectroscopic optical coherence tomography," *Optics Letters*, vol. 25, pp. 111-113, Jan 15 2000.
- [11] B. Bouma, G. J. Tearney, S. A. Boppart, M. R. Hee, M. E. Brezinski, and J. G. Fujimoto, "High-resolution optical coherence tomographic imaging using a mode-locked Ti:Al<sub>2</sub>O<sub>3</sub> laser source," *Optics Letters*, vol. 20, pp. 1486-1488, July 1 1995.
- [12] I. Hartl, X. D. Li, C. Chudoba, R. K. Hganta, T. H. Ko, J. G. Fujimoto, J. K. Ranka, and R. S. Windeler, "Ultra-high-resolution optical coherence tomography using continuum generation in an air-silica microstructure optical fiber," *Optics Letters*, vol. 26, pp. 608-610, May 1 2001.
- [13] P.-L. Hsiung, Y. Chen, T. H. Ko, J. G. Fujimoto, C. J. S. de Matos, S. V. Popov, J. R. Taylor, and V. P. Gapontsev, "Optical coherence tomography using a continuous-wave, high-power, Raman continuum light source," *Optics Express*, vol. 12, Nov 1 2004.
- [14] N. Nishizawa, Y. Chen, P. Hsiung, E. P. Ippen, and J. G. Fujimoto, "Real-time, ultra-high-resolution, optical coherence tomography with an all-fiber, femtosecond fiber laser continuum at 1.5 microm," *Opt Lett*, vol. 29, pp. 2846-8, Dec 15 2004.
- [15] A. D. Aguirre, N. Nishizawa, J. G. Fujimoto, W. Seitz, M. Lederer, and D. Kopf, "Continuum generation in a novel photonic crystal fiber for ultra-high resolution optical coherence tomography at 800 nm and 1300 nm," *Optics Express*, vol. 14, pp. 1145-1160, Feb 6 2006.
- [16] E. A. Swanson, J. A. Izatt, M. R. Hee, D. Huang, C. P. Lin, J. S. Schuman, C. A. Puliafito, and J. G. Fujimoto, "In vivo retinal imaging by optical coherence tomography," *Optics Letters*, vol. 18, pp. 1864-1866, Nov 1 1993.
- [17] M. R. Hee, J. A. Izatt, E. A. Swanson, D. Huang, J. S. Schuman, C. P. Lin, C. A. Puliafito, and J. G. Fujimoto, "Optical coherence tomography of the human retina," *Archives of Ophthalmology*, vol. 113, pp. 325-332, Mar 1995.
- [18] A. F. Fercher, C. K. Hitzenberger, G. Kamp, and S. Y. Elzaiat, "Measurement of Intraocular Distances by Backscattering Spectral Interferometry," *Optics Communications*, vol. 117, pp. 43-48, May 15 1995.
- [19] G. Hausler and M. W. Lindner, "'Coherence radar" and "spectral radar"-new tools for dermatological diagnosis," *Journal of Biomedical Optics*, vol. 3, pp. 21-31, 1998/01/ 1998.
- [20] R. Leitgeb, C. K. Hitzenberger, and A. F. Fercher, "Performance of Fourier domain vs. time domain optical coherence tomography," *Optics Express*, vol. 11, pp. 889-894, Apr 21 2003.
- [21] M. A. Choma, M. V. Sarunic, C. H. Yang, and J. A. Izatt, "Sensitivity advantage of swept source and Fourier domain optical coherence tomography," *Optics Express*, vol. 11, pp. 2183-2189, Sep 8 2003.
- [22] J. F. de Boer, B. Cense, B. H. Park, M. C. Pierce, G. J. Tearney, and B. E. Bouma, "Improved signal-to-noise ratio in spectral-domain compared with time-domain optical coherence tomography," *Optics Letters*, vol. 28, pp. 2067-2069, Nov 1 2003.
- [23] M. Wojtkowski, R. Leitgeb, A. Kowalczyk, T. Bajraszewski, and A. F. Fercher, "In vivo human retinal imaging by Fourier domain optical coherence tomography," *Journal of Biomedical Optics*, vol. 7, pp. 457-463, July 2002.

- [24] M. Wojtkowski, T. Bajraszewski, P. Targowski, and A. Kowalczyk, "Real-time in vivo imaging by high-speed spectral optical coherence tomography," *Optics Letters*, vol. 28, pp. 1745-1747, Oct 1 2003.
- [25] M. Wojtkowski, V. J. Srinivasan, T. H. Ko, J. G. Fujimoto, A. Kowalewicz, and J. S. Duker, "Ultrahigh resolution, high speed, Fourier domain optical coherence tomography and methods for dispersion compensation," *Optics Express*, vol. 12, pp. 2404-2422, May 2004.
- [26] S. R. Chinn, E. A. Swanson, and J. G. Fujimoto, "Optical coherence tomography using a frequency-tunable optical source," *Optics Letters*, vol. 22, pp. 340-342, Mar 1 1997.
- [27] B. Golubovic, B. E. Bouma, G. J. Tearney, and J. G. Fujimoto, "Optical frequency-domain reflectometry using rapid wavelength tuning of a Cr<sup>4+</sup>:forsterite laser," *Optics Letters*, vol. 22, pp. 1704-1706, Nov 15 1997.
- [28] S. H. Yun, C. Boudoux, M. C. Pierce, J. F. de Boer, G. J. Tearney, and B. E. Bouma, "Extended-cavity semiconductor wavelength-swept laser for biomedical imaging," *IEEE Photonics Technology Letters*, vol. 16, pp. 293-5, 2004/01/ 2004.
- [29] S. H. Yun, C. Boudoux, G. J. Tearney, and B. E. Bouma, "High-speed wavelength-swept semiconductor laser with a polygon-scanner-based wavelength filter," *Optics Letters*, vol. 28, pp. 1981-1983, Oct 15 2003.
- [30] R. Huber, D. C. Adler, and J. G. Fujimoto, "Buffered Fourier Domain Mode Locking (FDML): Unidirectional swept laser sources for OCT imaging at 370,000 lines per second," *Optics Letters*, vol. 31, pp. 2975-2977, October 15 2006.
- [31] M. Wojtkowski, T. Bajraszewski, I. Gorczynska, P. Targowski, A. Kowalczyk, W. Wasilewski, and C. Radzewicz, "Ophthalmic imaging by spectral optical coherence tomography," *Am J Ophthalmol*, vol. 138, pp. 412-9, Sep 2004.
- [32] N. A. Nassif, B. Cense, B. H. Park, M. C. Pierce, S. H. Yun, B. E. Bouma, G. J. Tearney, T. C. Chen, and J. F. de Boer, "In vivo high-resolution video-rate spectral-domain optical coherence tomography of the human retina and optic nerve," *Optics Express*, vol. 12, 2004/02/09 2004.
- [33] R. Leitgeb, M. Wojtkowski, A. Kowalczyk, C. K. Hitzenberger, M. Sticker, and A. F. Fercher, "Spectral measurement of absorption by spectroscopic frequency-domain optical coherence tomography," *Optics Letters*, vol. 25, pp. 820-2, 2000/06/01 2000.
- [34] B. R. White, M. C. Pierce, N. Nassif, B. Cense, B. H. Park, G. J. Tearney, B. E. Bouma, T. C. Chen, and J. F. de Boer, "In vivo dynamic human retinal blood flow imaging using ultra-high-speed spectral domain optical Doppler tomography," *Optics Express*, vol. 11, pp. 3490-3497, Dec 15 2003.
- [35] R. A. Leitgeb, L. Schmetterer, W. Drexler, A. F. Fercher, R. J. Zawadzki, and T. Bajraszewski, "Real-time assessment of retinal blood flow with ultrafast acquisition by color Doppler Fourier domain optical coherence tomography," *Optics Express*, vol. 11, pp. 3116-3121, Nov 17 2003.
- [36] P. Targowski, M. Wojtkowski, A. Kowalczyk, T. Bajraszewski, M. Szkulmowski, and W. Gorczynska, "Complex spectral OCT in human eye imaging in vivo," *Optics Communications*, vol. 229, pp. 79-84, Jan 2 2004.

### 1.2.1 Spectral Domain OCT

Spectral domain detection techniques measure the echo time delay of light by using an interferometer with a broadband light source and a spectrometer with a multichannel analyzer. The spectrum of the interferometer output is acquired and processed. [1-5] Backreflections or backscattering from the tissue at different delays produces oscillations or fringes in the interference spectrum. Increasing delay differences produce higher frequency oscillations. The magnitude and delay of the light from the tissue can be measured by Fourier transforming the interference spectrum. In a spectral detection, the sensitivity, or one over the smallest detectable reflection,  $R_S$ , is given by:  $1/R_S = \eta P T_{exp} / (h\nu)$ , where  $P$  is the source power,  $T_{exp}$  is the exposure time,  $\eta$  is the detection efficiency, and  $h\nu$  is the photon energy. With spectral detection, the exposure time is approximately the axial scan time  $T_{A-scan}$ , therefore  $T_{A-scan} \approx T_{exp}$ . In conventional

time domain OCT, light from different time delays is detected sequentially, so assuming an axial scan time of  $T_{A-scan}$ , the exposure time is approximately  $T_{A-scan} / M$ , where  $M$  is the number of resolvable elements in one axial scan, defined as the total axial measurement range divided by the axial resolution. Because light exposure levels in the eye are limited, the imaging speed possible with a time domain detection system is limited by the minimum sensitivity required for good image quality. Spectral domain OCT does not have this limitation, thus making it possible to image with ultrahigh resolution and high speed. Therefore, spectral domain detection has a sensitivity advantage proportional to the number of resolvable elements in an axial scan. This sensitivity advantage is typically  $\sim 30$  dB, enabling dramatic increases in imaging speeds [1, 6-9]. With shorter exposure times, spectral domain OCT is less sensitive to subject motion than conventional time domain OCT.

Using these latest technological advances in OCT, we have designed and constructed a portable, high-speed ultrahigh resolution spectral OCT system which can achieve axial image resolution of  $\sim 3$   $\mu\text{m}$  and can perform high-speed, video-rate OCT imaging in the ophthalmology clinic. This high-speed UHR-OCT prototype can be operated using either a femtosecond laser or a broadband superluminescent SLD as imaging light source. In our early studies, we developed a low threshold femtosecond Ti:Sapphire laser that was used in the ophthalmology clinic for a period of three years. However, recent advances in multiplexed SLD light sources enable image resolutions of 3.5  $\mu\text{m}$ . These broadband multiplexed SLD provides an easy to operate and relatively inexpensive light source for clinical UHR-OCT imaging. The combination of high image acquisition speed and ultrahigh OCT axial resolution promises to yield significant improvements in the clinical utility of high-speed ultrahigh resolution OCT systems over currently available prototype and commercial OCT systems.

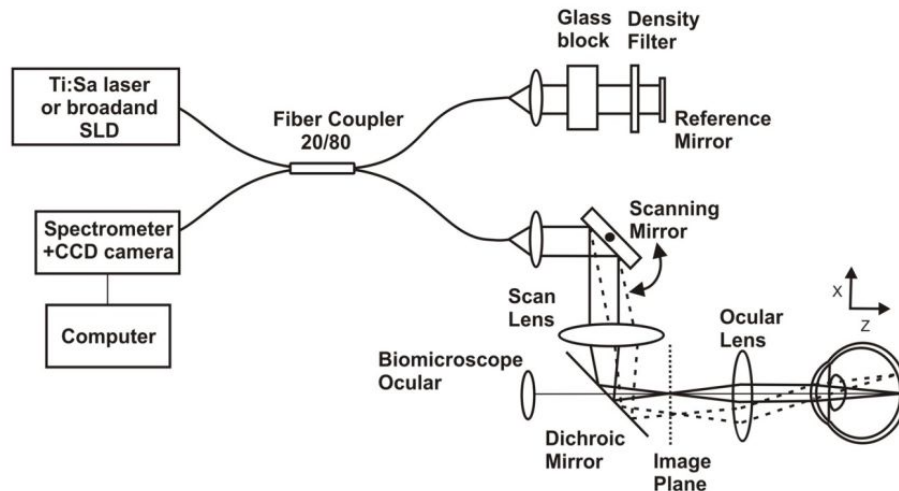


**Figure 1.1.** Schematic diagram of high-speed ophthalmic OCT instrument using Fourier domain detection.

Figure 1.1 shows a schematic of the high-speed, UHR-OCT ophthalmic system using spectral/Fourier domain detection [5]. Light from a broadband light source is split between the sample and reference arms of an interferometer. Light in the reference arm is attenuated and reflected from a stationary mirror at a fixed delay. Light in the sample arm is directed through two galvanometer-actuated steering mirrors and relay imaged through the pupil onto the retina. The transverse spot size on the retina is estimated to be 20  $\mu\text{m}$ , but depends on factors such as aberrations and refractive powers of different eyes. The galvanometer actuated mirrors can scan the OCT beam across the retina in any arbitrary pattern in order to perform cross-sectional imaging [10]. Cross sectional OCT data was acquired by scanning the OCT beam on the retina under computer control. The incident light power on the eye is 750  $\mu\text{W}$ , the same exposure used in commercial ophthalmic OCT systems and consistent with ANSI safety standards. The

spectrum of the interferometer output is detected using a spectrometer consisting of a collimating lens, transmission grating, imaging lens, and CCD line scan camera. The interference spectrum data from the camera was transferred to computer system memory where it was rescaled from wavelength to frequency and Fourier transformed to generate axial measurements of the echo delay and magnitude of light from the retina. An example of clinical imaging using the high speed, ultrahigh resolution OCT instrument with spectral detection is shown in Figure 1.2.

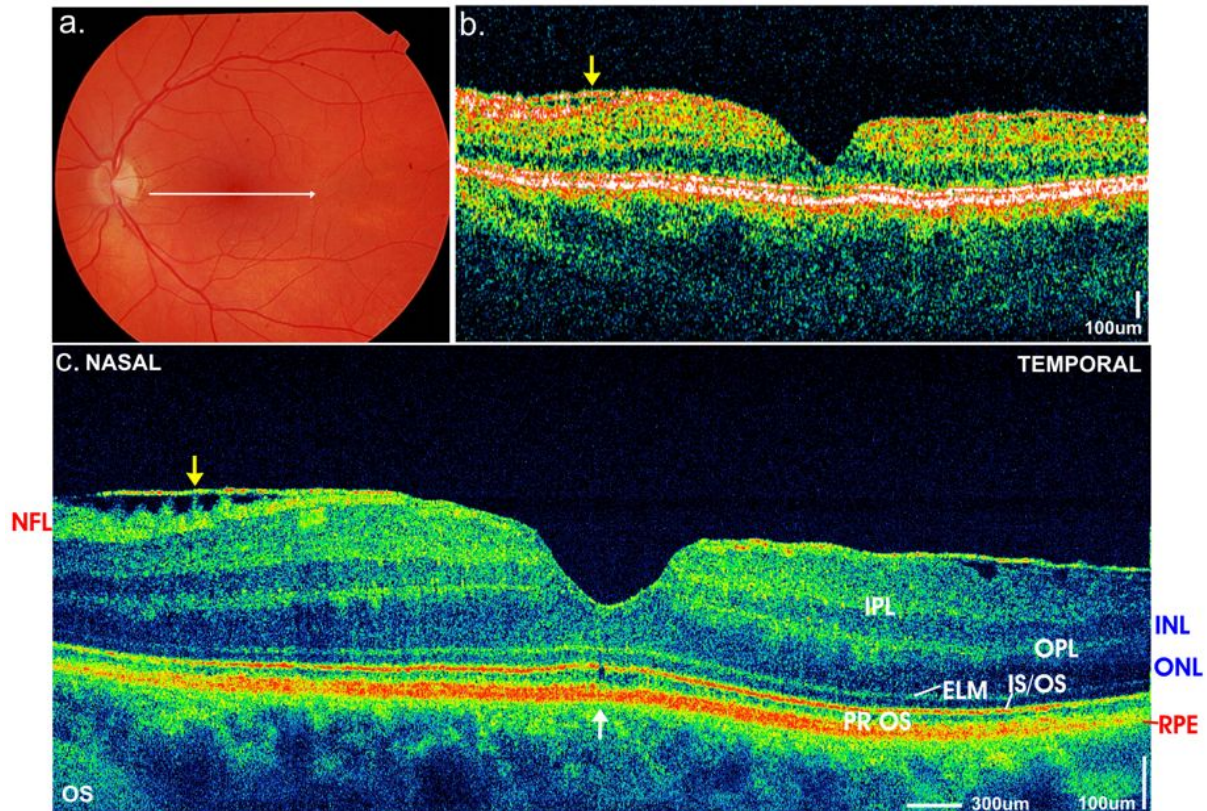


**Figure 1.2.** Macular hole repair: fundus photo (left top), cross-sectional image obtained by commercial instrument – Zeiss Stratus OCT (top right), cross-sectional image obtained by high speed, ultrahigh resolution OCT instrument. The high quality image consists of 8100 axial scans (transverse pixels) with 1024 points (axial pixels) per scan and was measured in 0.35 sec. NFL – nerve fiber layer, IPL- inner plexiform layer, INL – inner nuclear layer, OPL – outer plexiform layer, ONL – outer nuclear layer, ELM – external limiting membrane, IS/OS – inner/outer photoreceptor junction, PR OS – photoreceptor outer segments, RPE – retinal pigment epithelium.

Figure 1.2 shows a comparison of standard resolution (10  $\mu\text{m}$  resolution image from the commercial Zeiss StratusOCT instrument) and high speed, ultrahigh resolution (from our research prototype instrument) images from a 65-year-old woman two years after the surgical repair of a full-thickness macular hole in her left eye. Visual acuity had improved to 20/25 OS. Both the standard resolution StratusOCT image (Fig 1.2b) and the high-definition, 8192 axial scan, ultrahigh resolution OCT image (Fig 1.2c) depict an epiretinal membrane (yellow arrows). However, the high-definition, ultrahigh resolution OCT image enables better visualization of the membrane thickness and separation from the retina in the nasal portion of the image. A very small central disruption of the photoreceptor IS/OS junction and photoreceptor outer segments in the fovea is visualized in the high-definition ultrahigh resolution OCT image (white arrow). No such disruption is apparent in the standard resolution OCT image. This apparent disruption is

probably not a shadowing artifact, as evidenced by the absence of shadowing in the inner retina above the disruption and the fact that the retinal pigment epithelium (RPE) signal is not reduced below the disruption. This abnormality in the photoreceptor signal, along with the epiretinal membrane, may explain the patient's slight decrease in visual acuity. Small photoreceptor disruptions visualized by OCT following macular hole repair have been reported previously, and may be correlated with visual acuity. Similar outer retinal defects can improve as visual acuity improves during the postoperative period.

## References

- [1] R. Leitgeb, C. K. Hitzenberger, and A. F. Fercher, "Performance of Fourier domain vs. time domain optical coherence tomography," *Optics Express*, vol. 11, pp. 889-894, Apr 21 2003.
- [2] R. Leitgeb, M. Wojtkowski, A. Kowalczyk, C. K. Hitzenberger, M. Sticker, and A. F. Fercher, "Spectral measurement of absorption by spectroscopic frequency-domain optical coherence tomography," *Optics Letters*, vol. 25, pp. 820-2, June 1 2000.
- [3] P. Targowski, M. Wojtkowski, A. Kowalczyk, T. Bajraszewski, M. Szkulmowski, and W. Gorczynska, "Complex spectral OCT in human eye imaging in vivo," *Optics Communications*, vol. 229, pp. 79-84, Jan 2 2004.
- [4] M. Wojtkowski, A. Kowalczyk, R. Leitgeb, and A. F. Fercher, "Full range complex spectral optical coherence tomography technique in eye imaging," *Optics Letters*, vol. 27, pp. 1415-17, Aug 15 2002.
- [5] M. Wojtkowski, R. Leitgeb, A. Kowalczyk, T. Bajraszewski, and A. F. Fercher, "In vivo human retinal imaging by Fourier domain optical coherence tomography," *Journal of Biomedical Optics*, vol. 7, pp. 457-463, Jul 2002.
- [6] M. A. Choma, M. V. Sarunic, C. Yang, and J. Izatt, "Sensitivity advantage of swept source and Fourier domain optical coherence tomography," *Optics Express*, vol. 11, pp. 2183-2189, 2003.
- [7] J. F. de Boer, B. Cense, B. H. Park, M. C. Pierce, G. J. Tearney, and B. E. Bouma, "Improved signal-to-noise ratio in spectral-domain compared with time-domain optical coherence tomography," *Optics Letters*, vol. 28, pp. 2067-2069, Nov 1 2003.
- [8] M. Wojtkowski, T. Bajraszewski, P. Targowski, and A. Kowalczyk, "Real-time in vivo imaging by high-speed spectral optical coherence tomography," *Optics Letters*, vol. 28, pp. 1745-1747, Oct 1 2003.
- [9] S. H. Yun, G. J. Tearney, B. E. Bouma, B. H. Park, and J. F. de Boer, "High-speed spectral-domain optical coherence tomography at 1.3  $\mu$ m wavelength," *Optics Express*, vol. 11, pp. 3598-3604, Dec 29 2003.
- [10] M. R. Hee, J. A. Izatt, E. A. Swanson, D. Huang, J. S. Schuman, C. P. Lin, C. A. Puliafito, and J. G. Fujimoto, "Optical coherence tomography of the human retina," *Archives of Ophthalmology*, vol. 113, pp. 325-332, Mar 1995.

### 1.2.2 Swept Source OCT Imaging

Although spectral/Fourier domain OCT technology provides high-performance imaging in low-scattering organs such as the eye, these systems are limited in their application to other tissue types. The study of epithelial tissues, for example, is of great interest since many human diseases are associated with structural abnormalities of this superficial tissue layer. Epithelial tissue is the most common starting point of human cancers, and is found in the linings of hollow organs such as the colon, esophagus, lung, and breast ducts. Epithelial tissue is highly specialized for specific functions such as absorption or excretion of material, and therefore contains a high density of cellular organelles such as mitochondria, nuclei, and cellular membranes. This densely-packed architecture results in a highly scattering medium that limits the penetration depth of light as the wavelength decreases. Spectral/Fourier domain OCT systems typically employ silicon-based CCD detectors with dramatically decreased sensitivity at

wavelengths above  $\sim 1000$  nm, and are generally restricted to operation between 400–900 nm. For OCT imaging of the epithelium and its underlying supportive tissues, however, operation at wavelengths of 1000–1300 nm is desired to achieve an image penetration depth of 1–3 mm.

Fourier domain detection using frequency-swept lasers provides a powerful approach for OCT imaging that is complementary to spectral/Fourier domain detection. These so-called “swept source/Fourier domain” systems typically employ a broadband, rapid frequency-swept laser source and InGaAs photodetectors to perform Fourier domain OCT imaging without the use of a spectrometer [1-9]. Figure 1.3 illustrates the concept of swept source OCT imaging using a frequency-swept laser and a Michelson interferometer. The frequency-swept output from the laser can be thought of as a heavily chirped optical signal. The source light is split into two parts by a beamsplitter. One beam travels a fixed distance and reflects off of a reference surface, setting the reference distance for the interferometer. The other beam strikes the sample of interest, where light is backscattered from structures at various depths within the sample. Each backscattering event produces an attenuated, time-delayed copy of the incident frequency sweep, which travels back to the beamsplitter and interferes with the reference beam. This interference is measured as a function of time using a high-speed photodetector.

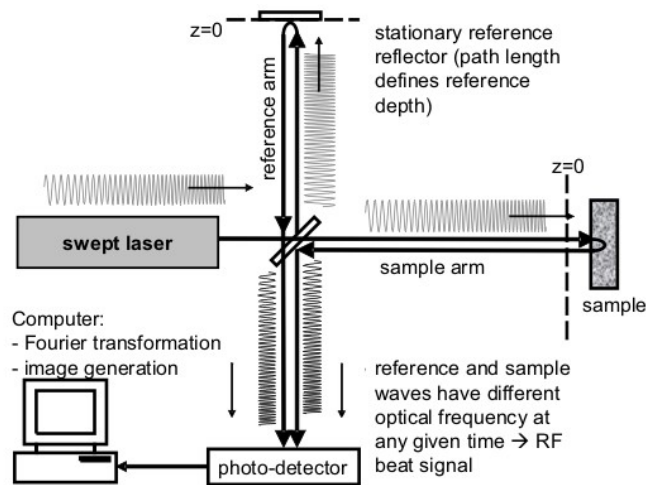


**Figure 1.3.** Principle of Fourier domain OCT imaging using a rapidly wavelength-swept laser source.

As shown in Figure 1.4, the resulting interference fringes contain radio-frequency (RF) beat frequencies that correspond to the depth of each backscattering or backreflection event. If the sample produces a single reflection, as is assumed in Fig. 1.4, a single-frequency RF modulation will be created on top of the optical carrier signal. The modulation frequency is directly proportional to the difference in optical path traveled by the sample and reference beams. The photodetector, which is sensitive to optical intensity, is typically band-limited to a few hundred MHz and therefore outputs only the RF modulation. For a biological sample, each of the numerous backscattering events within the tissue creates a unique RF modulation frequency. A computer digitizes the interference fringes detected by the photodiode and performs a Fourier transformation to generate a single axial line. The beam can be translated over the sample in order to form 2D or 3D OCT images.

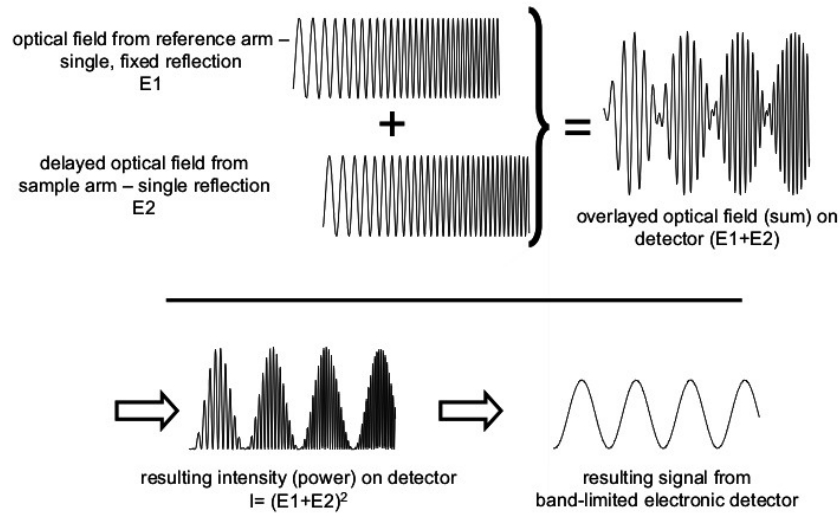


**Figure 1.4.** Generation of an interference fringe pattern from two time-delayed copies of a wavelength-swept optical waveform in a Michelson interferometer.

In practice, a fiberoptic Michelson interferometer is typically used for OCT imaging [10]. Figure 1.5 illustrates a typical swept source/Fourier domain OCT imaging setup. A small portion (~5%) of the laser output is tapped off and routed to an asymmetric Mach-Zehnder interferometer (MZI), which is used for determining the instantaneous optical frequency of the sweep. Prior to Fourier transformation to form each axial line, the interference fringes must be evenly spaced in optical frequency. The frequency sweeps of swept laser sources are not linear in time, however. Therefore the frequency spacing of the MZI fringes are analyzed and used to resample the OCT fringes onto a uniformly-spaced frequency grid [2, 11]. A highly efficient, dual-balanced Michelson interferometer is used to detect the OCT signal. In this configuration, intensity noise from the laser source is cancelled out and the effective signal level is doubled by subtracting two out-of-phase interference fringes. The sample beam is scanned over the target by a pair of XY mirrors. A 200 MS/s, 2 channel, 14-bit A/D card is synchronized to the laser sweep and is used to record the calibration and OCT signals. A computer then resamples the OCT signals, carries out a Fourier transform, and produces a final image.

Several types of frequency-swept lasers have been developed for use in OCT imaging systems. Swept lasers incorporate a tunable wavelength-selective filter element inside the cavity in order to produce a variable optical frequency over time. Two early studies were performed by our group with bulk optic designs, one using a Cr:Forsterite laser operating at 1250 nm with a sweep rate of 10 Hz [12], and another using an external cavity diode laser operating at 800 nm with a sweep rate of 2 kHz [13]. An all-fiber ring laser employing a fiber Fabry-Perot (FFP) tunable filter has been demonstrated at a sweep rate of 200 Hz [14]. Hybrid bulk optic and fiber cavity designs using a fiber-coupled semiconductor amplifier as a gain medium and a diffraction grating for wavelength selection have also been developed. For these designs, frequency sweep rates of up to 115 kHz have been achieved using a polygon rotating mirror to sweep the operating wavelength [9].

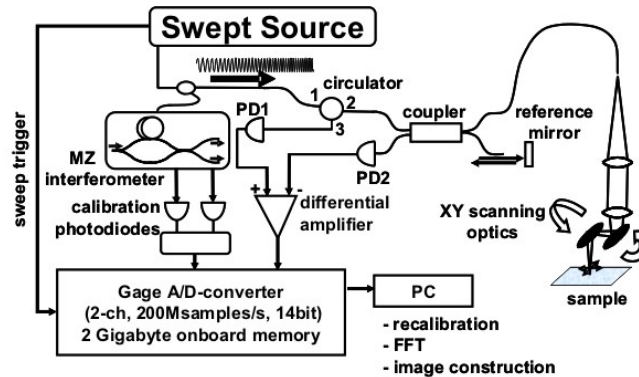


**Figure 1.5.** Schematic of OCT system used for swept source / Fourier domain imaging. MZ: Mach-Zehnder.

In swept source/Fourier domain OCT imaging, the imaging speed is equal to the sweep rates of the laser. The imaging depth and axial resolution are related to the instantaneous linewidth and total tuning range of the laser, respectively. Therefore for high-quality, high-speed OCT imaging it is desirable to possess a laser with a high sweep rate, narrow instantaneous linewidth, and broad tuning range. Recently, our lab has developed a new class of frequency-swept sources called Fourier Domain Modelocked (FDML) lasers [15-18]. These lasers precisely synchronize the wavelength selective element, typically an FFP filter, to the optical roundtrip time of the cavity. Each wavelength in the sweep perceives the filter to be stationary, allowing all of the wavelengths to build up and lase simultaneously within the cavity. This is termed “quasi-continuous wave” operation, and results in an unprecedented combination of sweep speed, instantaneous linewidth, and tuning range. Traditional swept sources, in comparison, require lasing to build up from the gain medium background every time the filter is shifted. This non-continuous operation forces a tradeoff between sweep speed and the other performance characteristics[5].

FDML lasers have been demonstrated with sweep rates of up to 370 kHz at a center wavelength of ~1300 nm, achieving OCT imaging speeds of 370,000 A-scans per second[19]. FDML lasers have also been demonstrated with sweep rates of 236 kHz at a center wavelength of ~1060 nm[18], which is useful for ophthalmic OCT imaging in the water absorption window. Sweep bandwidths are typically 100 – 170 nm (full width), giving OCT axial resolutions of 7 – 13 nm in air. At these extremely high sweep speeds, OCT imaging is limited by the photodetector bandwidths (350 MHz) and A/D rates (2 MS/s). For example, in order to perform real-time imaging at 370 kHz over a depth range of 2 mm, it is necessary to use a digital oscilloscope with a 5 GS/s acquisition rate instead of a standard analog-to-digital card in order to capture every sweep.

Swept source OCT imaging has been performed in several applications where rapid acquisition at 1300 nm is highly desirable. Figure 1.6 gives an example of OCT imaging in highly scattering human skin at 42,000 axial scans per second and 10 frames per second [19]. Excellent penetration into the tissue is evident at depths > 1 mm. Due to the high transverse line density (4096 lines per frame) and high sensitivity (96 dB) of the swept source OCT system, the image quality is very high. Rapid three dimensional imaging of epithelial tissue is also possible with FDML-based swept source OCT systems. Figure 1.7 shows several visualizations of a 3D dataset taken from a human finger tip. This 512 x 200 x 512 pixel data set was acquired at a record 370,000 axial lines per second [19] with a total acquisition time of < 0.5 sec. Other applications for high-speed three-dimensional OCT (3D-OCT) imaging include 3D optical biopsy of the colon, esophagus, and colon, and high-speed cellular-resolution optical coherence microscopy. These applications are discussed below in sections 3 and 4.

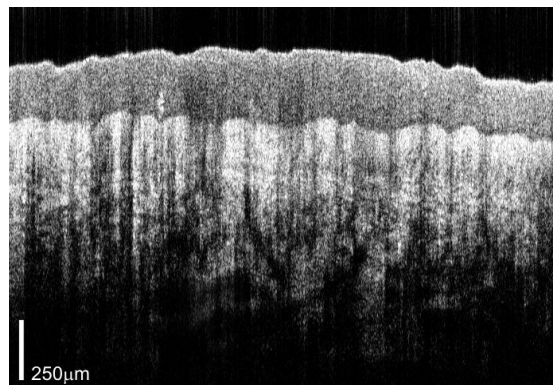


**Figure 1.6.** Swept source / Fourier domain OCT image of *in vivo* human skin, acquired at 42,000 axial lines / sec and 10 frames / sec.

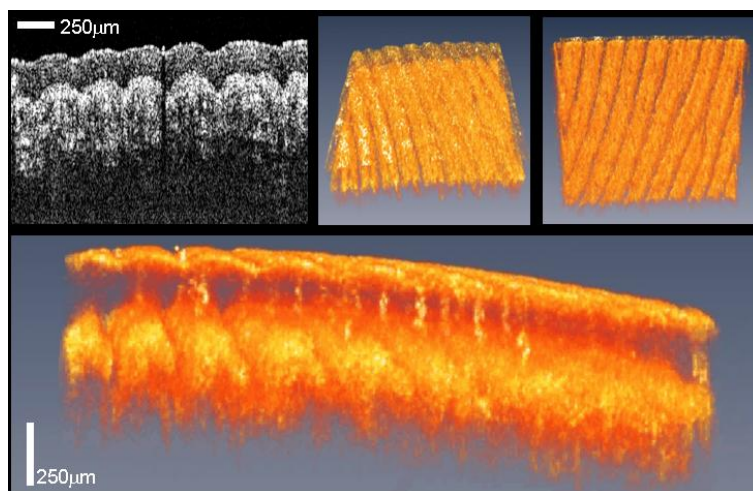


**Figure 1.7.** 3D Swept source / Fourier domain OCT image of *in vivo* human skin, acquired at 370,000 axial lines / sec and 2 volumes / sec.

## References

- [1] S. H. Yun, G. J. Tearney, J. F. de Boer, N. Iftimia, and B. E. Bouma, "High-speed optical frequency-domain imaging," *Optics Express*, vol. 11, pp. 2953-2963, Nov 3 2003.
- [2] M. A. Choma, M. V. Sarunic, C. Yang, and J. Izatt, "Sensitivity advantage of swept source and Fourier domain optical coherence tomography," *Optics Express*, vol. 11, pp. 2183-2189, 2003.
- [3] S. H. Yun, C. Boudoux, G. J. Tearney, and B. E. Bouma, "High-speed wavelength-swept semiconductor laser with a polygon-scanner-based wavelength filter," *Optics Letters*, vol. 28, pp. 1981-1983, Oct 15 2003.
- [4] M. A. Choma, K. Hsu, and J. Izatt, "Swept source optical coherence tomography using an all-fiber 1300-nm ring laser source," *Journal of Biomedical Optics*, vol. 10, p. #044009, 2005.

- [5] R. Huber, M. Wojtkowski, K. Taira, J. G. Fujimoto, and K. Hsu, "Amplified, frequency swept lasers for frequency domain reflectometry and OCT imaging: design and scaling principles," *Optics Express*, vol. 13, pp. 3513-3528, May 2 2005.
- [6] J. Zhang and Z. P. Chen, "In vivo blood flow imaging by a swept laser source based Fourier domain optical Doppler tomography," *Optics Express*, vol. 13, pp. 7449-7457, Sep 19 2005.
- [7] R. Huber, K. Taira, M. Wojtkowski, and J. G. Fujimoto, "Fourier domain mode-locked lasers for swept source OCT imaging at up to 290 kHz scan rates," in *Coherence Domain Optical Methods and Optical Coherence Tomography in Biomedicine IX*, San Jose, California, USA, 2005, pp. 96-99.
- [8] Y. Yasuno, V. Madjarova, S. Makita, M. Akiba, A. Morosawa, C. Chong, T. Sakai, K. Chan, M. Itoh, and T. Yatagai, "Three-dimensional and high-speed swept-source optical coherence tomography for in vivo investigation of human anterior eye segments," *Optics Express*, vol. 13, pp. 10652-10664, 2005.
- [9] W. Y. Oh, S. H. Yun, B. J. Vakoc, G. J. Tearney, and B. E. Bouma, "Ultrahigh-speed optical frequency domain imaging and application to laser ablation monitoring," *Applied Physics Letters*, vol. 88, Mar 6 2006.
- [10] D. Huang, E. A. Swanson, C. P. Lin, J. S. Schuman, W. G. Stinson, W. Chang, M. R. Hee, T. Flotte, K. Gregory, C. A. Puliafito, and J. G. Fujimoto, "Optical Coherence Tomography," *Science*, vol. 254, pp. 1178-1181, Nov 22 1991.
- [11] J. Zhang and Z. Chen, "Complex Fourier domain optical coherence tomography using the heterodyne technique," *Optics & Photonics News*, vol. 15, p. 17, Dec 2004.
- [12] S. R. Chinn, E. A. Swanson, and J. G. Fujimoto, "Optical coherence tomography using a frequency-tunable optical source," *Optics Letters*, vol. 22, pp. 340-342, Mar 1 1997.
- [13] B. Golubovic, B. E. Bouma, G. J. Tearney, and J. G. Fujimoto, "Optical frequency-domain reflectometry using rapid wavelength tuning of a Cr<sup>4+</sup>:forsterite laser," *Optics Letters*, vol. 22, pp. 1704-1706, Nov 15 1997.
- [14] M. A. Choma, M. V. Sarunic, C. H. Yang, and J. A. Izatt, "Sensitivity advantage of swept source and Fourier domain optical coherence tomography," *Optics Express*, vol. 11, pp. 2183-2189, Sep 8 2003.
- [15] R. Huber, K. Taira, M. Wojtkowski, and J. G. Fujimoto, "Fourier Domain Mode Locked Lasers for OCT imaging at up to 290kHz sweep rates," in *Optical Coherence Tomography and Coherence Techniques II*, Munich, 2005, pp. 245-250.
- [16] R. Huber, M. Wojtkowski, and J. G. Fujimoto, "Fourier Domain Mode Locking (FDML): A new laser operating regime and applications for optical coherence tomography," *Optics Express*, vol. 14, pp. 3225-3237, Apr 17 2006.
- [17] D. C. Adler, R. Huber, and J. G. Fujimoto, "Phase-sensitive optical coherence tomography at up to 370,000 lines per second using buffered Fourier domain mode locked lasers," *Opt Lett*, vol. 32, pp. 626-628, 2007.
- [18] R. Huber, D. C. Adler, V. J. Srinivasan, and J. G. Fujimoto, "Fourier domain mode locking at 1050 nm for ultrahigh-speed optical coherence tomography of the human retina at 236,000 axial scans per second," *Optics Letters*, vol. 32, p. In Press, 2007.
- [19] R. Huber, D. C. Adler, and J. G. Fujimoto, "Buffered Fourier Domain Mode Locking (FDML): Unidirectional swept laser sources for OCT imaging at 370,000 lines per second," *Optics Letters*, vol. 31, pp. 2975-2977, October 15, 2006 2006.

## 2. Ophthalmic OCT

### Sponsors

National Institutes of Health RO1-EY11289-20, RO1- EY013178-06, P30-EY008098

National Science Foundation BES-0522845, BES-0119494

Air Force Office of Scientific Research FA9550-040-1-0011, FA9550-050-1-0046

### Project Staff

Dr. Iwona Gorczynska, Jonathan J. Liu, Vivek J. Srinivasan, Professor James G. Fujimoto (MIT)

Royce Chen, Bryan Monson, Dr. Jay S. Duker (New England Eye Center)

Dr. Joel Schuman (University of Pittsburgh Medical Center)

Dr. Sven Bursell, Dr. Alan Clermont, Dr. Edward Feener (Joslin Diabetes Center)

Since its development in 1991, OCT has become a standard diagnostic technique in ophthalmology. Our group was responsible for the invention of OCT and initial development of OCT for ophthalmology. The first report of OCT was published in *Science* in 1991 and demonstrated *in vitro* imaging of the human retina and atherosclerotic plaque [1]. With improved technology and the availability of extensive clinical data, OCT is rapidly becoming a standard of care in ophthalmology.

The current commercial OCT device (StratusOCT) has an axial resolution of 10  $\mu\text{m}$  and can acquire an image in  $\sim 1.3$  seconds. Recent research advances have enabled high-speed ultrahigh resolution (UHR) OCT, achieving axial resolutions as fine as 2  $\mu\text{m}$  and acquiring retinal images in  $\sim 0.02$  seconds [2-5]. Our current research focuses on developing high-speed, ultrahigh resolution OCT for clinical and fundamental research applications.

In retinal pathologies, prognosis is significantly improved by detecting disease during its early stages. Early-stage retinal disease is often characterized by small changes in architectural morphology or physiology. There is a need to screen the retina for such changes comprehensively; quantitatively, objective markers for disease progression and response to treatment are required. Our high-speed UHR-OCT prototype enables three-dimensional imaging of the retina, acquiring comprehensive micron-scale structural information necessary for early detection of retinal disease. This instrument has been used in the ophthalmology clinic for imaging a range of retinal pathologies. In addition to performing qualitative cross-sectional studies of retinal diseases, our group is developing segmentation algorithms and visualization methods for quantitative analysis of OCT images. Another area of our research is structural and functional OCT imaging in the murine (rat and mouse) eye model.[6, 7] The murine eye is important due to its structural similarity to the human eye and relative ease of genetic manipulation, making it an important surrogate model for a number of retinal diseases.

Recent advances by our group in the area of OCT technology have enabled further dramatic improvements in performance. Recently, retinal imaging speeds as high as 250,000 axial scans per second were demonstrated using swept source / Fourier domain OCT. This represents an order of magnitude improvement in imaging speed compared to previous technologies. These advances may improve the performance of OCT in conventional imaging applications, and possibly enable novel applications such as functional imaging of the retina.

## 2.1 Technology for Clinical Ophthalmic OCT

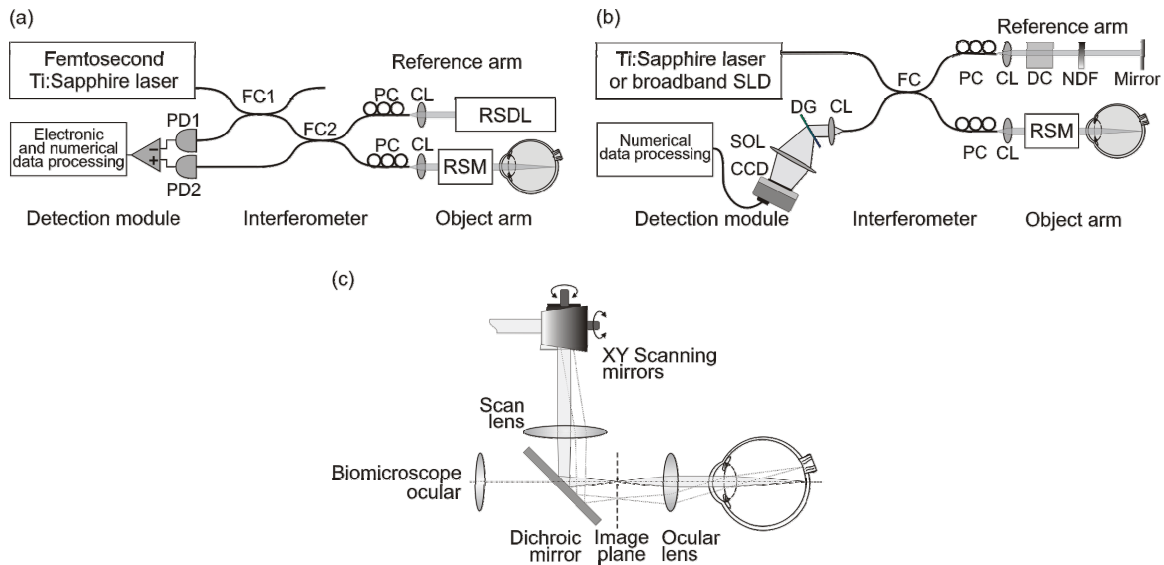


**Figure 2.1.** Schematic of the OCT technologies used for ophthalmic imaging: (a) Time-domain OCT system, (b) spectral/Fourier domain OCT system. (c) Retinal scanning module (RSM). FC – fiber coupler, PC – polarization controller, CL – collimating lens, RSDL – rapid scanning delay line, RSM – retinal scanning module, PD – photodiode, DC – dispersion compensation, NDF – neutral density filter, DG – diffraction grating, SOL – spectrometer objective lens, CCD – line scan CCD camera.

The OCT instruments that we used for clinical ophthalmic imaging are based on either time domain detection [1] (Figure 2.1 a) or spectral/Fourier domain detection [8, 9] (Figure 2.1 b). Ultrahigh resolution imaging ( $\sim 2 - 3.5 \mu\text{m}$ ) was achieved with a femtosecond titanium: sapphire laser [10, 11] (central wavelength of 820nm and bandwidth of 150 nm) or broadband superluminescent diode light source (bandwidth of  $\sim 100$  nm centered at 840 nm). High-speed data acquisition rates (up to 25,000 axial scans per second) were attained using spectral/Fourier domain detection.

To provide the visualization of retinal pathologies we developed several different scan protocols. Scan patterns initially proposed by our group for time domain systems have been implemented in commercially available devices [12, 13]. However, to take advantage of the enhanced performance of high-speed spectral/Fourier domain OCT novel imaging protocols are required. We developed several new protocols. The first one acquires a small number of 6 mm high-definition images (8192 A-scans  $\times$  3 B-scans). It is especially useful for patients with opaque media or other conditions that result in a low OCT signal, as transverse pixel averaging can be used to increase the signal-to-noise ratio. The second protocol (Figure 2.2 a) acquires a series of high transverse pixel density images in a 6 mm  $\times$  6 mm raster pattern (2048 A-scans  $\times$  21 B-scans). The third protocol (Figure 2.2 b) acquires three-dimensional OCT (3D-OCT) data. It achieves comprehensive retinal coverage, taking measurements on a 6 mm  $\times$  6 mm area with a spacing of  $12 \mu\text{m} \times 33 \mu\text{m}$  between axial scans. The large set of cross-sectional images can be useful for tracking pathologies in three dimensions, or detecting small focal pathologies. The fourth scanning pattern (Figure 2.2 c) consists of 24 radial scans with 1500 lines, centered at the fovea. This protocol samples most densely in the fovea, the region of the retina most important in determining visual acuity. This protocol can be used to map intraretinal layers.

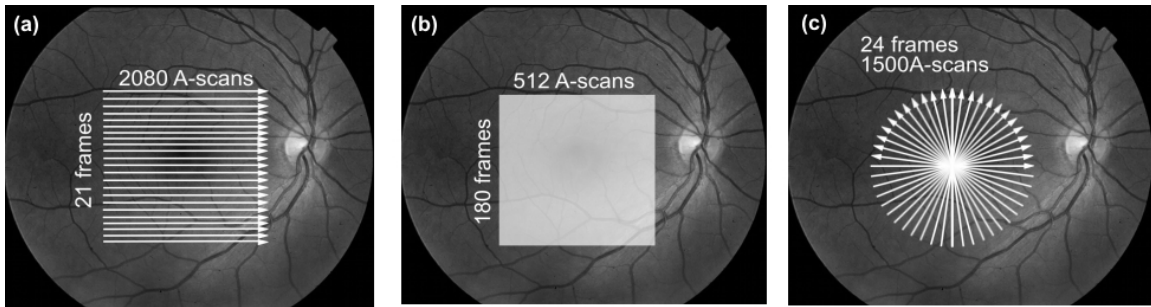


**Figure 2.2.** Selected scanning protocols for high-speed UHR-OCT instrument: (a) series of high transverse pixel density images in a 6 mm x 6 mm raster pattern (acquisition time: 1.8s), (b) three-dimensional OCT data (acquisition time: 3.7s), (c) radial scans (acquisition time: 1.4s).

## 2.2 Ultrahigh resolution OCT study of retinal pathologies

High-speed UHR-OCT has a number of advantages over commercially available OCT instruments including improved image quality, preservation of retinal topography, improved retinal coverage.[14] Images obtained using this technique show new features (reflective bands) at the level of the photoreceptors and retinal pigment epithelium (RPE) which were not previously visible on slower, lower resolution systems (Figure 2.3). Three-dimensional (3D) OCT imaging enables the creation of an OCT fundus image (Figure 2.4 a) which shows features such as blood vessels. Individual cross-sectional OCT images (Figure 2.4 b-c) are automatically registered to the OCT fundus image. This enables correlation of 3D OCT findings with standard ophthalmic examination.

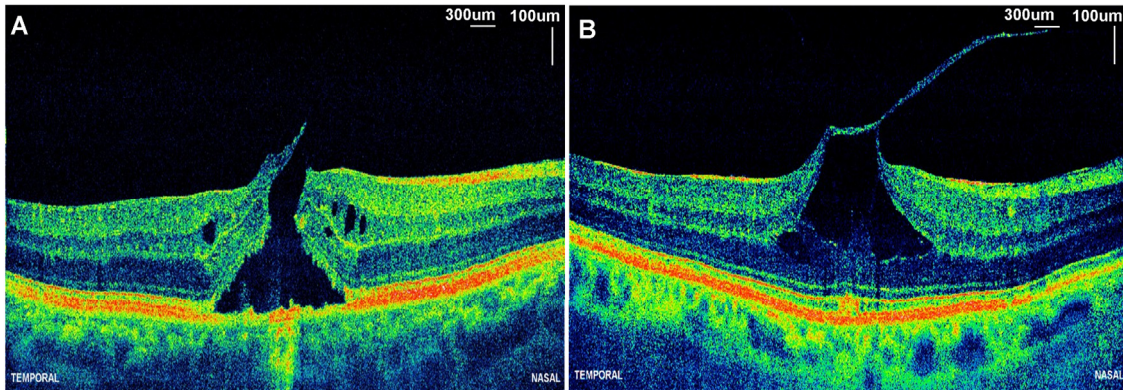


**Figure 2.3.** High transverse pixel density images of full thickness macular hole (A) and vitreomacular traction syndrome (B). The rapid acquisition time of high-speed ultrahigh resolution OCT eliminates the need for axial motion correction.

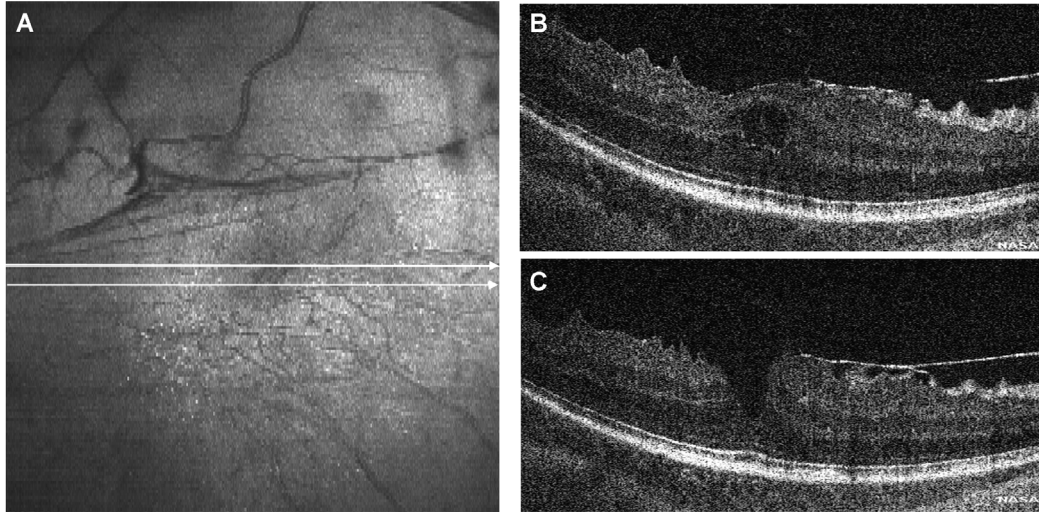


**Figure 2.4.** Three-dimensional imaging using high-speed ultrahigh resolution OCT. A raster scan set of 180 OCT images (512 axial scans each) is acquired in <4 seconds covering the entire volume of a macular pseudohole in the eye with epiretinal membrane and vitreomacular traction present. The OCT fundus image (A) is generated from the 3D OCT dataset. The location of each OCT image (B, C) can be precisely registered relative to the OCT fundus image (A).

High-speed UHR OCT provides new information about retinal structure that complements standard diagnostic techniques like fluorescein angiography (FA), indocyanine green angiography (ICG) or fundus photography by providing images of micron-scale pathological changes. Cross-sectional as well as longitudinal studies of pathologies are necessary in order to validate the technology. Cross-sectional studies[14, 15] illustrate features characteristic of retinal pathologies and aid in the correct interpretation of OCT images. They can also serve as motivation for future, more involved longitudinal investigations. Detailed qualitative and quantitative analysis of UHR OCT images allows for characterization of early markers of pathologies and improved understanding of pathogenesis. Our group is conducting clinical investigation of different eye pathologies in collaboration with New England Eye Center (N.E.E.C.) of Tufts-New England Medical Center (NEMC) and University of Pittsburgh Medical Center (UPMC). These studies were approved by the IRB committees of MIT, NEMC, and UPMC and are compliant with the Health Insurance Portability and Accountability Act of 1996.

Clinical studies using several generations of prototype instruments have been performed at the New England Eye Center and collaborating institutions over the past 15 years. Retinal diseases including macular holes,[16-19] glaucoma[20-25], and age-related macular degeneration[14, 15, 26, 27] have been studied. Numerous clinical studies involving a range of pathologies and other clinical findings have been performed as well.[19, 28-38]

### 2.3 Three-dimensional visualization methods for ophthalmic imaging

Ultrahigh resolution OCT data should be visualized in a way that reveals all information relevant to diagnosis of retinal pathologies. In the simplest visualization method single B-scans (or OCT frames) showing the most representative cross-sections of investigated pathology are presented using an appropriate color scale (commonly gray or false color scales representing different levels of light scattering in eye structures). Such a solution is usually utilized in standard resolution StratusOCT or ultrahigh resolution time domain OCT, where image acquisition speeds are relatively slow. However, with the advent of high-speed imaging, where as many as ~200

images are acquired at once more advanced methods of visualization and data display are required.

Improvements in imaging speed enabled by spectral/Fourier domain OCT allow raster scan protocols (Figure 2.2 b) to obtain densely sampled three-dimensional OCT data. This data can be visualized using a range of novel visualization methods [11, 35]. For example it can be used to create three dimensional (3D) OCT data rendering. Before visualization, individual frames from the three-dimensional data set were correlated to remove axial motion artifacts. Correlation between consecutive axial scans is unnecessary due to the fast acquisition rate. Virtual cross-sectional images, segmented, virtual perspective, and cut-away rendered views of the intraretinal layers were in this case generated using volumetric rendering software similar to that for magnetic resonance image processing.

Three dimensional data likewise sets of radial scans densely covering the retina (Figure 2.2 c) may be used for quantitative analysis of OCT tomograms [11, 39-41]. Segmentation of different eye structures allows for calculation of volume of selected retinal features (Figure 2.5) as well as mapping intraretinal layer thicknesses. The later is especially important in quantifying macular edema which is a consequence of many pathological retinal conditions such as diabetic retinopathy, epiretinal membrane formation, ocular inflammation, retinal vascular occlusion, and cataract extraction. Macular thickness analysis is particularly helpful in guiding and assessing treatments for macular edema such as photodynamic therapy, intravitreal corticosteroids, and vitrectomy. It is also important for the detection and monitoring of glaucoma [22].

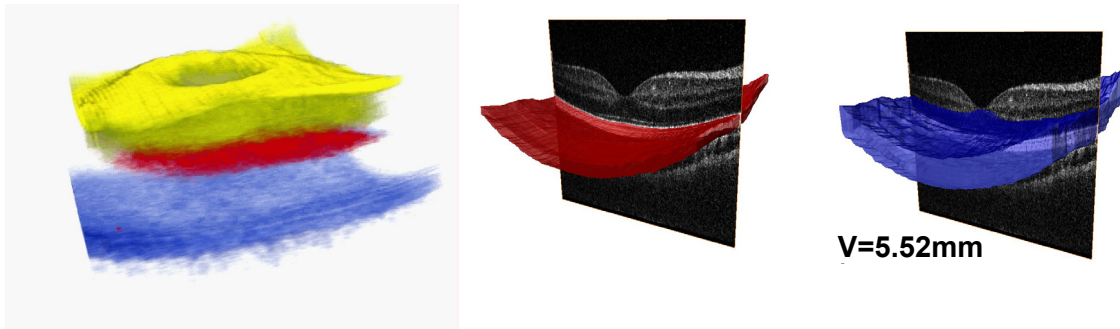


**Figure 2.5.** 3D-OCT data can be rendered and displayed using techniques similar to MR imaging.

Another visualization method is shown in Figure 2.6.(d) OCT fundus images are created by summing the three-dimensional data set along the axial direction at each transverse (*en face*) position on the retina. This corresponds to detecting all of the light backscattered or backreflected from each fundus position, and therefore is analogous to fundus photography or scanning laser ophthalmoscopy. Since the OCT fundus image is generated directly from the 3-D OCT data, OCT images are precisely and reproducibly registered with the fundus. The result is then displayed as a grey scale image that enables direct comparison of OCT findings with those from clinical examination, such as fundus photographs or fluorescein angiography. It is also possible to generate OCT fundus images selectively displaying specific retinal layers or specific retinal features.

En face OCT fundus images, sectioned at different levels of the retina are created using a segmentation algorithm based on the Laplacian edge detection method [42]. Correction for retinal curvature was performed to enable reliable en face sectioning. En face images are generated either by summation of signals from selected retinal layers or weighted axial summation of the entire 3D-OCT data. The method preserves information about all retinal layers, while enhancing the information from chosen sections of the retina. Sectioning was applied to different retinal layers to improve visualization of pathologies.

OCT fundus images provide maps showing changes in the light scattering properties of the retina related to different pathological conditions. For example: pigmentary changes in the RPE, different types of deposits, photoreceptor and/or RPE atrophy. They reveal tissue microstructure and give insight into topography of lesions. An example set of *en face* OCT fundus images are shown in Figure 2.6. (b)-(d) (f)-(h). The patient had retinopathy caused by sun-gazing. The patient was imaged with high-speed UHR OCT using the raster scan imaging protocol consisting of 180 frames (Figure 2.2. b). The disrupted areas in the *en face* images were similar in shape in both eyes. From the *en face* OCT fundus images of the right eye, chronic damage from sun-gazing is observed primarily confined to the outer retina.

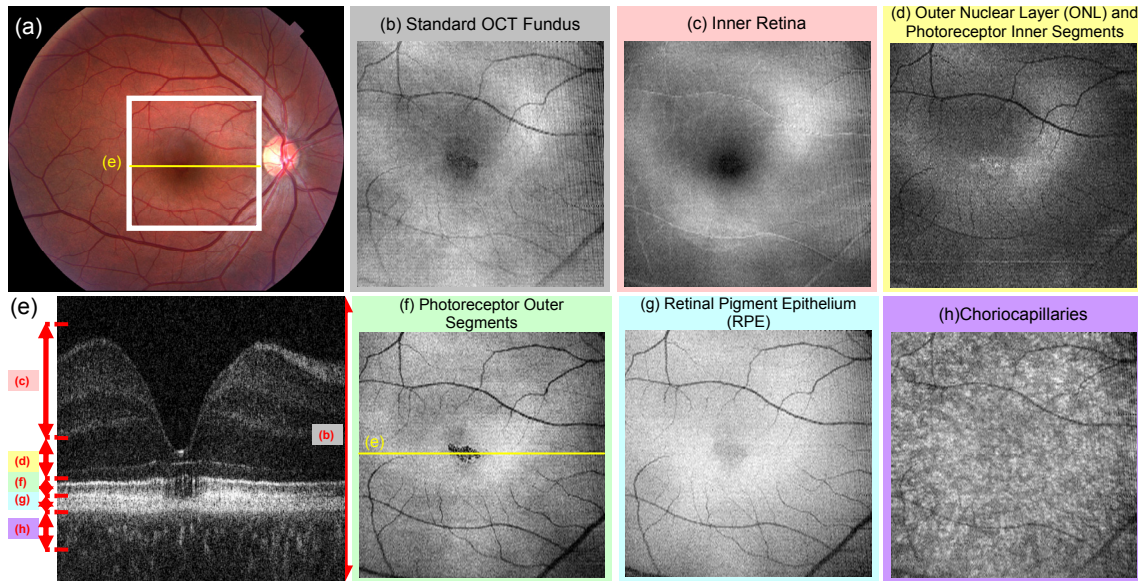


**Figure 2.6.** Solar Retinopathy. Damage from sun-gazing is primarily confined to the outer retina. Hyporeflective areas indicate photoreceptor disruption, clearly visible in the sectioned photoreceptor outer segments *en face* image (f). The photoreceptor outer segments in the foveal region are almost entirely absent. Vertical bands of hyporeflectivity through the photoreceptor IS/OS junction and outer segments demonstrate focal areas of photoreceptor cell death, as seen in figure (e).

Sectioning and segmentation methods may be optimized for specific diseases affecting localized regions or layers of the retina. Displaying these findings relative to retinal features such as vasculature, enables quick and intuitive assessment of the positions and areas of lesions. These attributes may help improve diagnostic efficiency.

## 2.4 Small animal retinal imaging

Research on ocular diseases is limited by the restrictions on studying pathophysiologic processes in the human eye. Likewise, many human ocular diseases are genetic in origin, but appropriate subjects often are not available for genetic studies. Murine (rat and mouse) models of ocular disease therefore provide powerful tools for characterization of disease pathogenesis and response to treatment. While enucleation and histology are the gold standard for characterization of microstructural changes in animals, non-invasive structural imaging has the potential to reduce the need for sacrifice and histology in many studies. Novel “spectral/Fourier domain” OCT detection methods enable high-speed imaging as well as numerical dispersion compensation and spectral shaping, which are crucial for visualizing the fine structures in the retina.

A high-speed, ultrahigh resolution Optical Coherence Tomography (UHR-OCT) system using “spectral/Fourier domain” detection was developed for small animal retinal imaging.[6] This system achieves imaging speeds of 24,000 axial scans per second, an improvement of ~100x over previous UHR-OCT systems. Using a broadband superluminescent diode light source, an axial image resolution of 2.8  $\mu\text{m}$  is achieved. A 10  $\mu\text{m}$  transverse resolution in air is obtained using a post-objective scanning microscope. High-speed, UHR-OCT enables high quality imaging of the murine retina and the visualization of all major intraretinal layers.

One limitation in the development of treatments for macular edema is the lack of appropriate animal models. In evaluating anti-permeability agents for treatment of diabetic macular edema in humans, an animal model that exhibits quantifiable edema is desired. Optical coherence tomography (OCT) has become the clinical standard for quantifying diabetic macular edema in humans,[13] and is therefore also the preferred method for characterization of retinal edema in animal models. Animal studies may also help to determine surrogate markers for early disease progression. The availability of clinical surrogate markers would help in the design of clinical trials with shorter time frames. These markers would also help to elucidate mechanisms by which hyperglycemia and diabetes cause changes in retinal hemodynamics and metabolism. By identifying appropriate animal models of diabetic retinopathy and imaging tools for characterization, the proposed studies will aid in identification of surrogate markers for early progression of diabetic retinopathy.

In collaboration with the Joslin Diabetes Center, a study investigating retinal thickness changes in a rat model of diabetic retinal edema was performed.[43] The eyes of STZ-induced diabetic rats were injected with either carbonic anhydrase-I (CA-I) or control saline solution (BSS). As focal areas of leakage were found using fluoresceindextran at 48 hours after intravitreal injection, we used this time point to investigate the effect of intravitreal injection of CA-I on retinal ultrastructure, using high-speed UHR OCT with 2.8  $\mu\text{m}$  axial image resolution. We observed that at 48 hours after intravitreal injection, the retinas of diabetic rats receiving CA-I were 12% thicker and the outer nuclear layer (ONL) 30% thicker than in contralateral eyes receiving an intravitreal saline vehicle injection (Figure 2.7). Indeed, in CA-I-treated eyes, the ONL accounted for 38% of the overall retinal thickness, an increase of 17% and 18%, respectively, compared to BSS-treated diabetic and nondiabetic rats. These data provide the first evidence, to our knowledge, of an endogenous molecule that induces clinically evident intraretinal edema in the diabetic rat model at physiologically relevant concentrations.

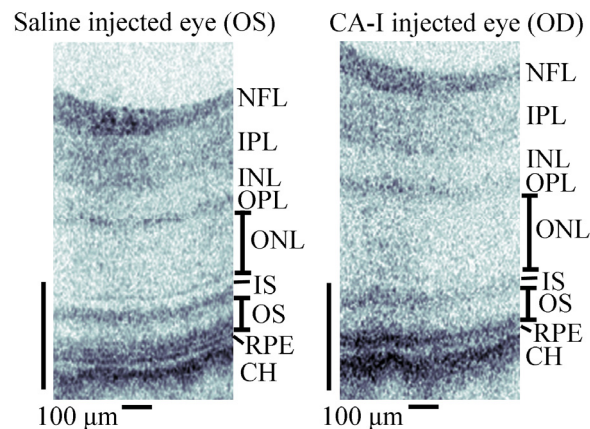


**Figure 2.7.** Eyes of diabetic rats injected with CA-1 showed an increase in retinal thickness after 48 hours, as compared to control contralateral eyes receiving saline vehicle injection.

## 2.5 Swept Source / Fourier domain OCT retinal imaging

Recent advances in optical coherence tomography (OCT) detection have enabled retinal imaging with speeds 50-100x faster than conventional OCT.[44, 45] These “spectral/Fourier domain” detection methods have an inherent speed/sensitivity advantage compared to conventional “time domain” detection methods.[46-48] Spectral/Fourier domain OCT, which uses a high-speed spectrometer in the detection arm to resolve the interference signal spectrally, typically operates at speeds of ~20-30,000 axial scans per second. Swept source OCT, which is performed using a tunable laser that sweeps in wavelength or frequency, has analogous theoretical speed/sensitivity advantages. Moreover, swept source OCT is possible with higher detection efficiency than spectral/Fourier domain OCT, which uses relatively inefficient CCD-based spectrometers in the detection arm and does not employ dual-balanced detection. Higher detection efficiency may enable swept source OCT imaging at higher speeds than current spectrometer-based OCT systems. In addition, the depth dependence of imaging sensitivity is a current limitation in spectral/Fourier domain OCT,[4, 45, 46] which may be overcome with swept source OCT using narrow line width tunable lasers. Swept source OCT was recently demonstrated in the retina at 1050 nm with ~10 micron axial resolution in tissue and 19,000 axial scans per second, showing improved visualization of choroidal structures.[49] In addition, swept source OCT at 850 nm and 43,500 axial scans per second with 10-micron axial resolution in tissue was demonstrated in microscopy and retinal imaging applications.

Our group demonstrated swept source OCT retinal imaging in two different wavelength ranges using two different semiconductor tunable laser designs. Firstly, swept source OCT retinal imaging at 16,000 axial scans per second was demonstrated at ~850 nm using a compact external cavity bulk laser.[50] This laser provides the highest axial resolution (<7 micron) swept source OCT retinal images achieved to date, and achieves a 6 dB drop in sensitivity over a ~2.5 mm imaging depth (~10-12 dB over 4 mm) in air. Secondly, ultrahigh-speed swept source OCT retinal imaging at 249,000 axial scans per second was demonstrated using a Fourier domain mode locked (FDML)[51] fiber laser operating at ~1070 nm. The axial resolution in tissue was ~12 micron and the imaging depth was ~1.4 mm for a 6 dB sensitivity drop. The 249,000 axial scan per second imaging speed, is to our knowledge, the highest speed retinal imaging demonstrated to date, and is an order of magnitude faster than typical spectral/Fourier domain OCT systems.

Using the external cavity bulk semiconductor laser, swept source OCT retinal imaging was performed. A high-definition 6 mm image (2048 axial scans, 0.125 seconds acquisition) of the normal human macula is shown in Figure 2.8 a, with a zoom of the foveal region (Figure 2.8 b). All major intraretinal layers are visible, including the external limiting membrane (ELM).[52] The improved sensitivity performance and imaging range of swept source OCT enables the visualization of deeper structures.

Figure 2.9 shows the schematic of the swept source OCT system used for ultrahigh-speed retinal imaging with an FDML laser. Only the backward sweep (long to short wavelength) was used, and an external unbalanced Mach-Zehnder interferometer doubled the effective sweep rate. A sweep rate of 249,000 axial scans per second was thus achieved. A booster amplifier was used to increase average sweep power. The full wavelength sweep range was 55 nm, and the full-width at half maximum (FWHM) was 44 nm, enabling an axial resolution of ~12 microns in tissue. A 3D OCT data (512 frames x 512 axial scans x 512 pixels) set could be acquired in ~1.1 seconds. Figure 2.10 shows images of the retina. Because of the rapid acquisition, median filtering could be used without correction for motion between frames. These initial results show that ultrahigh-speed OCT imaging with FDML lasers may improve performance in ophthalmic imaging applications.

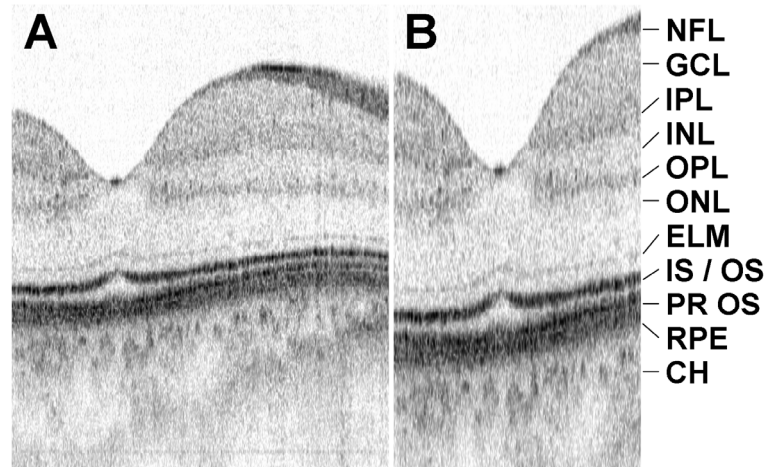


**Figure 2.8.** Retinal imaging results using swept source OCT at 850 nm. A) 2048 axial scan image through the fovea of a normal human retina. B) Zoom of foveal region. This image clearly shows the external limiting membrane (ELM), as well as the detailed structure of the photoreceptor outer segments. (NFL – nerve fiber layer, GCL – ganglion cell layer, IPL – inner plexiform layer, INL – inner nuclear layer, OPL – outer plexiform layer, ONL – outer nuclear layer, ELM – external limiting membrane, IS/OS – photoreceptor inner segment / outer segment junction, PR OS – photoreceptor outer segments, RPE – retinal pigment epithelium, CH – choroid)

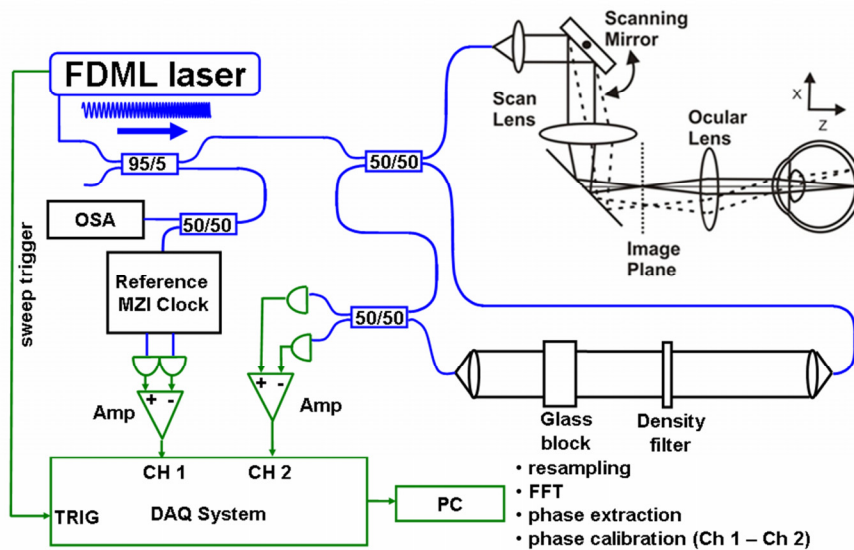


**Figure 2.9.** Schematic of ultrahigh speed OCT imaging system using an FDML laser. A reference Mach-Zehnder interferometer (MZI) is used to resample the acquired fringes. Dual-balanced detection is used to reduce excess intensity noise.

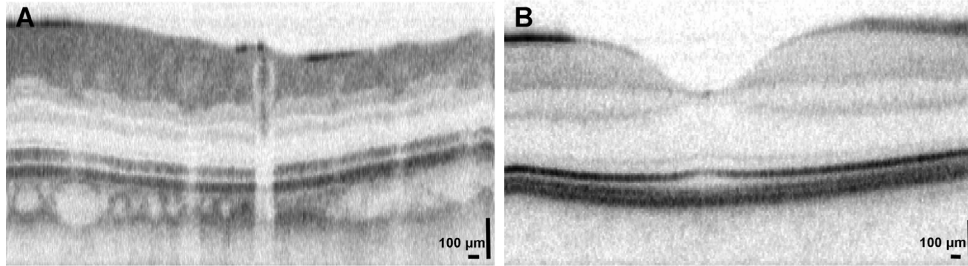


**Figure 2.10.** Ultrahigh-speed imaging enables speckle reduction for improved visualization of intraretinal layers (above right). Images from the 3D-OCT scan protocol median filtered along the slow (Y) axis are shown. Images were aligned in the axial direction prior to median filtering. A median filter with a length of 16 pixels was used to generate these preliminary results.

## References

- [1] D. Huang, E. A. Swanson, C. P. Lin, J. S. Schuman, W. G. Stinson, W. Chang, M. R. Hee, T. Flotte, K. Gregory, C. A. Puliafito, and J. G. Fujimoto, "Optical Coherence Tomography," *Science*, vol. 254, pp. 1178-1181, Nov 22 1991.
- [2] N. Nassif, B. Cense, B. H. Park, S. H. Yun, T. C. Chen, B. E. Bouma, G. J. Tearney, and J. F. de Boer, "In vivo human retinal imaging by ultrahigh-speed spectral domain optical coherence tomography," *Opt Lett*, vol. 29, pp. 480-2, Mar 1 2004.
- [3] R. A. Leitgeb, W. Drexler, A. Unterhuber, B. Hermann, T. Bajraszewski, T. Le, A. Stingl, and A. F. Fercher, "Ultrahigh resolution Fourier domain optical coherence tomography," *Optics Express*, vol. 12, pp. 2156-2165, May 17 2004.
- [4] M. Wojtkowski, V. J. Srinivasan, T. H. Ko, J. G. Fujimoto, A. Kowalewicz, and J. S. Duker, "Ultrahigh resolution, high speed, Fourier domain optical coherence tomography and methods for dispersion compensation," *Optics Express*, vol. 12, pp. 2404-2422, May 2004.
- [5] M. Wojtkowski, T. Bajraszewski, I. Gorczynska, P. Targowski, A. Kowalczyk, W. Wasilewski, and C. Radzewicz, "Ophthalmic imaging by spectral optical coherence tomography," *Am J Ophthalmol*, vol. 138, pp. 412-9, Sep 2004.
- [6] V. J. Srinivasan, T. H. Ko, M. Wojtkowski, M. Carvalho, A. Clermont, S. E. Bursell, Q. H. Song, J. Lem, J. S. Duker, J. S. Schuman, and J. G. Fujimoto, "Noninvasive volumetric imaging and morphometry of the rodent retina with high-speed, ultrahigh-resolution optical coherence tomography," *Invest Ophthalmol Vis Sci*, vol. 47, pp. 5522-8, Dec 2006.
- [7] V. J. Srinivasan, M. Wojtkowski, J. G. Fujimoto, and J. S. Duker, "In vivo measurement of retinal physiology with high-speed ultrahigh-resolution optical coherence tomography," *Opt Lett*, vol. 31, pp. 2308-10, Aug 1 2006.
- [8] A. F. Fercher, C. K. Hitzenberger, G. Kamp, and S. Y. Elzaiat, "Measurement of Intraocular Distances by Backscattering Spectral Interferometry," *Optics Communications*, vol. 117, pp. 43-48, May 15 1995.
- [9] G. Hausler and M. W. Lindner, "'Coherence radar" and "spectral radar"-new tools for dermatological diagnosis," *Journal of Biomedical Optics*, vol. 3, pp. 21-31, 1998/01/ 1998.
- [10] W. Drexler, U. Morgner, F. X. Kartner, C. Pitris, S. A. Boppart, X. D. Li, E. P. Ippen, and J. G. Fujimoto, "In vivo ultrahigh-resolution optical coherence tomography," *Optics Letters*, vol. 24, pp. 1221-1223, Sep 1 1999.
- [11] M. Wojtkowski, V. Srinivasan, J. G. Fujimoto, T. Ko, J. S. Schuman, A. Kowalczyk, and J. S. Duker, "Three-dimensional retinal imaging with high-speed ultrahigh-resolution optical coherence tomography," *Ophthalmology*, vol. 112, pp. 1734-46, Oct 2005.
- [12] M. R. Hee, C. A. Puliafito, C. Wong, J. S. Duker, E. Reichel, B. Rutledge, J. S. Schuman, E. A. Swanson, and J. G. Fujimoto, "Quantitative assessment of macular edema with optical coherence tomography," *Archives of Ophthalmology*, vol. 113, pp. 1019-1029, Aug 1995.

- [13] M. R. Hee, C. A. Puliafito, J. S. Duker, E. Reichel, J. G. Coker, J. R. Wilkins, J. S. Schuman, E. A. Swanson, and J. G. Fujimoto, "Topography of diabetic macular edema with optical coherence tomography," *Ophthalmology*, vol. 105, pp. 360-370, Feb 1998.
- [14] V. J. Srinivasan, M. Wojtkowski, A. J. Witkin, J. S. Duker, T. H. Ko, M. Carvalho, J. S. Schuman, A. Kowalczyk, and J. G. Fujimoto, "High-definition and 3-dimensional imaging of macular pathologies with high-speed ultrahigh-resolution optical coherence tomography," *Ophthalmology*, vol. 113, pp. 2054 e1-14, Nov 2006.
- [15] T. H. Ko, J. G. Fujimoto, J. S. Schuman, L. A. Paunescu, A. M. Kowalewicz, I. Hartl, W. Drexler, G. Wollstein, H. Ishikawa, and J. S. Duker, "Comparison of Ultrahigh- and Standard-Resolution Optical Coherence Tomography for Imaging Macular Pathology," *Ophthalmology*, Sep 22 2005.
- [16] M. R. Hee, C. A. Puliafito, C. Wong, J. S. Duker, E. Reichel, J. S. Schuman, E. A. Swanson, and J. G. Fujimoto, "Optical coherence tomography of macular holes," *Ophthalmology*, vol. 102, pp. 748-756, May 1995.
- [17] A. Chan, J. S. Duker, J. S. Schuman, and J. G. Fujimoto, "Stage 0 macular holes: observations by optical coherence tomography," *Ophthalmology*, vol. 111, pp. 2027-32, Nov 2004.
- [18] T. H. Ko, J. G. Fujimoto, J. S. Duker, L. A. Paunescu, W. Drexler, C. R. Baumal, C. A. Puliafito, E. Reichel, A. H. Rogers, and J. S. Schuman, "Comparison of ultrahigh- and standard-resolution optical coherence tomography for imaging macular hole pathology and repair," *Ophthalmology*, vol. 111, pp. 2033-43, Nov 2004.
- [19] T. H. Ko, A. J. Witkin, J. G. Fujimoto, A. Chan, A. H. Rogers, C. R. Baumal, J. S. Schuman, W. Drexler, E. Reichel, and J. S. Duker, "Ultrahigh-resolution optical coherence tomography of surgically closed macular holes," *Archives of Ophthalmology*, vol. 124, pp. 827-836, Jun 2006.
- [20] J. S. Schuman, M. R. Hee, C. A. Puliafito, C. Wong, T. Pedut-Kloizman, C. P. Lin, E. Hertzmark, J. A. Izatt, E. A. Swanson, and J. G. Fujimoto, "Quantification of nerve fiber layer thickness in normal and glaucomatous eyes using optical coherence tomography," *Archives of Ophthalmology*, vol. 113, pp. 586-596, May 1995.
- [21] J. S. Schuman, T. Pedut-Kloizman, E. Hertzmark, M. R. Hee, J. R. Wilkins, J. G. Coker, C. A. Puliafito, J. G. Fujimoto, and E. A. Swanson, "Reproducibility of nerve fiber layer thickness measurements using optical coherence tomography," *Ophthalmology*, vol. 103, pp. 1889-1898, Nov 1996.
- [22] H. Ishikawa, D. M. Stein, G. Wollstein, S. Beaton, J. G. Fujimoto, and J. S. Schuman, "Macular segmentation with optical coherence tomography," *Invest Ophthalmol Vis Sci*, vol. 46, pp. 2012-7, Jun 2005.
- [23] G. Wollstein, L. A. Paunescu, T. H. Ko, J. G. Fujimoto, A. Kowalewicz, I. Hartl, S. Beaton, H. Ishikawa, C. Mattox, O. Singh, J. Duker, W. Drexler, and J. S. Schuman, "Ultrahigh-resolution optical coherence tomography in glaucoma," *Ophthalmology*, vol. 112, pp. 229-37, Feb 2005.
- [24] G. Wollstein, J. S. Schuman, L. L. Price, A. Aydin, P. C. Stark, E. Hertzmark, E. Lai, H. Ishikawa, C. Mattox, J. G. Fujimoto, and L. A. Paunescu, "Optical coherence tomography longitudinal evaluation of retinal nerve fiber layer thickness in glaucoma," *Arch Ophthalmol*, vol. 123, pp. 464-70, Apr 2005.
- [25] M. Y. Kahook, R. J. Noecker, H. Ishikawa, G. Wollstein, L. Kagemann, M. Wojtkowski, J. S. Duker, V. J. Srinivasan, J. G. Fujimoto, and J. S. Schuman, "Peripapillary schisis in glaucoma patients with narrow angles and increased intraocular pressure," *Am J Ophthalmol*, vol. 143, pp. 697-9, Apr 2007.
- [26] M. R. Hee, C. R. Baumal, C. A. Puliafito, J. S. Duker, E. Reichel, J. R. Wilkins, J. G. Coker, J. S. Schuman, E. A. Swanson, and J. G. Fujimoto, "Optical coherence tomography of age-related macular degeneration and choroidal neovascularization," *Ophthalmology*, vol. 103, pp. 1260-1270, Aug 1996.
- [27] C. G. Pieroni, A. J. Witkin, T. H. Ko, J. G. Fujimoto, A. Chan, J. S. Schuman, H. Ishikawa, E. Reichel, and J. S. Duker, "Ultrahigh resolution optical coherence tomography in non-exudative age related macular degeneration," *British Journal of Ophthalmology*, vol. 90, pp. 191-197, Feb 2006.

- [28] T. A. Scheufele, A. J. Witkin, L. S. Schocket, A. H. Rogers, J. S. Schuman, T. H. Ko, J. G. Fujimoto, E. Reichel, and J. S. Duker, "Photoreceptor atrophy in acute posterior multifocal placoid pigment epitheliopathy demonstrated by optical coherence tomography," *Retina*, vol. 25, pp. 1109-1112, 2005.
- [29] L. S. Schocket, A. J. Witkin, J. G. Fujimoto, T. H. Ko, J. S. Schuman, A. H. Rogers, C. Bauman, E. Reichel, and J. S. Duker, "Ultrahigh-resolution optical coherence tomography in patients with decreased visual acuity after retinal detachment repair," *Ophthalmology*, vol. 113, pp. 666-672, Apr 2006.
- [30] A. J. Witkin, T. H. Ko, J. G. Fujimoto, A. Chan, W. Drexler, J. S. Schuman, E. Reichel, and J. S. Duker, "Ultra-high resolution optical coherence tomography assessment of photoreceptors in retinitis pigmentosa and related diseases," *Am J Ophthalmol*, vol. 142, pp. 945-52, Dec 2006.
- [31] A. J. Witkin, T. H. Ko, J. G. Fujimoto, J. S. Schuman, C. R. Bauman, A. H. Rogers, E. Reichel, and J. S. Duker, "Redefining lamellar holes and the vitreomacular interface: An ultrahigh-resolution optical coherence tomography study," *Ophthalmology*, vol. 113, pp. 388-397, Mar 2006.
- [32] A. J. Witkin, T. H. Ko, J. G. Fujimoto, J. S. Schuman, E. Reichel, and J. S. Duker, "Vitreofoveal attachment causing metamorphopsia: an ultrahigh-resolution optical coherence tomography finding," *Retina*, vol. 26, pp. 1085-7, Nov-Dec 2006.
- [33] A. J. Witkin, A. H. Rogers, T. H. Ko, J. G. Fujimoto, J. S. Schuman, and J. S. Duker, "Optical coherence tomography demonstration of macular infarction in sickle cell retinopathy," *Arch Ophthalmol*, vol. 124, pp. 746-7, May 2006.
- [34] M. H. Nguyen, A. J. Witkin, E. Reichel, T. H. Ko, J. G. Fujimoto, J. S. Schuman, and J. S. Duker, "Microstructural abnormalities in MEWDS demonstrated by ultrahigh resolution optical coherence tomography," *Retina*, vol. 27, pp. 414-8, Apr-May 2007.
- [35] A. J. Witkin, M. Wojtkowski, E. Reichel, V. J. Srinivasan, J. G. Fujimoto, J. S. Schuman, and J. S. Duker, "Photoreceptor disruption secondary to posterior vitreous detachment as visualized with optical coherence tomography," *Arch. Ophthalmol.*, submitted.
- [36] J. A. Rodriguez-Padilla, T. R. Hedges, 3rd, B. Monson, V. Srinivasan, M. Wojtkowski, E. Reichel, J. S. Duker, J. S. Schuman, and J. G. Fujimoto, "High-speed ultra-high-resolution optical coherence tomography findings in hydroxychloroquine retinopathy," *Arch Ophthalmol*, vol. 125, pp. 775-80, Jun 2007.
- [37] B. K. Monson, P. B. Greenberg, E. Greenberg, J. G. Fujimoto, V. J. Srinivasan, and J. S. Duker, "High-speed, ultra-high-resolution optical coherence tomography of acute macular neuroretinopathy," *Br J Ophthalmol*, vol. 91, pp. 119-20, Jan 2007.
- [38] L. Kagemann, G. Wollstein, H. Ishikawa, M. L. Gabriele, V. J. Srinivasan, M. Wojtkowski, J. S. Duker, J. G. Fujimoto, and J. S. Schuman, "Persistence of Cloquet's canal in normal healthy eyes," *Am J Ophthalmol*, vol. 142, pp. 862-4, Nov 2006.
- [39] K. Ishikawa, H. Terasaki, C. Kobayashi, Y. Niwa, C. H. Piao, Y. Ito, M. Kondo, and Y. Miyake, "Changes in foveal thickness and macular function after transpupillary thermotherapy for age-related macular degeneration," *Ophthalmic Res*, vol. 37, pp. 34-42, Jan-Feb 2005.
- [40] A. Chan, J. S. Duker, T. H. Ko, J. G. Fujimoto, and J. S. Schuman, "Normal macular thickness measurements in healthy eyes using stratus optical coherence tomography," *Archives of Ophthalmology*, vol. 124, pp. 193-198, Feb 2006.
- [41] H. Ishikawa, G. Wollstein, L. A. Paunescu, S. Beaton, J. G. Fujimoto, and J. S. Schuman, "Detailed retinal layer segmentation with optical coherence tomography: A pilot study," *Ophthalmology*, submitted.
- [42] D. Koozekanani, K. Boyer, and C. Roberts, "Retinal thickness measurements from optical coherence tomography using a Markov boundary model," *IEEE Transactions on Medical Imaging*, vol. 20, pp. 900-16, Sep 2001.
- [43] B. B. Gao, A. Clermont, S. Rook, S. J. Fonda, V. J. Srinivasan, M. Wojtkowski, J. G. Fujimoto, R. L. Avery, P. G. Arrigg, S. E. Bursell, L. P. Aiello, and E. P. Feener, "Extracellular carbonic anhydrase mediates hemorrhagic retinal and cerebral vascular permeability through prekallikrein activation," *Nat Med*, vol. 13, pp. 181-8, Feb 2007.

- [44] M. Wojtkowski, T. Bajraszewski, P. Targowski, and A. Kowalczyk, "Real-time in vivo imaging by high-speed spectral optical coherence tomography," *Optics Letters*, vol. 28, pp. 1745-1747, Oct 1 2003.
- [45] N. A. Nassif, B. Cense, B. H. Park, M. C. Pierce, S. H. Yun, B. E. Bouma, G. J. Tearney, T. C. Chen, and J. F. de Boer, "In vivo high-resolution video-rate spectral-domain optical coherence tomography of the human retina and optic nerve," *Optics Express*, vol. 12, Feb 9 2004.
- [46] R. Leitgeb, C. K. Hitzenberger, and A. F. Fercher, "Performance of Fourier domain vs. time domain optical coherence tomography," *Optics Express*, vol. 11, pp. 889-894, Apr 21 2003.
- [47] M. A. Choma, M. V. Sarunic, C. H. Yang, and J. A. Izatt, "Sensitivity advantage of swept source and Fourier domain optical coherence tomography," *Optics Express*, vol. 11, pp. 2183-2189, Sep 8 2003.
- [48] J. F. de Boer, B. Cense, B. H. Park, M. C. Pierce, G. J. Tearney, and B. E. Bouma, "Improved signal-to-noise ratio in spectral-domain compared with time-domain optical coherence tomography," *Optics Letters*, vol. 28, pp. 2067-2069, Nov 1 2003.
- [49] E. C. W. Lee, J. F. de Boer, M. Mujat, H. Lim, and S. H. Yun, "In vivo optical frequency domain imaging of human retina and choroid," *Optics Express*, vol. 14, pp. 4403-4411, May 15 2006.
- [50] V. J. Srinivasan, R. Huber, I. Gorczynska, J. G. Fujimoto, J. Y. Jiang, P. Reisen, and A. E. Cable, "High-speed, high-resolution optical coherence tomography retinal imaging with a frequency-swept laser at 850 nm," *Opt Lett*, vol. 32, pp. 361-3, Feb 15 2007.
- [51] R. Huber, M. Wojtkowski, and J. G. Fujimoto, "Fourier Domain Mode Locking (FDML): A new laser operating regime and applications for optical coherence tomography," *Optics Express*, vol. 14, pp. 3225-3237, Apr 17 2006.
- [52] W. Drexler, U. Morgner, R. K. Ghanta, F. X. Kärtner, J. S. Schuman, and J. G. Fujimoto, "Ultrahigh-resolution ophthalmic optical coherence tomography," *Nature Medicine*, vol. 7, pp. 502-507, Apr 2001.

### 3. Optical Biopsy using OCT

#### Sponsors

National Institutes of Health – RO1-EY011289-21, RO1-CA75289-08  
National Science Foundation – BES-0522845, ECS-0501478, BES-0119494, ECS-0119452  
Air Force Office of Scientific Research – FA9550-040-1-0011, FA9550-040-1-0046  
German Research Foundation (DFG) – HU 1006/1-1  
Natural Sciences and Engineering Research Council of Canada – CGS D2-331643-2006  
Cancer Research and Prevention Foundation  
The Whitaker Foundation

#### Project Staff

Prof. James G. Fujimoto, Dr. Peter M. Andrews (Georgetown University), Dr. Yu Chen, Dr. Hiroshi Mashimo (VA Medical Center), Dr. Robert Huber (Ludwig Maximilians University, Munich, Germany), Dr. Joseph Schmitt (LightLab Imaging), Desmond C. Adler, Aaron D. Aguirre, Shu-Wei Huang

Optical coherence tomography (OCT) is an emerging biomedical imaging technology that enables the visualization of tissue microstructures in situ and in real-time, with a resolution of 1-10  $\mu\text{m}$ , 10-100 times higher than standard ultrasound. OCT can provide cross-sectional images at the resolution approaching that of histopathology, which may allow differentiation of normal from diseased tissues. However, unlike conventional biopsy and histology process, OCT can be performed in real-time and without the need of tissue excision, thus increasing its possible application areas in where the excision biopsy is impossible or undesirable, and potentially allowing the use of OCT in guidance of biopsy or surgery. This potential has been demonstrated

in a wide range of applications such as ophthalmology [1, 2], cardiology [3, 4], gastroenterology [5-7], dermatology [8], dentistry [9], urology [10], and gynecology [11]. In our lab, we are developing the advanced technology for OCT and investigating the use of OCT in imaging a variety of clinically relevant tissue types and pathologies, for application in clinical diagnosis and treatment, and for basic biomedical research. Integration of high-speed, high-resolution OCT into portable systems with various delivering devices offers promise to enable new applications in clinics and pathology labs.

## References

- [1] M. R. Hee, J. A. Izatt, E. A. Swanson, D. Huang, J. S. Schuman, C. P. Lin, C. A. Puliafito, and J. G. Fujimoto, "Optical coherence tomography of the human retina," *Archives of Ophthalmology*, vol. 113, pp. 325-332, Mar 1995.
- [2] C. A. Puliafito, M. R. Hee, J. S. Schuman, and J. G. Fujimoto, *Optical coherence tomography of ocular diseases*. Thorofare, NJ: Slack Inc., 1996.
- [3] J. G. Fujimoto, S. A. Boppart, G. J. Tearney, B. E. Bouma, C. Pitris, and M. E. Brezinski, "High resolution in vivo intra-arterial imaging with optical coherence tomography," *Heart*, vol. 82, pp. 128-33, Aug 1999.
- [4] I. K. Jang, B. Bouma, B. MacNeill, M. Takano, M. Shishkov, N. Iftima, and G. J. Tearney, "In-vivo coronary plaque characteristics in patients with various clinical presentations using Optical Coherence Tomography," *Circulation*, vol. 108, pp. 373-373, OCT 28 2003.
- [5] B. E. Bouma, G. J. Tearney, C. C. Compton, and N. S. Nishioka, "High-resolution imaging of the human esophagus and stomach in vivo using optical coherence tomography," *Gastrointestinal endoscopy*, vol. 51(4) Pt 1, pp. 467-74, Apr 2000.
- [6] M. V. Sivak, Jr., K. Kobayashi, J. A. Izatt, A. M. Rollins, R. Ung-Runyawee, A. Chak, R. C. Wong, G. A. Isenberg, and J. Willis, "High-resolution endoscopic imaging of the GI tract using optical coherence tomography," *Gastrointestinal endoscopy*, vol. 51(4) Pt 1, pp. 474-9, Apr 2000.
- [7] X. D. Li, S. A. Boppart, J. Van Dam, H. Mashimo, M. Mutinga, W. Drexler, M. Klein, C. Pitris, M. L. Krinsky, M. E. Brezinski, and J. G. Fujimoto, "Optical coherence tomography: advanced technology for the endoscopic imaging of Barrett's esophagus," *Endoscopy*, vol. 32, pp. 921-30, Dec 2000.
- [8] J. Welzel, C. Reinhardt, E. Lankenau, C. Winter, and H. H. Wolff, "Changes in function and morphology of normal human skin: evaluation using optical coherence tomography," *Br J Dermatol*, vol. 150, pp. 220-5, Feb 2004.
- [9] L. L. Otis, M. J. Everett, U. S. Sathyam, and B. W. Colston, Jr., "Optical coherence tomography: a new imaging technology for dentistry," *The Journal of the American Dental Association*, vol. 131, pp. 511-4, Apr 2000.
- [10] A. V. D'Amico, M. Weinstein, X. Li, J. P. Richie, and J. Fujimoto, "Optical coherence tomography as a method for identifying benign and malignant microscopic structures in the prostate gland," *Urology*, vol. 55, pp. 783-7, May 2000.
- [11] C. Pitris, A. Goodman, S. A. Boppart, J. J. Libus, J. G. Fujimoto, and M. E. Brezinski, "High-resolution imaging of gynecologic neoplasms using optical coherence tomography," *Obstetrics and gynecology*, vol. 93, pp. 135-9, Jan 1999.

### 3.1 Ultrahigh-Speed 3D Endomicroscopy

Gastrointestinal (GI) cancers will be found in over 200,000 new people and will cause over 79,000 deaths in the United States in 2007[1]. When detected and treated early, the 5-year survival rate for colorectal cancer increases by a factor of 1.3[1]. For esophageal cancer, the rate increases by a factor of 2[1]. Unfortunately, many early-stage lesions are missed during standard endoscopic examination. Approximately 15 – 27% of small (< 5 mm) lesions in the colon go undetected, with miss rates of flat lesions being ~2x worse than polypoid lesions[2]. The situation is worse in the esophagus, where 30 – 40% of relatively large, invasive cancers are missed[3]. A

method for imaging the GI tract that can detect the earliest stages of cancer may reduce morbidity and mortality associated with the disease, allowing physicians to intervene earlier using minimally invasive therapies.

The majority of gastrointestinal (GI) cancers begin as small ( $< 100 \mu\text{m}$ ) lesions that are impossible to identify using conventional endoscopy. OCT is well-suited for detecting the changes in tissue microstructure associated with early GI cancers. Since the lesions are not visually apparent, however, it is necessary to survey a relatively large area of the GI tract with high-resolution OCT in order to avoid missing the lesions. As tissue motion and patient discomfort are problematic in the GI tract, imaging must be performed at extremely high speeds inside the living body. Recently, our group has developed an endoscopic imaging system using an FDML laser, state-of-the-art data acquisition system, and rapid spiral-scanning fiberoptic endoscope probe. This "3D endomicroscopy" system is capable of acquiring 3D-OCT data at unprecedented speeds and 3D resolutions, enabling the detection of small GI structures linked to colon cancer for the first time. 3D acquisition also enables a variety of powerful visualization techniques such as frame averaging for speckle reduction, *en face* image generation for comparison to microscopy or endoscopy, and arbitrary sectioning with quantitative measurement of tissue structures.

To perform *in vivo* 3D imaging of organs such as the colon and esophagus, several criteria must be met simultaneously. First, the optical resolution of the system must be sufficiently high to detect features that are of clinical interest. For detecting the earliest stages of cancer in the colon, for example, it is desirable to clearly resolve individual crypt structures that are  $40 - 80 \mu\text{m}$  in diameter[4]. Second, the spatial sampling density of the system must be sufficiently high to fully utilize the optical resolution. For an OCT system with an optical resolution of  $10 \times 10 \times 10 \mu\text{m}$  (XYZ), for example, the system should acquire data points every  $5 \mu\text{m}$  in all three dimensions according to the Nyquist sampling criteria. Third, the dataset should be acquired over a time frame shorter than or comparable to the time associated with tissue motion in the organ. In the colon, where tissue motility and whole-body movement are the dominant sources of motion artifacts, this time scale is  $10 - 20$  seconds. In the esophagus, where cardiac motion can displace the lumen, the time scale is  $0.5 - 2$  seconds. High speed imaging is also necessary to minimize procedure times and patient discomfort. Finally, it is beneficial to be able to perform a higher speed, lower resolution "survey scan" of a large segment of the colon or esophagus. A survey scan could allow suspicious areas of tissue to be identified, perhaps automatically[5], and subsequently imaged at higher resolution for a more detailed analysis.

With these requirements in mind, an ultrahigh-speed 3D endoscopic OCT system was developed for *in vivo* imaging of GI tract. Figure 3.1 shows a schematic of the complete imaging system. A dual-balanced Michelson interferometer constructed with a matched pair of circulators and a single 50/50 splitter is used to reduce amplitude noise while minimizing signal loss. The FDML laser produces a sweep trigger that is passed to the DAQ system in order to synchronize operation to the beginning of each wavelength sweep. The OCT signal must be evenly spaced in optical frequency prior to Fourier transformation to form the image, but the FDML laser produces sweeps where the frequency evolution is a sine function in time. To correct for this effect without storing and processing a second reference signal, an optical frequency clocking method is used. 5% of the laser output is routed to an asymmetric Mach-Zehnder interferometer (MZI) that produces interference fringes with zero crossings evenly spaced in optical frequency. These fringes are detected by a dual balanced photoreceiver and the zero crossings are identified by an analogue voltage comparator, generating a digital pulse train that functions as an optical frequency clock (OFC).

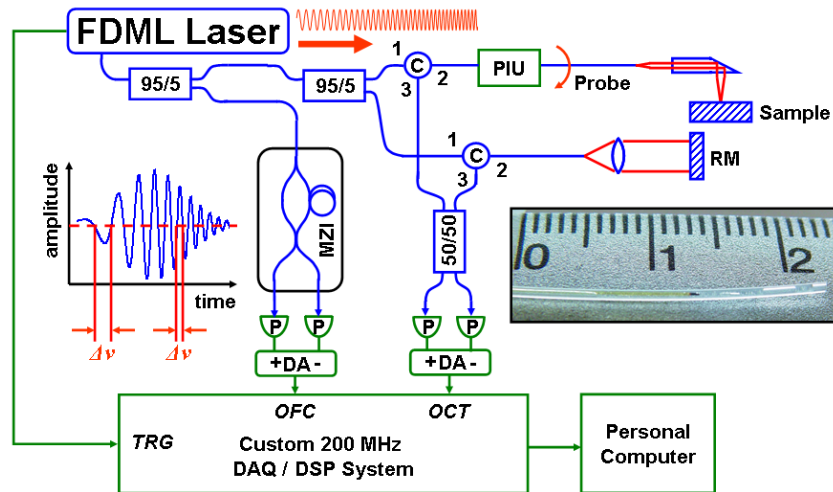


**Figure 3.1.** Schematic diagram of a high-speed 3D-OCT endomicroscopy system for use inside the body. C: circulator. PIU: patient interface unit. RM: reference mirror. MZI: Mach-Zehnder interferometer. P: photodiode. DA: differential amplifier. TRG: sweep trigger input. OFC: optical frequency clock input. OCT: OCT signal input. Left inset: concept of optical frequency clocking, where MZI fringes are evenly spaced in optical frequency  $\nu$ . Right inset: photograph of the fiberoptic imaging probe.

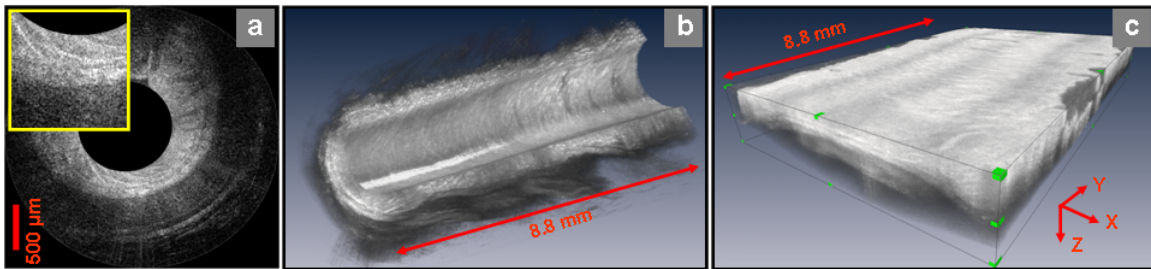
The OFC is used to trigger data acquisition of the OCT signal. Since the same frequency sweep from the laser generates both the MZI and OCT fringes, the spacing of the OFC pulses corresponds to evenly-spaced optical frequency intervals in the OCT signal. Therefore after digitization the OCT signal becomes evenly spaced in optical frequency as a function of sample index. The OCT signal is digitized by a 200 MS/sec analog-to-digital converter and continuously streamed to the RAM of a personal computer. The computer performs a fast Fourier transform to synthesize the image. Each frame is interpolated into polar coordinates and displayed as a radial image in real time at  $> 20$  frames per second on the monitor. During 3D acquisition, sustained frame rates of up to 60 Hz are achieved while maintaining the real-time display capabilities. The maximum imaging duration is limited only by available RAM on the computer.

The fiber optic probe pictured in Fig. 3.1 is a spiral-scanning device that combines rapid rotary motion (up to 50 Hz) with a linear pullback (0.5 – 5 mm/sec) to image 3D volumes. The optical fiber is placed inside a flexible polymer tube, which is necessary for mechanical stability. The tube can be water flushed using a syringe located outside the body to reduce specular reflection from the tissue surface and wash debris from the imaging site. The proximal end of the fiber is attached to a patient interface unit (PIU) containing the rotary and push/pull actuators. The distal end of the fiber is attached to an angle-polished microlens, providing a  $9 \mu\text{m}$  spot diameter. The total probe diameter is 0.83 mm, allowing it to pass down the working channel of a wide variety of commercial endoscopes.

A demonstration experiment was performed in the rabbit colon in order to validate the 3D-OCT endomicroscopy system. The imaging rate was 100,000 axial lines per second. The optical resolution in tissue was  $9 \times 9 \times 7 \mu\text{m}$  (XYZ). The spatial sampling density is  $3 \times 10 \times 3.5 \mu\text{m}$  (XYZ). The X and Z sampling densities were sufficiently high to fully utilize the optical resolution, while the transverse (Y) dimension was  $\sim 2\times$  undersampled. Transverse sampling was limited by the rotational speed of the fiber optic probe. Taking into account both the optical resolution and spatial sampling density of the system, the true resolvable 3D feature size is  $9 \times 20 \times 7 \mu\text{m}$ . This compares favorably to previously reported endoscopic OCT systems[6], where the true XY resolution and thus resolvable feature size is limited by spatial sampling to  $46 \times 64 \mu\text{m}$  in the GI tract. The maximum imaging depth was 1.5 mm in tissue. An 8.8 mm segment of colon was

imaged in 17.7 seconds. The fiber optic probe was rotated at 50 Hz and pulled back at 0.5 mm/sec. Commercially available rendering software was used to visualize the 3D data.

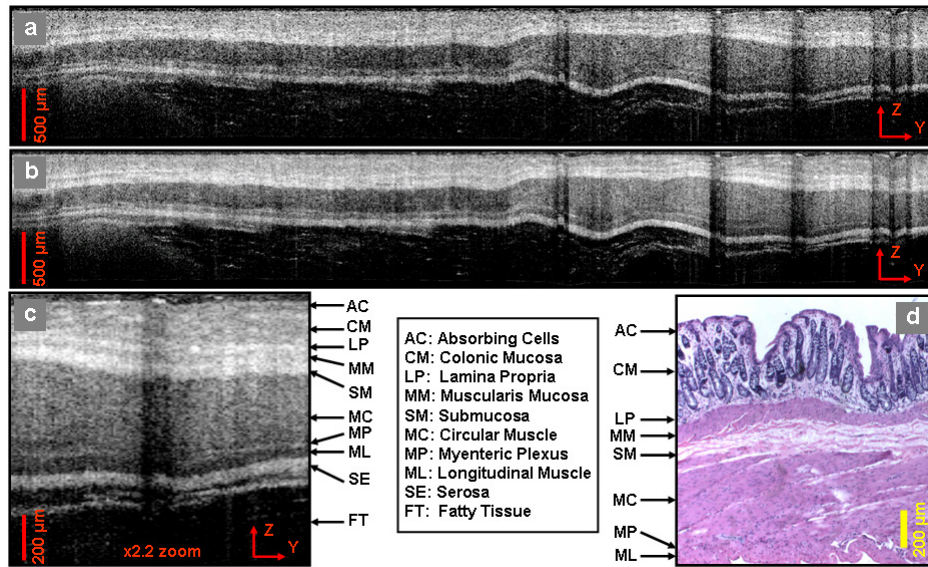
Figure 3.2 shows several visualizations of the dataset. Figure 3.2(A) shows a single radial frame from near the center of the colon segment. The inset shows an enlarged view of the epithelium. Colonic crypts are clearly distinguishable as dark regions surrounded by bright filament-like bands of lamina propria. The ability to detect and analyze crypt structures in 3D is important since abnormal crypts are signatures of early neoplastic change[4]. The complete volumetric dataset is composed of 885 radial frames, which can be processed and displayed in 3D. Figure 3.2(B) shows a cutaway view of the rendered dataset to allow visualization of the tissue morphology. Crypts are again visible on the luminal surface as well as in the epithelial wall. It is possible to perform a “virtual incision” by unfolding the tissue from cylindrical into rectangular form as shown in Fig. 3.2(C). The unfolded visualization enables clearer appreciation of tissue morphology and comparison to techniques such as endoscopy or biopsy-based histology. After unfolding, cross-sectional OCT images with arbitrary orientations can be generated that are precisely registered to the surface of the tissue.



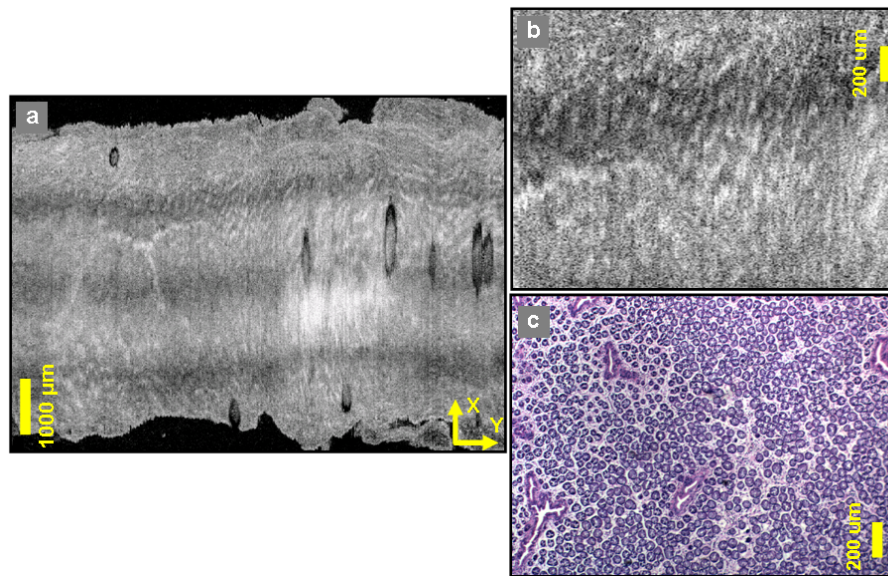
**Figure 3.2.** *In vivo* 3D-OCT data acquired in the rabbit colon at 100,000 axial lines / sec. A: single radial frame, with the epithelium shown as an enlarged inset. Colonic crypts are visible in the epithelium. B: Cutaway view of the cylindrical volume rendering of the entire dataset. C: Rectangular volume rendering of the tissue following a virtual incision and unfolding.

Figure 3.3(A) shows a single longitudinal (YZ) slice through the middle of the unfolded volume. Since the data set is sampled with a high spatial density, consecutive slices can be averaged to reduce speckle noise without significantly blurring image features. Figure 3.3(B) shows the mean of 7 consecutive slices, equivalent to averaging over a 21  $\mu\text{m}$  thick section. This dimension corresponds to less than two epithelial cells, so tissue structure is largely constant and minimal blurring is observed. Since the speckle size is approximately equal to the 9- $\mu\text{m}$  focal spot size, the speckle pattern is decorrelated over the section and image averaging enhances tissue contrast. Figure 3.3(B) shows an enlarged view of a region of Fig. 3.3(B). The OCT image correlates well with representative histology of colonic tissue from the same animal, shown in Fig. 3.3(D).

*En face* (XY) OCT images can also be generated, similar to those obtained with a magnifying endoscope or microscope, except the OCT images can be viewed at arbitrary tissue depths. Figure 3.4(A) shows an *en face* OCT image of the colon averaged over an 18  $\mu\text{m}$  section at a depth of 144  $\mu\text{m}$ , corresponding to the center of the colonic mucosa. Crypts are visible as dark regions between bright white bands of lamina propria. The three darker bands extending along the Y dimension are polarization artifacts caused by probe rotation. Figure 3.4(B) shows an enlarged view of a section of Fig. 3.4(A), while Fig. 3.4(C) shows an *en face* histological section from approximately the same depth. The size and distribution of crypts vary, with crypts often appearing larger in the OCT image. This is due to tissue shrinkage that occurs during histology processing, and differences in crypt orientation in the OCT image compared to the histological plane.



**Figure 3.3.** Longitudinal (YZ) OCT images taken from the center of the 3D dataset. A: single YZ frame. B: average of 7 frames over a width of 21  $\mu\text{m}$ , showing reduced speckle noise. C: enlarged view of a region of B, showing the layered structure of the colonic tissue. D: representative histology of colonic tissue showing good correlation to the OCT image.



**Figure 3.4.** *En face* (XY) OCT images taken at a depth of 144  $\mu\text{m}$  into the colonic tissue. A: average of 6 XY frames over a width of 18  $\mu\text{m}$ . B: enlarged view of a region of A, showing colonic crypts as dark bands between white strands of lamina propria. C: representative *en face* histology of colonic tissue showing good correlation to the OCT image.

Densely sampled volumetric 3D-OCT datasets enable quantitative 3D measurements of architectural morphology. Figure 3.5(A) shows an unfolded cross-sectional (XZ) image averaged over a 20  $\mu\text{m}$  width. Figure 3.5(B) shows an enlarged view of a segment of Fig. 3.5(A). The red arrows indicate two specific crypts and the dashed line defines a plane normal to the long axis of the crypts. Figure 3.5(C) shows this plane averaged along a 140  $\mu\text{m}$  section parallel to the long axis. The crypts are ovular in cross-section, likely due to slight compression of the tissue from the probe, with dimensions of  $\sim 120 \times 50 \mu\text{m}$ . The crypts extend  $\sim 300 \mu\text{m}$  in depth. The ability to quantitatively measure individual crypts could be important in recognizing clusters of aberrant crypt foci [4], which are markers of early colon cancer.

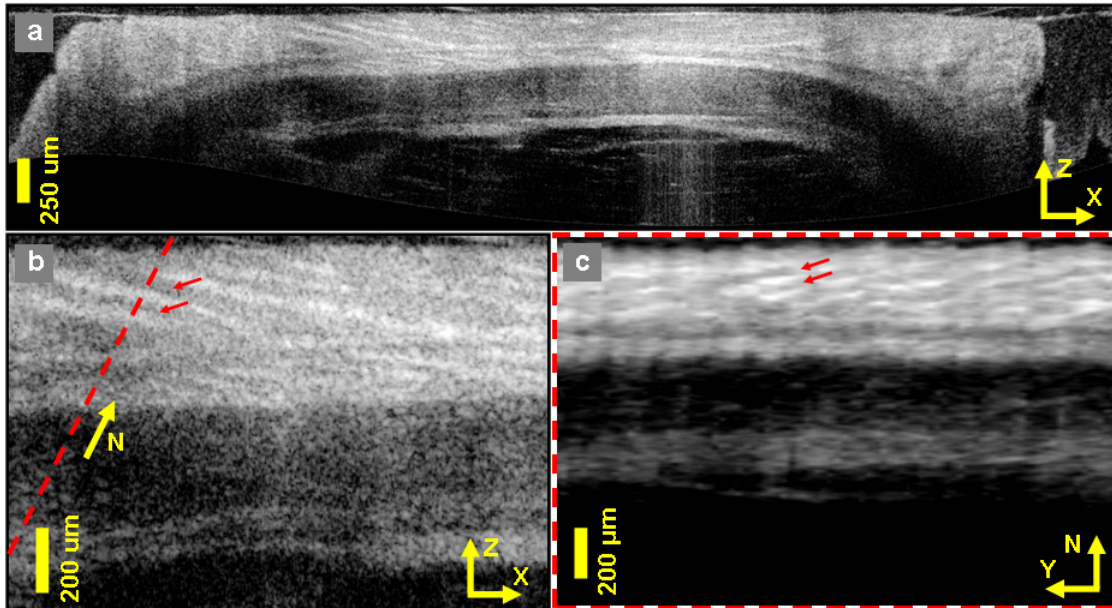


**Figure 3.5.** Cross-sectional (XZ) OCT images taken near the center of the 3D dataset. A: average of 2 XY frames over a width of 20  $\mu\text{m}$ . B: enlarged view of a region of A, showing colonic crypts as dark bands between white strands of lamina propria. Dashed red line defines a plane normal to the long axis of the crypts. C: Image formed by projecting the plane defined in B over a 140  $\mu\text{m}$  path parallel to the long axis of the crypts. Crypts can be quantitatively measured.

In the future, this system will be evaluated for its ability to detect early diseases in humans that are difficult to detect endoscopically. This may include early dysplastic changes in patients with chronic inflammation of the colon or esophagus. The system speed will also increase as more advanced data acquisition systems become available, since the FDML laser can support speeds several times higher than the current 100,000 axial lines per second.

## References

- [1] American Cancer Society, "Cancer Facts and Figures - 2007," Atlanta 2007.
- [2] D. K. Rex, "Maximizing detection of adenomas and cancers during colonoscopy," *American Journal of Gastroenterology*, vol. 101, pp. 2866-2877, Dec 2006.
- [3] S. J. Spechler, "Dysplasia in Barrett's esophagus: limitations of current management strategies," *American Journal of Gastroenterology*, vol. 100, pp. 927-935, Apr 2005.

- [4] T. Takayama, S. Katsuki, Y. Takahashi, M. Ohi, S. Nojiri, S. Sakamaki, J. Kato, K. Kogawa, H. Miyake, and Y. Niitsu, "Aberrant crypt foci of the colon as precursors of adenoma and cancer," *New England Journal of Medicine*, vol. 339, pp. 1277-1284, Oct 29 1998.
- [5] X. Qi, M. V. Sivak, G. Isenberg, J. E. Willis, and A. M. Rollins, "Computer-aided diagnosis of dysplasia in Barrett's esophagus using endoscopic optical coherence tomography," *Journal of Biomedical Optics*, vol. 11, pp. -, Jul-Aug 2006.
- [6] S. H. Yun, G. J. Tearney, B. J. Vakoc, M. Shishkov, W. Y. Oh, A. E. Desjardins, M. J. Suter, R. C. Chan, J. A. Evans, I. K. Jang, N. S. Nishioka, J. F. de Boer, and B. E. Bouma, "Comprehensive volumetric optical microscopy in vivo," *Nature Medicine*, vol. 12, pp. 1429-1433, Dec 2006.

### 3.2 Endoscopic Imaging of Barrett's Esophagus

Optical coherence tomography (OCT) is an emerging biomedical imaging technology which can generate high resolution, cross-sectional images of biological tissues *in situ* and in real time [1-3]. OCT can function as a type of optical biopsy to enable imaging of tissue microstructure with the resolution approaching that of standard excision biopsy, without the need of excising the tissue specimen [4-6]. One promising application of optical biopsy using OCT is the endoscopic imaging of the gastrointestinal (GI) tract. In contrast to conventional endoscopy, which can only visualize the surface alterations, OCT can detect changes in tissue morphology beneath the tissue surface. Therefore, endoscopic imaging with high resolution OCT could potentially improve the detection, visualization, and diagnosis of gastrointestinal diseases.

Several investigators have investigated endoscopic OCT (EOCT) imaging in the human gastrointestinal (GI) tract, including the esophagus and stomach, the small and large intestine, and the bile duct [7-17]. In addition to structural imaging, imaging of blood flow can also be performed using endoscopic Doppler OCT [18]. OCT imaging has demonstrated high sensitivities and specificities (100% sensitivity and 93% specificity in a retrospective study, 97% sensitivity and 92% specificity in a prospective study) for diagnosis of specialized intestinal metaplasia [19]. OCT imaging could also distinguish hyperplastic from adenomatous polyps in the colon [20]. The capability of OCT for detecting dysplasia in Barrett's esophagus was demonstrated recently. Evans et al. reported a sensitivity of 83% and specificity of 75% for detection of dysplasia with blinded scoring of OCT images [21]. And Isenberg et al. reported an accuracy of 78% for the detection of dysplasia in patients with Barrett's esophagus [22]. However, currently almost all clinical studies have been performed using standard OCT with 10-15  $\mu\text{m}$  resolution. Ultrahigh resolution OCT could enhance the imaging performance for the identification of early neoplastic changes, and could improve the sensitivity of biopsy by reducing false negative rates from sampling errors.

In order to achieve the high powers and short coherence lengths necessary for high resolution, high speed imaging, a Cr:Forsterite laser is used as the light source [23]. This laser generates broadband spectrum in the 1300 nm wavelength regime. The output bandwidth is increased by using nonlinear effects in optical fibers to yield a coherence length of 5  $\mu\text{m}$  or less. To match the optical dispersion within the system, dispersion-compensating glass (DCG) was inserted in the reference arm, and an air-gap coupling (AGC) was used in the sample arm. Due to the bandwidth limitations in the optical components in the sample and reference arms, the back-coupled spectrum on the detector has a bandwidth of 150 nm, which corresponds to a theoretical axial resolution of 4.6  $\mu\text{m}$  in air. The width of the measured axial point spread function is 5  $\mu\text{m}$ ; corresponding to  $\sim 4$   $\mu\text{m}$  resolution in the tissue, which is two- to three-fold times finer than standard OCT systems. With improvements in the bandwidth support of the optical components, higher axial resolutions could be achieved. The system sensitivity was 102 dB at 4 Hz frame rate with up to 15 mW power on the sample.

Ultrahigh-resolution (UHR) EOCT imaging was performed in the patients undergoing upper GI endoscopy at the Boston Veteran Affairs Medical Center (VAMC). Informed consent was obtained from patients enrolled under a protocol approved jointly by the Institutional Review Board (IRB) of Boston VAMC, the Committee on Human Studies at Harvard Medical School and the Committee on the Use of Humans as Experimental Subjects (COUHES) of Massachusetts Institute of Technology. The disinfected OCT imaging catheter was inserted through the accessory channel of the endoscope. While in the field of view of the endoscope, the OCT imaging catheter was positioned to the areas of interest by maneuvering the tip of the endoscope. The side of the distal end of the catheter was placed in gentle contact with the tissue surface during image acquisition to maintain mechanical stability for minimizing motion artifacts. The internal optics of the catheter was rotated so the OCT image plane was perpendicular into the tissue surface. A visible wavelength (670 nm) light source served as an aiming beam to facilitate the visualization and identification of the OCT imaging plane.

A total of 84 patients with previous history of Barrett's esophagus were imaged. Images from both normal and abnormal areas in the upper GI tract were acquired and later classified according to the results of pinch biopsy histology. The pathologic diagnoses from biopsy specimens included: Barrett's esophagus without dysplasia, indefinite for dysplasia, low-grade dysplasia, high-grade dysplasia, and adenocarcinoma.

Figure 3.6 shows the representative UHR EOCT images of normal esophagus and different pathological stages during the cancer progression. Figure 3.6(A) shows normal esophagus which has the characteristic layered architecture. OCT reveals the relatively homogeneous epithelium (ep), the high-backscattering band (brighter) of the lamina propria (lp), the low-backscattering (darker) muscularis mucosae (mm), the high-backscattering submucosa (sm), and the low-backscattering and thick muscularis propria (mp). Figure 3.6(B) shows a representative OCT image of Barrett's esophagus, a pre-malignant condition. OCT image of Barrett's esophagus demonstrate clear differences in the tissue architecture when compared to the normal esophageal squamous mucosa. The horizontally layered esophageal squamous epithelium is replaced by the presence of glandular architectures, which are more heterogeneous when compared to the normal esophagus. Low-backscattering Barrett's glands are frequently observed within Barrett's mucosa, with interlaced regions of high-backscattering connective tissue corresponding to the lamina propria. The deeper horizontal stratified muscularis mucosae and submucosal layers of the normal esophagus are preserved in patients with Barrett's esophagus. Figure 3.6(C) shows an example of UHR EOCT image of high-grade dysplasia. OCT images of high-grade dysplasia are characterized by irregular, distorted, and cribriform or villiform glandular architecture and are more heterogeneous than in non-dysplastic Barrett's epithelium. The epithelial-stromal interface appears more irregular. Figure 3.6(D) shows UHR EOCT image of esophageal adenocarcinoma. UHR EOCT images acquired along the margins of the lesion exhibited epithelial disruption and pronounced stromal infiltration extending from the superficially ulcerated carcinoma.

OCT images show progressive increase in architectural irregularity from Barrett's esophagus to high-grade dysplasia and eventually to adenocarcinoma. We are currently working in collaboration with Dr. Andrews Rollins from Case Western Reserve University on the application of computer-aid-diagnosis algorithm for detection of high-grade dysplasia in Barrett's esophagus []. The improved image resolution of OCT enabled the visualization of architectural morphology features such as the normal layered structure of the epithelium versus glandular and columnar structures associated with Barrett's esophagus more clearly. And the improved image resolution and reduced speckle noise should improve algorithm performance. Further and more detailed investigations using ultrahigh resolution OCT imaging in clinical endoscopic studies will be necessary to evaluate the ultimate impact of improved resolution on the diagnostic capabilities for detecting Barrett's esophagus associated high-grade dysplasia and carcinoma. In the context of surveillance of patients with Barrett's for high grade dysplasia and adenocarcinoma, the most intriguing application of OCT would be to direct excisional biopsy to reduce sampling errors. This

could improve sensitivity of diagnosis, reduce the cost of surveillance and provide enhanced diagnosis and treatment decisions.

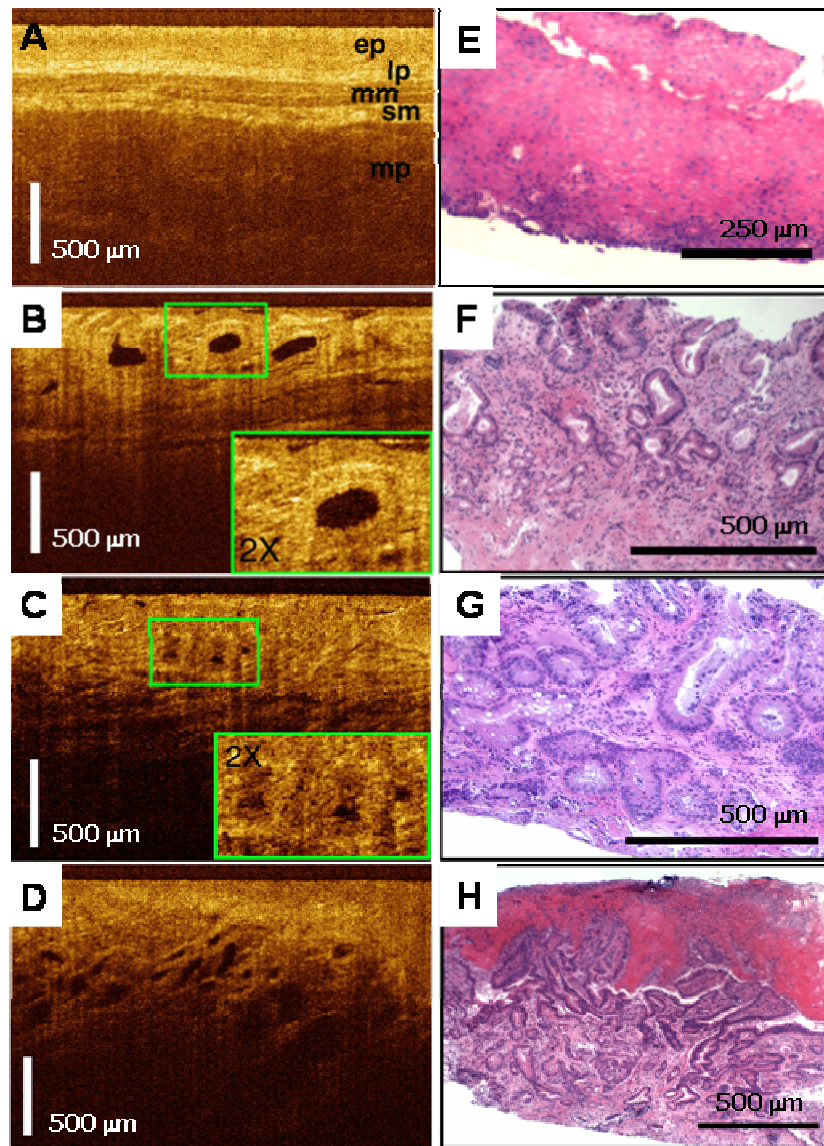


**Figure 3.6.** A-D: In vivo ultrahigh-resolution endoscopic OCT images of normal esophagus and representative pathological stages during cancer progression. A: normal esophagus; B: Barrett's esophagus; C: High-grade dysplasia; D: Adenocarcinoma. E-F: Corresponding histology with the OCT images to the left.

Another important clinical niche for OCT is to evaluate the subsurface abnormalities after the ablation therapy. Currently one of the clinical concerns associated with ablation therapies (such as argon plasma coagulation – APC [24], photodynamic therapy – PDT [25], and radiofrequency ablation [26]) is the residual metaplastic epithelium under the neosquamous epithelium (so called 'buried glands') [27]. A significant portion (~ 20% - 30%) of patients followed up after APC and PDT showed the presence of buried glands [24, 27]. This might be associated with risks of adenocarcinoma under the neosquamous epithelium [28, 29]. Since Barrett's epithelium located

beneath squamous epithelium can be missed in standard endoscopic surveillance, which depends on surface features to identify suspicious areas for biopsy.

Visualization of submucosal features is a key advantage of OCT imaging when compared to standard endoscopy. Figure 3.7(A) shows a case of esophageal adenocarcinoma underneath benign squamous epithelium in a patient 15 months after PDT. The irregularly backscattering neoplastic mucosa of the adenocarcinoma is dramatically different from that of normal and Barrett's esophagus. OCT images of adenocarcinoma show irregularly shaped and crowded glandular architecture buried underneath the smooth squamous epithelium, as confirmed by histology (Figure 3.7(B)). Figure 3.7(C) shows an OCT image of a patient 6 months after the bipolar radiofrequency ablation therapy. OCT reveals squamous neo-epithelium similar to that observed from normal esophagus. However, underneath the smooth-appearing epithelium, glandular structures characteristic of Barrett's esophagus can be visualized. The presence of subsquamous Barrett's is confirmed by the corresponding histology (Figure 3.7(D)). Endoscopic OCT allows real-time in vivo imaging of subsurface tissue morphology which is uniquely qualified for assessment and surveillance of treatment efficacy after ablation therapy, suggesting that OCT could be a promising non-invasive tool in evaluation of treatment effects, and for real time guidance of focal ablation during follow-up endoscopy.

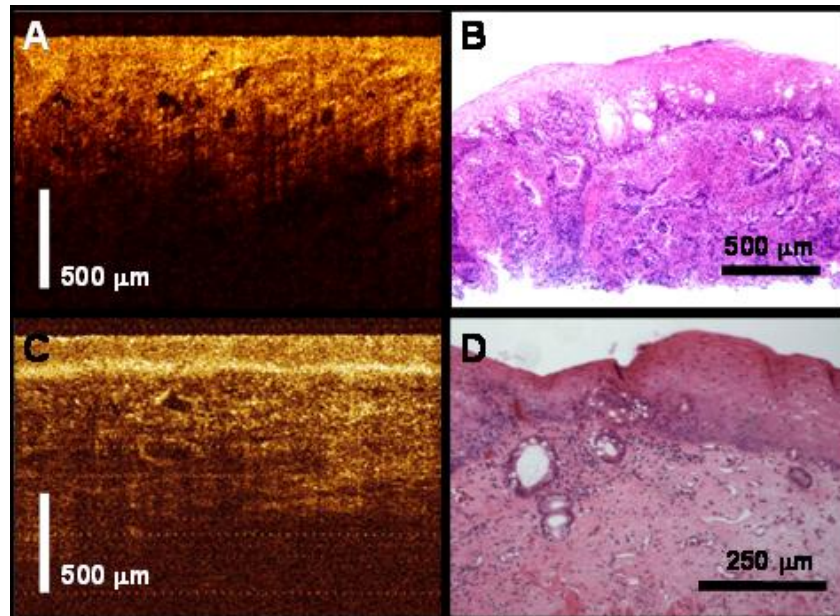


**Figure 3.7.** A: In vivo ultrahigh-resolution endoscopic OCT imaging of adenocarcinoma under the squamous epithelium from a patient status post PDT. B: Corresponding histology. C: In vivo ultrahigh-resolution endoscopic OCT imaging of Barrett's epithelium buried underneath the neosquamous epithelium from a patient status post radiofrequency ablation. D: Corresponding histology.

## References

- [1] D. Huang, E. A. Swanson, C. P. Lin, J. S. Schuman, W. G. Stinson, W. Chang, M. R. Hee, T. Flotte, K. Gregory, C. A. Puliafito, and J. G. Fujimoto, "Optical Coherence Tomography," *Science*, vol. 254, pp. 1178-1181, Nov 22 1991.
- [2] J. M. Schmitt, "Optical coherence tomography (OCT): a review," *IEEE Journal of Selected Topics in Quantum Electronics*, vol. 5, pp. 1205-15, 1999/07/ 1999.

- [3] J. G. Fujimoto, "Optical coherence tomography for ultrahigh resolution in vivo imaging," *Nature Biotechnology*, vol. 21, pp. 1361-1367, Nov 2003.
- [4] J. G. Fujimoto, M. E. Brezinski, G. J. Tearney, S. A. Boppart, B. Bouma, M. R. Hee, J. F. Southern, and E. A. Swanson, "Optical biopsy and imaging using optical coherence tomography," *Nature Medicine*, vol. 1, pp. 970-972, Sep 1995.
- [5] M. E. Brezinski, G. J. Tearney, B. E. Bouma, J. A. Izatt, M. R. Hee, E. A. Swanson, J. F. Southern, and J. G. Fujimoto, "Optical coherence tomography for optical biopsy. Properties and demonstration of vascular pathology," *Circulation*, vol. 93, pp. 1206-13, Mar 15 1996.
- [6] J. G. Fujimoto, C. Pitris, S. A. Boppart, and M. E. Brezinski, "Optical coherence tomography: an emerging technology for biomedical imaging and optical biopsy," *Neoplasia*, vol. 2, pp. 9-25, Jan-Apr 2000.
- [7] A. M. Sergeev, V. M. Gelikonov, G. V. Gelikonov, F. I. Feldchtein, R. V. Kuranov, N. D. Gladkova, N. M. Shakhova, L. B. Suopova, A. V. Shakhov, I. A. Kuznetzova, A. N. Denisenko, V. V. Pochinko, Y. P. Chumakov, and O. S. Streltzova, "In vivo endoscopic OCT imaging of precancer and cancer states of human mucosa," *Optics Express*, vol. 1, 1997/12/22 1997.
- [8] B. E. Bouma, G. J. Tearney, C. C. Compton, and N. S. Nishioka, "High-resolution imaging of the human esophagus and stomach in vivo using optical coherence tomography," *Gastrointestinal endoscopy*, vol. 51(4) Pt 1, pp. 467-74, Apr 2000.
- [9] M. V. Sivak, Jr., K. Kobayashi, J. A. Izatt, A. M. Rollins, R. Ung-Runyawee, A. Chak, R. C. Wong, G. A. Isenberg, and J. Willis, "High-resolution endoscopic imaging of the GI tract using optical coherence tomography," *Gastrointestinal endoscopy*, vol. 51(4) Pt 1, pp. 474-9, Apr 2000.
- [10] S. Jäckle, N. Gladkova, F. Feldchtein, A. Terentieva, B. Brand, G. Gelikonov, V. Gelikonov, A. Sergeev, A. Fritscher-Ravens, J. Freund, U. Seitz, S. Schröder, and N. Soehendra, "In vivo endoscopic optical coherence tomography of esophagitis, Barrett's esophagus, and adenocarcinoma of the esophagus," *Endoscopy*, vol. 32, pp. 750-5, Oct 2000.
- [11] S. Jäckle, N. Gladkova, F. Feldchtein, A. Terentieva, B. Brand, G. Gelikonov, V. Gelikonov, A. Sergeev, A. Fritscher-Ravens, J. Freund, U. Seitz, S. Soehendra, and N. Schrödern, "In vivo endoscopic optical coherence tomography of the human gastrointestinal tract--toward optical biopsy," *Endoscopy*, vol. 32, pp. 743-9, Oct 2000.
- [12] S. Brand, J. M. Ponerros, B. E. Bouma, G. J. Tearney, C. C. Compton, and N. S. Nishioka, "Optical coherence tomography in the gastrointestinal tract," *Endoscopy*, vol. 32, pp. 796-803, Oct 2000.
- [13] X. D. Li, S. A. Boppart, J. Van Dam, H. Mashimo, M. Mutinga, W. Drexler, M. Klein, C. Pitris, M. L. Krinsky, M. E. Brezinski, and J. G. Fujimoto, "Optical coherence tomography: advanced technology for the endoscopic imaging of Barrett's esophagus," *Endoscopy*, vol. 32, pp. 921-30, Dec 2000.
- [14] G. Zuccaro, N. Gladkova, J. Vargo, F. Feldchtein, E. Zagaynova, D. Conwell, G. Falk, J. Goldblum, J. Dumot, J. Ponsky, G. Gelikonov, B. Davros, E. Donchenko, and J. Richter, "Optical coherence tomography of the esophagus and proximal stomach in health and disease," *The American journal of gastroenterology*, vol. 96, pp. 2633-9, Sep 2001.
- [15] B. Shen, G. Zuccaro, Jr., T. L. Gramlich, N. Gladkova, P. Trolli, M. Kareta, C. P. Delaney, J. T. Connor, B. A. Lashner, C. L. Bevins, F. Feldchtein, F. H. Remzi, M. L. Bambrick, and V. W. Fazio, "In vivo colonoscopic optical coherence tomography for transmural inflammation in inflammatory bowel disease," *Clin Gastroenterol Hepatol*, vol. 2, pp. 1080-7, Dec 2004.
- [16] U. Seitz, J. Freund, S. Jaeckle, F. Feldchtein, S. Bohnacker, F. Thonke, N. Gladkova, B. Brand, S. Schröder, and N. Soehendra, "First in vivo optical coherence tomography in the human bile duct," *Endoscopy*, vol. 33, pp. 1018-21, Dec 2001.
- [17] J. M. Ponerros, G. J. Tearney, M. Shiskov, P. B. Kelsey, G. Y. Lauwers, N. S. Nishioka, and B. E. Bouma, "Optical coherence tomography of the biliary tree during ERCP," *Gastrointestinal endoscopy*, vol. 55, pp. 84-8, Jan 2002.

- [18] V. X. Yang, S. J. Tang, M. L. Gordon, B. Qi, G. Gardiner, M. Cirocco, P. Kortan, G. B. Haber, G. Kandel, I. A. Vitkin, B. C. Wilson, and N. E. Marcon, "Endoscopic Doppler optical coherence tomography in the human GI tract: initial experience," *Gastrointest Endosc*, vol. 61, pp. 879-90, Jun 2005.
- [19] J. M. Poneros, S. Brand, B. E. Bouma, G. J. Tearney, C. C. Compton, and N. S. Nishioka, "Diagnosis of specialized intestinal metaplasia by optical coherence tomography," *Gastroenterology*, vol. 120, pp. 7-12, Jan 2001.
- [20] P. R. Pfau, M. V. Sivak, Jr., A. Chak, M. Kinnard, R. C. Wong, G. A. Isenberg, J. A. Izatt, A. Rollins, and V. Westphal, "Criteria for the diagnosis of dysplasia by endoscopic optical coherence tomography," *Gastrointest Endosc*, vol. 58, pp. 196-202, Aug 2003.
- [21] J. A. Evans, J. M. Poneros, B. E. Bouma, J. Bressner, E. F. Halpern, M. Shishkov, G. Y. Lauwers, M. Mino-Kenudson, N. S. Nishioka, and G. J. Tearney, "Optical coherence tomography to identify intramucosal carcinoma and high-grade dysplasia in Barrett's esophagus," *Clinical Gastroenterology and Hepatology*, vol. 4, pp. 38-43, Jan 2006.
- [22] G. Isenberg, M. V. Sivak, A. Chak, R. C. K. Wong, J. E. Willis, B. Wolf, D. Y. Rowland, A. Das, and A. Rollins, "Accuracy of endoscopic optical coherence tomography in the detection of dysplasia in Barrett's esophagus: a prospective, double-blinded study," *Gastrointestinal Endoscopy*, vol. 62, pp. 825-831, Dec 2005.
- [23] P. R. Herz, Y. Chen, A. D. Aguirre, J. G. Fujimoto, H. Mashimo, J. Schmitt, A. Koski, J. Goodnow, and C. Petersen, "Ultra-high resolution optical biopsy with endoscopic optical coherence tomography," *Optics Express*, vol. 12, pp. 3532-3542, JUL 26 2004.
- [24] J. P. Byrne, G. R. Armstrong, and S. E. A. Attwood, "Restoration of the normal squamous lining in Barrett's esophagus by argon beam plasma coagulation," *American Journal of Gastroenterology*, vol. 93, pp. 1810-1815, Oct 1998.
- [25] B. F. Overholt, M. Panjehpour, and J. M. Haydek, "Photodynamic therapy for Barrett's esophagus: follow-up in 100 patients," *Gastrointestinal Endoscopy*, vol. 49, pp. 1-7, Jan 1999.
- [26] V. K. Sharma, K. K. Wang, B. F. Overholt, C. J. Lightdale, M. B. Fennerty, P. J. Dean, D. K. Pleskow, R. Chuttani, A. Reymunde, N. Santiago, K. J. Chang, M. B. Kimmey, and D. E. Fleischer, "Balloon-based, circumferential, endoscopic radiofrequency ablation of Barrett's esophagus: 1-year follow-up of 100 patients," *Gastrointestinal Endoscopy*, vol. 65, pp. 185-195, Feb 2007.
- [27] C. J. Kelty, R. Ackroyd, N. J. Brown, T. J. Stephenson, C. J. Stoddard, and M. W. R. Reed, "Endoscopic ablation of Barrett's oesophagus: a randomized-controlled trial of photodynamic therapy vs. argon plasma coagulation," *Alimentary Pharmacology & Therapeutics*, vol. 20, pp. 1289-1296, Dec 2004.
- [28] J. L. Van Laethem, M. O. Peny, I. Salmon, M. Cremer, and J. Deviere, "Intramucosal adenocarcinoma arising under squamous re-epithelialisation of Barrett's oesophagus," *Gut*, vol. 46, pp. 574-577, Apr 2000.
- [29] K. Raganath, N. Krasner, V. S. Raman, M. T. Haqqani, C. J. Phillips, and I. Cheung, "Endoscopic ablation of dysplastic Barrett's oesophagus comparing argon plasma coagulation and photodynamic therapy: A randomized prospective trial assessing efficacy and cost-effectiveness," *Scandinavian Journal of Gastroenterology*, vol. 40, pp. 750-758, Jun 2005.

### 3.3 OCT Imaging of Kidney Microanatomy Ex Vivo

Most of the kidneys used for kidney transplantation are obtained from heart-beating cadavers. To date, there is no reliable way to determine the viability of donor kidneys. Tandem scanning confocal microscopy (TSCM) can provide non-invasive imaging of superficial uriniferous tubules of kidney, and has the potential of evaluating the status of donor kidney prior to their transplantation [1]. Optical coherence tomography (OCT) offers better penetration depth than confocal microscopy. In the present study, we explored the feasibility and evaluated the capability of high-resolution OCT technology to image normal kidneys as well as kidneys that had been subjected to an ischemic or toxic insult.

The OCT imaging system used in this study was a research prototype based on a commercial OCT system (Lightlab Imaging, Inc., MA, USA) that was modified for ultrahigh resolution performance [2]. Imaging was performed using a special broadband laser source consisting of a compact femtosecond Cr<sup>4+</sup>:Forsterite laser combined with nonlinear spectral broadening in a dispersion-shifted fiber to generate a 180-nm bandwidth at a center wavelength of 1260 nm with 50-mW output power. Dispersion compensating glasses were inserted in the reference arm to compensate for the collimating and focusing optics in the sample arm, and an air gap coupling was used in the sample arm to compensate for the air path in the reference arm from the collimator to the scanning delay mirror. An axial resolution of 4.6  $\mu\text{m}$  in air ( $\sim 3.3 \mu\text{m}$  in tissue) was achieved. The average optical power incident on the tissue was  $\sim 10$  mW. The system detection sensitivity was measured to be 102 dB. The system used a high-speed scanning delay line that acquires 3,125 axial scans per second. Imaging was performed using a fiber-based collimator combined with a microlens that produces a transverse spot size of 6  $\mu\text{m}$  full width at half maximum (FWHM). The collimator and microlens unit was raster (XY) scanned by two precisely controlled stages (Physik Instrumente GmbH & Co. KG, Karlsruhe, Germany). Individual cross-sectional OCT images (XZ) were generated at a rate of 2 frames per second with the dimension of 3 mm in length (600 pixels) and 2.5 mm in depth (1,600 pixels). Consecutive OCT images in different planes along Y direction were scanned with 3- $\mu\text{m}$  separation to generate a three-dimensional (3D) volume. The three-dimensional (3D) OCT data was processed and visualized using a 3D visualization and volumetric rendering software package (Amira, Mercury Computer Systems, Inc., Berlin, Germany). The software allowed the generation of three-dimensional volumetric views and en face (XY) views.

Figure 3.8(A) presents a cross-sectional OCT image of an intact rat kidney that was protected from ischemia by prior infusion of sucrose. The uriniferous tubule lumens appeared low backscattering (dark region) while the parenchyma appeared high backscattering (bright region). An en face image can be reconstructed from consecutive cross-sectional images as shown in Figure 3.8(B). The lumens appear wide open. Rendered OCT images using 3D visualization and volumetric rendering software provided three-dimensional cut-open view in Figure 3.8(C). In contrast, there was a significant difference in OCT images between those (Figure 3.8(A-C)) and those that received no protection (i.e., no sucrose) prior to the ischemic insult (Figure 3.9(A-C)). The latter (i.e., unprotected kidneys) revealed patches where tubules had lumens either entirely or partially filled with cytoplasmic debris. Although evident in the cross-sectional image (Figure 3.9(A)), this change was more dramatic when viewed in the en face image (Figures 3.9(B-C)). For comparative purposes, histology images of normal, protected kidney and the unprotected, ischemic kidneys are presented in Figures 3.8(D) and 3.9(D), respectively.

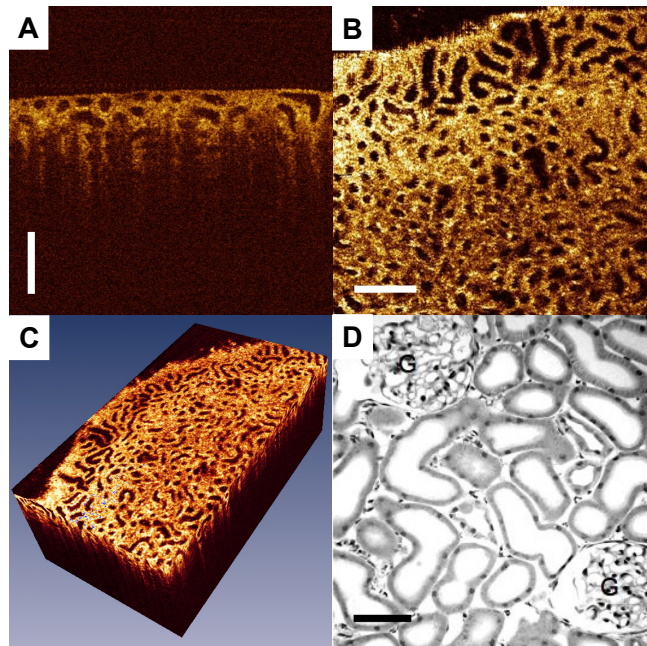


**Figure 3.8.** OCT images of a rat kidney that was protected from one hour of ischemic insult due to prior infusion of sucrose. A: Cross-sectional image (bar: 250  $\mu\text{m}$ ). B: En face image (bar: 250  $\mu\text{m}$ ). C: Three-dimensional view (size: 2.1 mm in length x 1.0 mm in width x 0.8 mm in height). D: Plastic embedded light microscopic section image (bar: 75  $\mu\text{m}$ ).

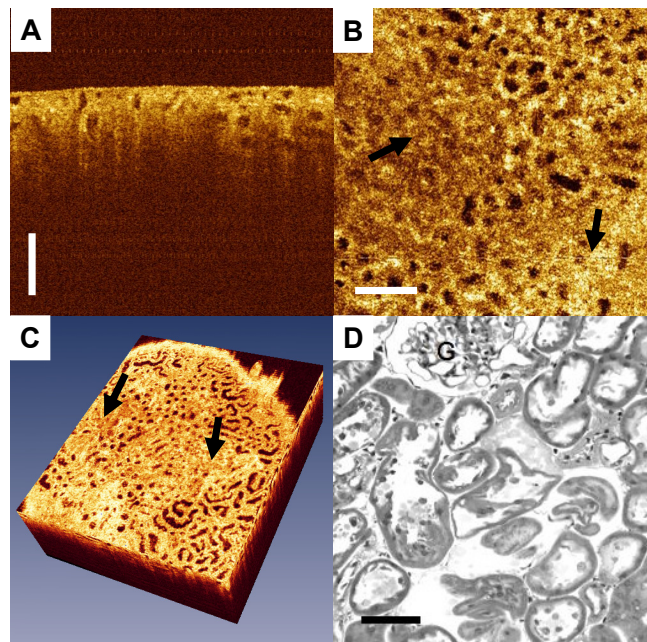


**Figure 3.9.** OCT images of a kidney that was subjected to 1 hour of ischemia followed by 5 minutes of recovery. A: Cross-sectional image (bar: 250  $\mu\text{m}$ ). B: En face image (bar: 250  $\mu\text{m}$ ). C: Three-dimensional view (size: 2.0 mm in length x 1.7 mm in width x 0.8 mm in height). D: Plastic embedded light microscopic section image (bar: 75  $\mu\text{m}$ ).

OCT images of kidneys subjected to mercury toxicity revealed regions devoid of tubule lumens due to accumulated cytoplasmic debris and casts. Other tubules exhibit distended lumens due to distal tubule blockage (Figure 3.10(A-C)). It is, nevertheless, difficult to distinguish between the distal and proximal convoluted tubules in these images. The foregoing OCT images correlate with light microscopic images of these kidneys showing debris in selected proximal convoluted tubules, distal tubule casts and distended lumens following the mercuric chloride insult (Figure 3.10(D)).

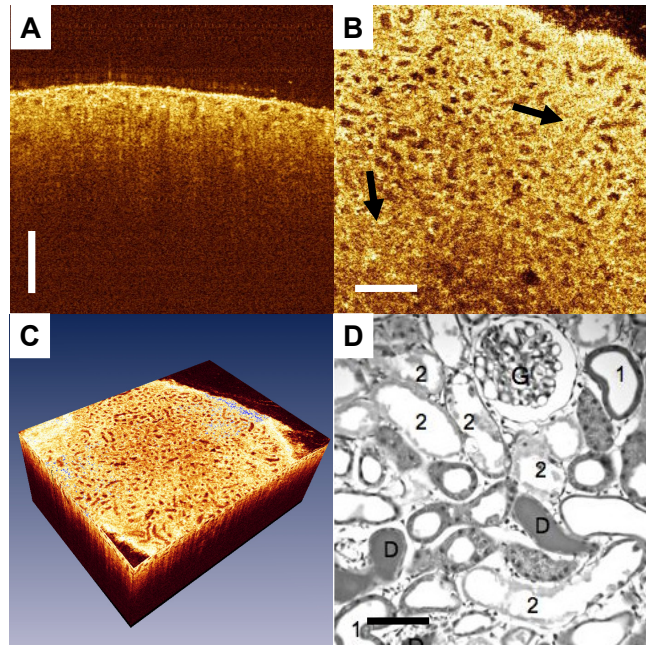


**Figure 3.10.** OCT images of a kidney 48 hours following infusion of mercuric chloride (1mg/kg). A: Cross-sectional image (bar: 250  $\mu\text{m}$ ). B: En face image (bar: 250  $\mu\text{m}$ ). C: Three-dimensional view (size: 2.1 mm in length x 1.6 mm in width x 0.8 mm in height). D: Plastic embedded light microscopic section image (bar: 100  $\mu\text{m}$ ).

The OCT imaging in this preliminary study is performed on ex vivo samples. This eliminates the motion artifacts, since the acquisition speed is limited (2 frames per second). However, with recent advances in OCT imaging technology using spectral/Fourier domain detection, dramatic improvements (~100 fold) in imaging speed are possible [3]. These high imaging speeds would enable 3D OCT of kidney microanatomy in vivo. Future studies will involve the high-speed imaging of kidney functional changes due to ischemia in vivo, and the correlation of OCT imaging parameters with post-transplantation kidney functions.

## References

- [1] P. M. Andrews, B. S. Khirabadi, and B. C. Bengs, "Using tandem scanning confocal microscopy to predict the status of donor kidneys," *Nephron*, vol. 91, pp. 148-155, May 2002.
- [2] P. R. Herz, Y. Chen, A. D. Aguirre, J. G. Fujimoto, H. Mashimo, J. Schmitt, A. Koski, J. Goodnow, and C. Petersen, "Ultra-high resolution optical biopsy with endoscopic optical coherence tomography," *Optics Express*, vol. 12, pp. 3532-3542, JUL 26 2004.
- [3] R. Huber, M. Wojtkowski, J. G. Fujimoto, J. Y. Jiang, and A. E. Cable, "Three-dimensional and C-mode OCT imaging with a compact, frequency swept laser source at 1300 nm," *Optics Express*, vol. 13, pp. 10523-10538, Dec 22 2005.

## 4. Optical Coherence Microscopy

### Sponsors

National Institutes of Health – R01-CA75289-08

National Science Foundation – BES-0522845, BES-0119494

Air Force Office of Scientific Research FA9550-040-1-0011, FA9550-040-1-0046

Cancer Research and Prevention Foundation

Whitaker Foundation

### Project Staff

Shu-Wei Huang, Dr. Aaron D. Aguirre, Dr. Robert Huber, Desmond C. Adler, Dr. Yu Chen, Professor James G. Fujimoto

Ultrahigh-resolution optical coherence tomography (OCT) can achieve 1-2  $\mu\text{m}$  axial resolution in tissue, but is limited in transverse resolution due to the low numerical aperture (NA) focusing to maintain a sufficient depth of field over the range of the cross-sectional image [1]. The relatively low lateral resolution achievable with cross-sectional OCT is generally insufficient for imaging of cellular features and therefore limits the utility of OCT in applications requiring cellular level diagnostics. To extend the imaging power of Optical coherence tomography to very high transverse resolution, we are developing a technology known as Optical coherence microscopy (OCM), which combines Optical coherence tomography with confocal microscopy. Figure 4.1 compares the image penetration depth and resolution of OCM with that of OCT and confocal microscopy. OCM can provide enhanced penetration depth compared to standard confocal microscopy while dramatically improving the resolution over typical cross-sectional OCT imaging methods.

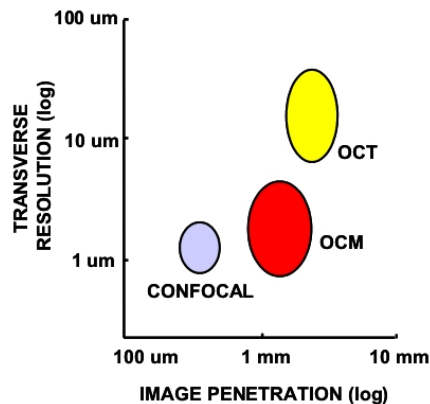


**Figure 4.1.** Transverse resolution and image penetration in optical coherence microscopy (OCM). OCM can dramatically enhance image penetration compared to confocal microscopy alone while significantly improving transverse resolution in OCT to enable cellular level imaging.

Optical coherence microscopy overcomes the depth of field limitation present in traditional OCT imaging by imaging in the *en face* plane rather than the cross-sectional plane. To image *en face*, the optical path length of the reference arm is matched exactly to the focus of the sample arm microscope while scanning a transverse raster pattern on the tissue. This eliminates the need for path length scanning to generate an axial depth map and allows the use of high NA lenses to provide very small spot sizes. Because of the high NA focusing used in OCM, the field of view in the images is necessarily smaller than in OCT. OCT images architectural features over a field of view of 3-6 mm square while OCM can image down to the cellular level but with reduced field of view of 100 – 500  $\mu\text{m}$  square.

OCM has the unique advantage of using two distinct optical sectioning techniques – confocal gating and coherence gating. While the confocal point spread function is entirely determined by the numerical aperture of the final objective lens, the coherence gate is determined by the light source bandwidth. The degree of confocal rejection of unfocused scattered light can be varied by changing the numerical aperture of the objective lens while the amount of coherence gated sectioning can be varied by changing the bandwidth of the light source. The multiplicative effect of the two sectioning methods strengthens the overall optical sectioning power, allowing increased rejection of unwanted, out of focus scattered light. Studies from our group as well as others have demonstrated that combined confocal and coherence gating can provide improved imaging depth compared to confocal alone [2-4]. The addition of high sensitivity coherence gated detection to confocal detection extends the imaging depth in scattering media to the shot noise quantum limit, providing a factor of 2-3 increase over standard confocal microscopy.

The use of multiple optical sectioning techniques also allows considerable flexibility in system design for achieving high-resolution cellular images. Broad bandwidth light sources as used in ultrahigh resolution OCT can provide thin optical sectioning via coherence gating, and the confocal sectioning can be relaxed to facilitate development of miniaturized imaging devices.

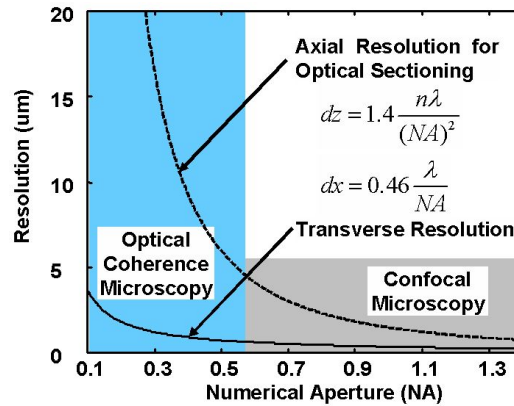


**Figure 4.2.** Numerical aperture requirement for OCM compared to confocal microscopy. OCM can image with high transverse resolution at much lower numerical aperture than confocal microscopy because it does not depend on high axial resolution for optical sectioning.

Figure 4.2 compares the confocal axial and transverse imaging resolution as a function of the numerical aperture of the probe optics to demonstrate this operating limit for OCM. The axial section thickness degrades much more quickly than the transverse resolution, and there exists a region where the transverse resolution is sufficient for cellular imaging but the axial resolution is not. Addition of a short coherence gate to provide tissue sectioning can therefore make cellular imaging possible with much lower NA than is sufficient for confocal microscopy alone. This operating regime for OCM imaging has very important clinical implications, since it promises to allow cellular imaging with small diameter probes compatible with standard endoscopic and laparoscopic procedures.

#### References

- [1] W. Drexler, U. Morgner, F. X. Kartner, C. Pitris, S. A. Boppart, X. D. Li, E. P. Ippen, and J. G. Fujimoto, *Optics Letters* **24** (1999) 1221.
- [2] J. A. Izatt, M. R. Hee, G. M. Owen, E. A. Swanson, and J. G. Fujimoto, *Optics Letters* **19** (1994) 590.
- [3] J. A. Izatt, M. D. Kulkarni, H.-W. Wang, K. Kobayashi, and M. V. Sivak, Jr., *IEEE Journal of Selected Topics in Quantum Electronics* **2** (1996) 1017.
- [4] M. Kempe, W. Rudolph, and E. Welsch, *Journal of the Optical Society of America A-Optics Image Science and Vision* **13** (1996) 46.

#### 4.1 Swept source OCM

Traditionally, OCM is implemented with time domain detection, which allows high speed *en face* imaging in order to eliminate motion artifacts [1, 2]. However, time domain systems have a number of features that make the optical system undesirably complex. First, a rapid phase modulation scheme in the reference arm is required for time domain OCM systems. Several methods have been proposed, including rapid scanning optical delay lines [2], electro-optic modulators [3, 4], and acousto-optic modulators [5, 6]. All of these methods require sophisticated optical designs and specific issues such as scanner synchronization and dispersion compensation need to be carefully addressed. Second, spatial overlap between the coherence gate and confocal gate is critical to ensure optimal image quality in highly scattered tissues. Due to the inhomogeneous nature of tissues, the matching between the two gates generally cannot be set *a priori* without real time measurement. In addition, when a fiber based endoscope system is used, any variation of stress in the fiber can introduce gate mismatch and degrade the image quality. Therefore, a feedback loop and a fast coordination algorithm are required to maintain optimal image quality during the imaging period. Finally, due to the limited field of view, usually a few hundred  $\mu\text{m}$ , OCM itself can suffer from sampling error in clinical studies. One solution to this limitation is to use optical coherence tomography (OCT) for large-scale survey and to conduct OCM only in the regions where abnormalities are detected using OCT. An imaging modality which incorporates high speed OCT and OCM is thus desirable. However, due to differences between time domain OCT and OCM system designs, it is challenging to achieve both high-speed OCT and OCM in one system.

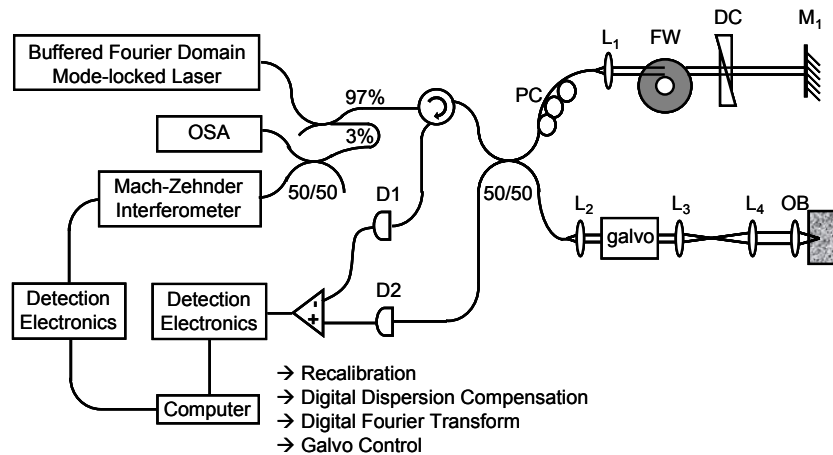


**Figure 4.3.** Schematic of the swept source OCM system. L1-L4, lenses; M1, mirror; OB, water-immersion objective; D1-D2, dual-balanced photodetectors; FW, neutral density filter wheel; DC, dispersion compensating glass.

Swept source/Fourier domain OCM is a new technique and has several advantages compared to time domain OCM. First, it more easily enables integration with OCT. Figure 4.3 is a schematic diagram of the swept source OCM system developed by our group. Different from time domain OCM, which acquires only a single *en face* image, swept source/Fourier domain OCM generates an image by acquiring an entire 3D volume and rendering the *en face* plane. Figure 4.4(A) shows an *in vivo* volumetric image of a *Xenopus laevis* tadpole, a commonly used model organism for developmental biology studies. The 3D dataset is post-processed to generate a series of *en face* images at different depths near the focal plane. Three representative *en face* images  $\sim 12 \mu\text{m}$  apart in depth from each other are shown in Fig. 4.4(B), 2(C), and 2(D). Degradation of transverse resolution from Fig. 4.4(C) to Fig. 4.4(D) is apparent due to the finite depth of field with  $\sim 0.35$  NA objective. The ability to generate images at different depths covering the entire focal range within one acquisition circumvents the need of online coordination between coherence gate

and confocal gate. In contrast, for time domain OCM, only one *en face* image is acquired at a time and therefore precise control of the position of the coherence gate is required to ensure optimal image quality. Besides, OCM and OCT using swept source/Fourier domain detection has the advantage of sharing the same optics in the reference arm, which makes integration of the two techniques relatively straightforward. An imaging modality which can be easily switched between high speed OCT for large-scale survey imaging and OCM for a detailed cellular level examination would be a powerful modality for optical biopsy and facilitate clinical studies. Swept source/Fourier domain OCM also has the advantage of reduced system complexity. Rapid phase modulators in time domain OCM system is not required in swept source/Fourier domain OCM.

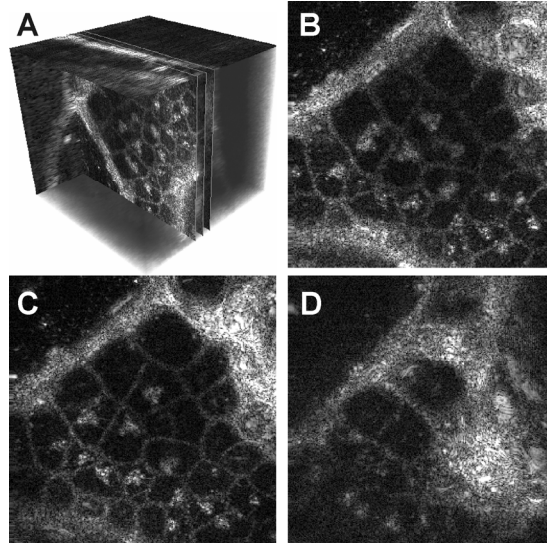


**Figure 4.4.** Extraction of *en face* images from the 3D dataset. A. A volumetric image acquired by the swept source OCM system in  $\sim 1.5$  second. A series of *en face* images can then be extracted from the volume digitally. The volume size is  $\sim 220 \mu\text{m} \times 220 \mu\text{m} \times 220 \mu\text{m}$ . B, C, and D. Three representative *en face* images  $\sim 12 \mu\text{m}$  apart in depth from each other are extracted from the volume around the focus.

Although the data rate of swept source/Fourier domain OCM is higher than time domain OCM, the frame rate for an *en face* image at a particular depth is limited by the laser sweep rate. Unlike standard swept laser sources, the FDML laser [7] can operate at extremely high speeds and therefore enables rapid, swept source/Fourier domain OCM. FDML lasers overcome limitations of sweep speeds which are present in standard swept lasers and unprecedented high sweep rates up to 370 kHz have been demonstrated with a buffered configuration [8]. At these speeds,  $\sim 6$  Hz frame rate can be supported and motion artifacts for *in vivo* imaging can be minimized.

We have demonstrated initial imaging results at  $\sim 42$  kHz axial scan rates, corresponding to image acquisition times of  $\sim 1.5$  seconds. Image resolutions of  $1.6 \mu\text{m} \times 8 \mu\text{m}$  (transverse  $\times$  axial) with a  $220 \mu\text{m} \times 220 \mu\text{m}$  field of view and sensitivity higher than 98 dB are achieved. Figure 4.5 shows swept source OCM images and H&E stained histology of a fixed rat kidney, demonstrating the capability to image in highly scattered biological samples. Figures 4.5(A) and 4.5(B) are acquired when the focus is at  $\sim 40 \mu\text{m}$  and  $\sim 120 \mu\text{m}$  below the surface, respectively. The cell lining along the kidney tubules is readily visible and small regions of bright reflectivity, consistent with nuclei, can also be observed in the images. The ability to generate high quality cellular images in human tissue with the system is demonstrated in Fig. 4.6. Figure 4.6(A) is a swept source OCM image of a normal human colonic mucosa taken at  $\sim 100 \mu\text{m}$  below the surface while Fig. 4.6(B) is H&E stained histology. Mucosal specimens can exhibit changes in optical properties with fixation, so the sample was preserved in phosphate-buffered saline (PBS) and imaged within 6 hours of excision, then fixed and processed for histology. Normal colonic mucosa shows the

presence of round crypts with goblet cells inside epithelium lining the lumen. In addition, the lamina propria houses many lymphoid cells. All features mentioned above can be clearly resolved in the swept source OCM image. Figures 4.6(C) and 4.6(D) are images of a different region at  $\sim 100 \mu\text{m}$  and  $\sim 150 \mu\text{m}$  below the surface, respectively. A decrease of lumen size with depth is apparent and detailed structures such as goblet cells and lymphoid cells can still be easily identified deep in the tissue.

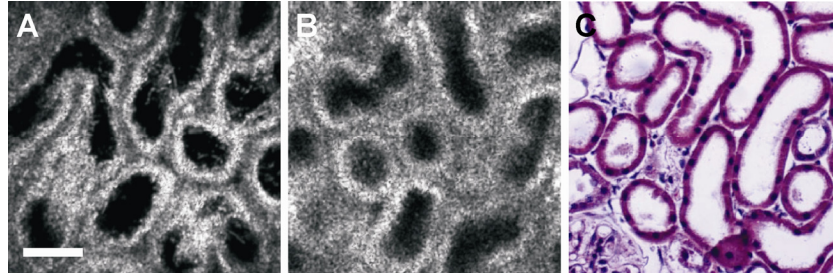


**Figure 4.5.** Cellular images of a fixed rat kidney. A, B. OCM images at  $\sim 40 \mu\text{m}$  and  $\sim 120 \mu\text{m}$  below the surface, respectively. C. Representative histology stained with H&E. The cell lining along the kidney tubules and nuclei can be observed. Scale bar:  $50 \mu\text{m}$ .

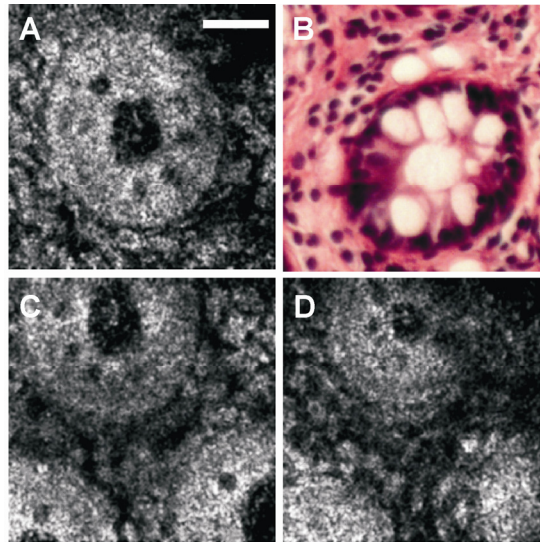


**Figure 4.6.** Cellular images of an unfixed human colonic mucosa. A. OCM image of a single crypt structure at  $\sim 100 \mu\text{m}$  below the surface. B. Representative histology stained with H&E. C, D. OCM images of a different region at  $\sim 100 \mu\text{m}$  and  $\sim 150 \mu\text{m}$  below the surface, respectively. Features like round crypts, goblet cells, epithelium lining the lumen, lymphoid cells in the lamina propria, and lumen shrinkage over depth can be resolved. Scale bar:  $50 \mu\text{m}$ .

The imaging speed is currently limited by the data acquisition and processing hardware, but has the potential to be significantly increased, enabling *in vivo* imaging and real-time display. To fully utilize the laser's high sweep rate and dynamically display an *en face* image of interest, an analog demodulation scheme should be developed so that the digital processing requirements can be minimized. Unfortunately, because of the nonlinear frequency sweep of the FDML laser, a simple band-pass filter is not sufficient to demodulate a particular *en face* image from the 3D dataset. However, matched filter approaches should be possible and promises to enable very high demodulation speeds. In terms of real-time processing and display, time domain OCM approaches are currently easier to implement. Toward improving resolution, we have recently developed FDML lasers with full tuning ranges of  $\sim 170 \text{ nm}$  using specially matched

semiconductor optical amplifier (SOA). This suggests that axial resolutions can be improved to  $\sim 5$   $\mu\text{m}$ , which is comparable to the thickness of standard histological sections. Furthermore, the superior phase stability of the buffered FDML laser compared with other frequency swept lasers promises to enable real-time phase microscopy with phase sensitivity compatible to spectral / Fourier domain systems [9].

## References

- [1] J. A. Izatt, M. R. Hee, G. M. Owen, E. A. Swanson, and J. G. Fujimoto, *Optics Letters* 19 (1994) 590.
- [2] A. D. Aguirre, P. Hsiung, T. H. Ko, I. Hartl, and J. G. Fujimoto, *Optics Letters* 28 (2003) 2064.
- [3] Y. Zhao, Z. Chen, C. Saxer, S. Xiang, J. F. de Boer, and J. S. Nelson, *Optics Letters* 25 (2000) 114.
- [4] V. Westphal, S. Yazdanfar, A. M. Rollins, and J. A. Izatt, *Optics Letters* 27 (2002) 34.
- [5] T. Xie, Z. Wang, and Y. Pan, *Optics Express* 11 (2003) 3210.
- [6] M. Pircher, E. Goetzinger, R. Leitgeb, and C. K. Hitzenberger, *Phys Med Biol* 49 (2004) 1257.
- [7] R. Huber, M. Wojtkowski, and J. G. Fujimoto, *Optics Express* 14 (2006) 3225.
- [8] R. Huber, D. C. Adler, and J. G. Fujimoto, *Optics Letters* 31 (2006) 2975.
- [9] D. C. Adler, R. Huber, and J. G. Fujimoto, *Opt Lett* 32 (2007) 626.

## 4.2 Line-Scanning Optical Coherence Microscopy (OCM)

Optical coherence tomography (OCT) is an emerging medical imaging technology which can generate high-resolution, cross-sectional imaging of biological tissues in situ and in real time [1]. OCT functions as a type of optical biopsy to enable imaging of tissue microstructure with a resolution approaching that of histopathology, without the need to excise tissue specimens. However, high resolutions in both axial and transverse dimensions are necessary to resolve subtle morphological alterations for diagnosis of diseases such as cancer. Ultrahigh axial resolution in OCT can be achieved using broadband light sources [2], however high transverse resolutions are also required for cellular imaging. Optical coherence microscopy (OCM) uses high numerical aperture (NA) focusing to generate en face images with cellular level, transverse resolution [3]. OCM has been implemented by raster scanning a tightly focused beam [4]. Alternately, full-field OCT uses a Linnik-type interferometer with full-field illumination and CCD detection to achieve cellular resolution en face imaging [5]. Full-field OCT has excellent image quality and uses low-cost, thermal light sources. However, full-field illumination and detection is sensitive to phase averaging effects from sample motion and has increased scattered light compared with single-point, beam-scanning illumination.

We have developed line-scanning OCM, a new technique for cellular-resolution en face imaging. Figure 4.7(A) shows the schematic of the experimental setup. The line-scanning OCM system was based on a Linnik-type interference microscope with two identical microscope objectives (10x, 0.3 NA, water immersion, working distance 3.1 mm, infinity corrected) in the sample and reference arms. A compact, commercially available broadband Ti:Sapphire laser (Femtolaser Produktions GmbH) was used to generate a spectral bandwidth of 80 nm FWHM at a center wavelength of 820 nm. 50 mW average power was coupled into a single-mode fiber and delivered to the interferometer, which gave 25 mW line illumination on the sample. Since the illumination was a line, the exposure is significantly less than for point illumination. Line illumination was achieved using a spherical focusing lens and a plano-concave cylindrical lens (CL). The reference arm power was controlled by a neutral density filter, and a glass blank used in the sample arm to balance dispersion. Light from the sample and reference arms were recombined by the beam splitter and imaged onto a high speed, 1024 pixel line scan CCD camera (Atmel) with 12-bit A/D range. The interference signal was modulated by actuating the reference mirror

with a piezoelectric transducer (PZT), using four integrating-bucket technique with sinusoidal phase modulation to extract the interference component [6]. En face images were generated by transversely scanning the sample orthogonal to the illumination line with a precision translation stage. A series of en face images at different depths were also acquired by translating the sample in the axial direction.

The line scan camera was read at  $\sim 52$  Mpixel/s, corresponding to an  $f = 51.6$  kHz line acquisition rate, while the PZT was sinusoidally actuated at  $f / 4 = 12.9$  kHz and synchronized to the camera frame grabber. Typically, 120 line scans, or 30 from each of the four-quadrant integrating-buckets, were averaged to increase the signal-to-noise ratio, and resulted in a line acquisition speed of 430 lines/second. Each en face image consisted of 256 lines and was acquired in 0.6 second. The magnification and the scanning speed of the system were chosen such that the image size is  $256 \times 256$  pixels over the field of view (FOV) of  $256 \mu\text{m} \times 256 \mu\text{m}$ .

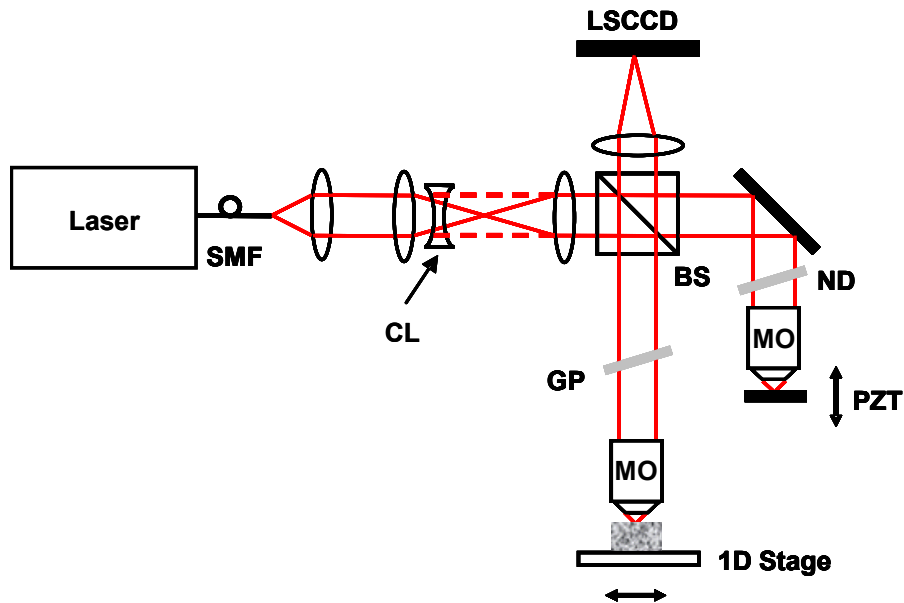


**Figure 4.7.** Schematic of line-scanning optical coherence microscopy (OCM) imaging system. A broadband Ti:Sapphire laser is used as the light source. SMF: single mode fiber; CL: cylindrical lens; BS: beam splitter; MO: microscope objectives; M: mirror; ND: neutral density filter; GP: glass plate for dispersion compensation; PZT: piezoelectric transducer; LSCCD: line scan CCD camera.

The axial point spread function of the system was measured by translating a mirror in the sample arm as was  $\sim 3 \mu\text{m}$  in water, as shown in Figure 4.8(A). The axial point spread function is a combination of the coherence gate and confocal gate. Figure 4.8(B) shows an en face OCM image of a USAF target in the sample arm. The smallest group 7, element 6 bars were resolved, indicating a  $\sim 2 \mu\text{m}$  transverse resolution. The detection sensitivity of the system was measured to be 93 dB with 30 line averages, which corresponds to an imaging speed of  $\sim 2$  Hz.

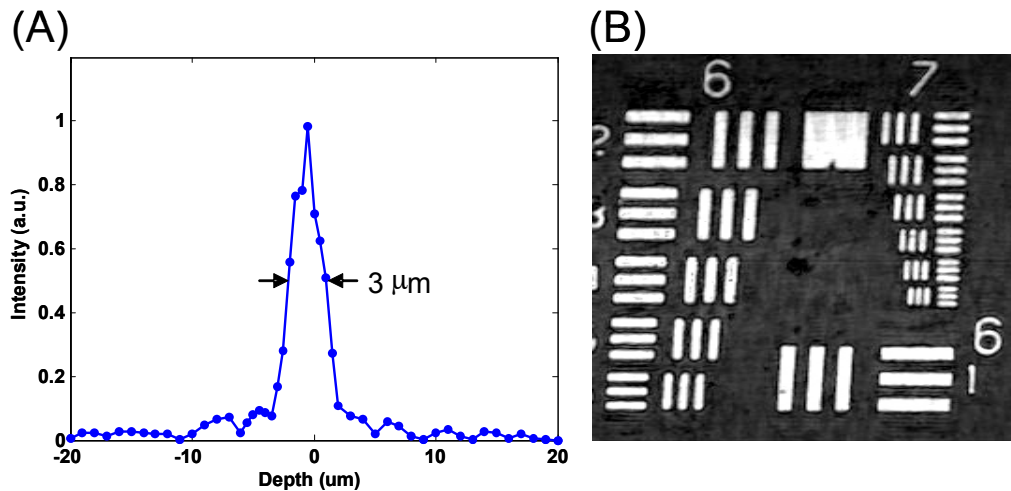


**Figure 4.8.** (A) Measured axial point spread function with 3  $\mu\text{m}$  FWHM in water. (B) Coherence gated image of a USAF resolution target demonstrating a transverse resolution of  $\sim 2 \mu\text{m}$ .

Figure 4.9 shows representative images of a human colon specimen *ex vivo*. Specimens were preserved in the phosphate-buffered saline (PBS) and imaged within 4 hours after excision. During the imaging, PBS was used with the immersion microscope objective to maintain tissue hydration and facilitate index matching. En face images at 100  $\mu\text{m}$  and 150  $\mu\text{m}$  depths are shown in Figure 4.9(A) and 4.9(B). Detailed structures such as the crypt lumens, the epithelium, and lamina propria were clearly visualized. Individual goblet cells containing translucent mucin could be seen within the epithelium. Deeper sections of crypts at 150  $\mu\text{m}$  depth show narrower lumens than those at 100  $\mu\text{m}$  depth. These images demonstrate the high-resolution, cellular level imaging capability of the line scan OCM. After imaging, specimens were fixed in formalin and processed for histology. Figure 4.9(C) shows representative en face histology stained with H&E.

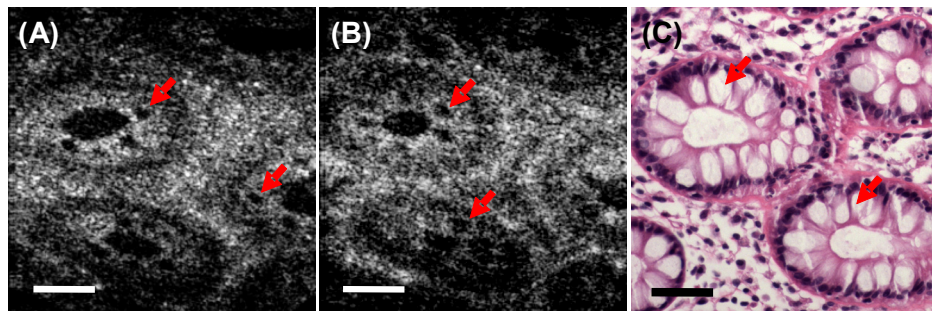


**Figure 4.9.** En face images of human colon specimen *ex vivo* acquired using line-scanning OCM at depths of (A) 100  $\mu\text{m}$  and (B) 150  $\mu\text{m}$ . Colonic crypt structures can be visualized with individual goblet cells (red arrows). (C) Representative en face histology of the colon. For all images, bar = 50  $\mu\text{m}$ .

Compared with full-field OCT, line scan OCM has the advantage of reducing the amount of incoherent scattered light and pixel cross talk in scattering tissues and therefore achieves higher detection sensitivity compared with full-field illumination. The use of line scan cameras promises to enable *in vivo* imaging by reducing sensitivity to sample motion compared with full-field camera detection because phase sensitive information is acquired rapidly, before phase averaging effects

can occur. The imaging speed could be increased up to ~8 frames per second by using two integrating-bucket demodulation and a higher speed, 512-pixel camera. Therefore, image speeds should be sufficient for in vivo imaging. Future work will include the development of a scanning mirror system to scan the line illumination and detection, and the development of miniaturized scanner for endoscopic applications.

## References

- [1] D. Huang, E. A. Swanson, C. P. Lin, J. S. Schuman, W. G. Stinson, W. Chang, M. R. Hee, T. Flotte, K. Gregory, C. A. Puliafito, and J. G. Fujimoto, "Optical Coherence Tomography," *Science*, vol. 254, pp. 1178-1181, Nov 22 1991.
- [2] W. Drexler, U. Morgner, F. X. Kartner, C. Pitris, S. A. Boppart, X. D. Li, E. P. Ippen, and J. G. Fujimoto, "In vivo ultrahigh-resolution optical coherence tomography," *Optics Letters*, vol. 24, pp. 1221-1223, 1 Sept. 1999.
- [3] J. A. Izatt, M. R. Hee, G. M. Owen, E. A. Swanson, and J. G. Fujimoto, "Optical coherence microscopy in scattering media," *Optics Letters*, vol. 19, pp. 590-2, 1994/04/15 1994.
- [4] A. D. Aguirre, P. Hsiung, T. H. Ko, I. Hartl, and J. G. Fujimoto, "High-resolution optical coherence microscopy for high-speed, in vivo cellular imaging," *Optics Letters*, vol. 28, pp. 2064-2066, Nov 1 2003.
- [5] A. Dubois, K. Grieve, G. Moneron, R. Lecaque, L. Vabre, and C. Boccara, "Ultrahigh-resolution full-field optical coherence tomography," *Appl Opt*, vol. 43, pp. 2874-83, May 10 2004.
- [6] A. Dubois, "Phase-map measurements by interferometry with sinusoidal phase modulation and four integrating buckets," *Journal of the Optical Society of America a-Optics Image Science and Vision*, vol. 18, pp. 1972-1979, Aug 2001.

## 5. Functional Brain Imaging with OCT

### Sponsors

Air Force Office of Scientific Research FA9550-040-1-0011, FA9550-040-1-0046  
National Institutes of Health R01-EY11289-20, NIH-5-R01-CA75289-08  
National Science Foundation BES-0522845, BES-0119494

### Project Staff

Dr. Yu Chen, Aaron D. Aguirre, Professor James G. Fujimoto, Dr. David A. Boas (MGH), Lana Ruvinskaya (MGH), Dr. Anna Devor (MGH)

Noninvasive imaging of neuronal response to external stimuli is an active area of research. Among available methods, hemodynamic techniques, including positron emission tomography (PET), single-photon emission computed tomography (SPECT), and functional magnetic resonance imaging (fMRI), have proven useful for visualizing spatial localization of neural activity, but they have limited temporal resolution. In contrast, electrophysiological techniques, such as electroencephalography (EEG), can measure neural responses on the millisecond time scale, but with limited spatial resolution. Optical methods can offer both high spatial and high temporal resolutions and are therefore particularly promising for making full-field measurements of hemodynamic, metabolic, and neuronal activities in vivo. Currently most of the optical intrinsic signal imaging (OISI) methods present the two-dimensional en face maps of brain activation, and do not provide depth resolution of the functional response [1, 2]. Depth-resolved images can be achieved by multiphoton fluorescence microscopy [3] and laminar optical tomography [4]. Optical coherence tomography (OCT) is another promising method for high-resolution, depth-resolved imaging in the cerebral cortex [5-7].

In collaboration with Dr. David Boas at the Martinos Center for Biomedical Imaging of the Massachusetts General Hospital and Harvard Medical School, we are investigating OCT for measuring subsurface scattering changes due to functional activation in the rat somatosensory cortex. Simultaneous OISI and OCT imaging were performed on anesthetized rat with thinned-skull preparation [7]. Forepaw stimulation is performed using 20-second stimulation blocks. Each block consists of 1 second of pre-stimulus period followed by 4 seconds of stimulation with  $\sim 1.8$  mA pulses at 3 Hz. A 15-second post-stimulus period is then provided to allow full recovery of the excitable tissues to baseline. The stimulus block is repeated 60 times during data acquisition over a 20-minute period. Block averaged signals are then computed to reduce the effects of physiologic noise in the measurements. Functional OCT signals are presented as the fractional changes by normalizing signals all time points to the averaged signal levels in the corresponding pixels at baseline (pre-stimulus period).

Figure 5.1 highlights the typical functional OCT imaging of rat somatosensory cortex. The averaged functional image from the time window 4-7 seconds (around the peak of maximal activation) is shown in Figure 5.1(A). Both positive and negative signal changes are observed. Warm colors at the red and yellow end of the colormap represent positive signal changes, while cool colors at the blue end represent negative changes. The functional OCT image reveals highly localized, distinct “hot spots” of activation in the cortex. Figure 5.1(B) shows a magnified view of the temporal sequence for the corresponding boxed region in Figure 5.1(A). Time point 0 represents the baseline. At 4 and 6 seconds, bright areas of signal change emerge and subsequently return to baseline after 8 and 10 seconds. Figure 5.1(C) shows a second magnified region of the functional OCT image. The colormap has been switched to gray scale, with positive signal change in black, to allow clear color-coded delineations of regions of interest (ROI). The corresponding temporal sequences of activation for the boxed regions in Figure 5.1(C) are provided in Figure 5.1(D). The OCT functional signal timecourses reveal clear increases and decreases that deviate from baseline, reach a peak near the cessation of the stimulus, and then gradually return to baseline.

Understanding the exact etiology and timecourse of the OCT functional signal will require additional investigation. The results presented here have been validated in more than 10 animals to date, and in each case, a robust and highly localized OCT response is seen corresponding with the hemodynamic response measured by OISI. The presence of positive and negative going OCT signals and the relatively speckled appearance of the response under differential signal analysis implicate swelling mechanisms as an important contributor. Furthermore, the presence of highly localized regions of activation in the cortex suggests that localized swelling or vascular dilation, rather than simply bulk brain swelling, is contributing.

A closer look at the timecourses for different ROIs reveals different temporal responses. For example, Figure 5.2 shows difference temporal response for two specific ROIs. The blue region in the cortex (Figure 5.2(A)) shows a timecourse correlating well with the stimulation pattern (Figure 5.2(B)). The functional signal increase when the stimulation starts at 1 second, and reach the apex at the end of the stimulation (5 second). In contrast, the red region indicating a large vessel from the structural image in Figure 5.2(A) shows a delayed response in the timecourse with respect to the stimulation pattern (Figure 5.2(B)). This phenomenon could be the indication of retrograde vessel dilation [8], where the smaller vessels, such as the capillary, response in synchrony with the neuronal activation. In addition, the vasodilatation is transmitted up-stream to the arterioles.

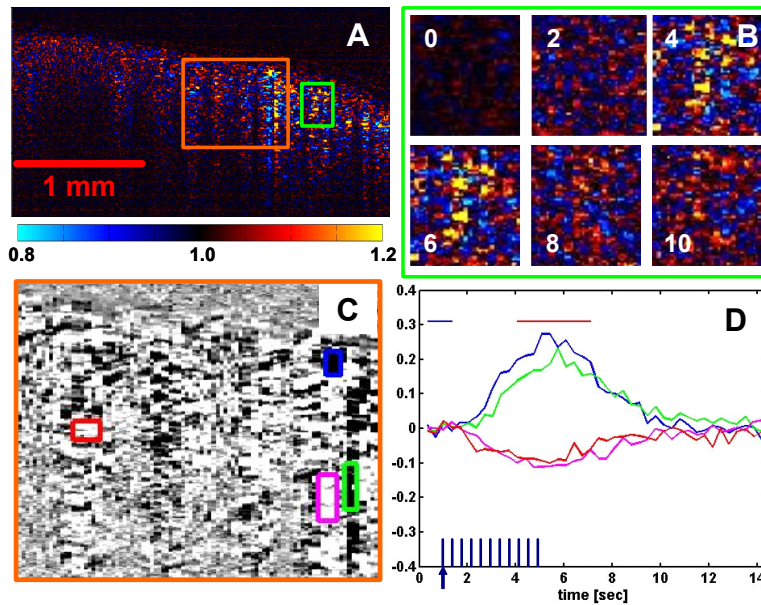


**Figure 5.1.** Functional OCT measurements in the rat cortex. A fractional change map (A) demonstrates the presence of positive (warm colors) and negative (cool colors) changes in OCT signals during stimulation. Temporal sequences (B) reveal the presence of highly localized regions of activation in the cortex that persist throughout stimulation. Further analysis of the localized regions of interest (C,D) shows a functional OCT timecourse that correlates well with that of the intrinsic hemodynamic optical signal but with both positive and negative going responses. The horizontal bars in (D) indicate the time windows of interest used to generate the functional map (A, B, C).

To appreciate the spatial correlation of the time lags, we performed a cross-correlation analysis for all the timecourses at every spatial location. We used the averaged OISI signal as the standard and calculated the shift of the peak (an indication of time lag) for individual pixel. Figure 5.3(A) displays the spatially resolved time lags overlay with the OCT structural image. Different colors indicate different time lags with respect to the averaged OISI response, which synchronizes with the stimulation pattern. The majority of the cortex region shows the response close to the stimulation pattern (with time lag within 1s). Some “hot spots” exhibit delayed responses, which might be an indication of arteries or arterioles. A histogram of the time lag is presented in Figure 5.3(B), where most of the pixels reside near time lag ~ 0s, but there is a smaller peak of time lag centered around 2s.

Future study will focus on careful characterization of the response, including the use of techniques such as three-dimensional and Doppler OCT. With further investigation, this technique has potential to become a new tool for basic and applied neuroscience research in animal models.

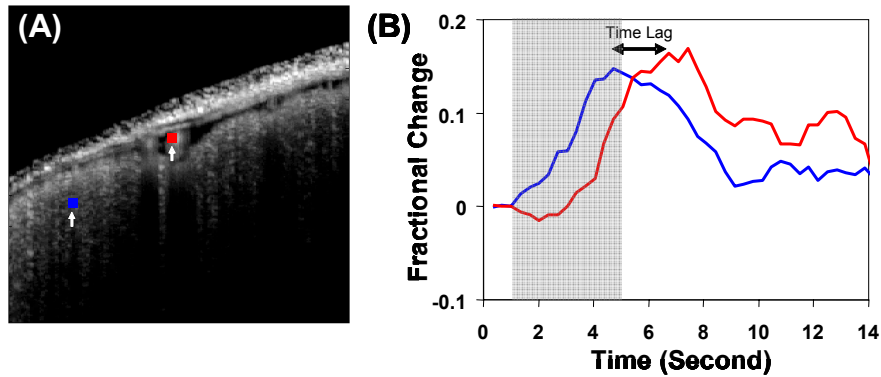


**Figure 5.2.** (A) Structural OCT image of rat brain. Red and blue regions denote the larger pia artery, and the smaller arterioles in the cortex region respectively. (B) Timecourses of functional activation from these two regions. The blue curve is from the region denoted by blue color (cortex), and the red curve is from the region denoted by red color (pia artery).

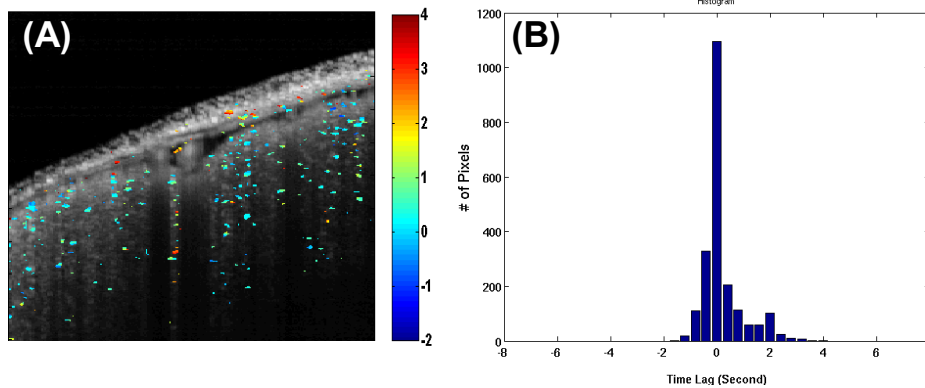


**Figure 5.3.** (A) Structural OCT image overlaid with the time lags of different activation loci. The time lags are color-coded (unit: second). (B) Histogram of the temporal distribution of the time lags for different loci.

## References

- [1] A. K. Dunn, A. Devor, A. M. Dale, and D. A. Boas, "Spatial extent of oxygen metabolism and hemodynamic changes during functional activation of the rat somatosensory cortex," *Neuroimage*, vol. 27, pp. 279-290, Aug 15 2005.
- [2] S. A. Sheth, M. Nemoto, M. W. Guio, M. A. Walker, and A. W. Toga, "Spatiotemporal evolution of functional hemodynamic changes and their relationship to neuronal activity," *Journal of Cerebral Blood Flow and Metabolism*, vol. 25, pp. 830-841, Jul 2005.
- [3] D. Kleinfeld, P. P. Mitra, F. Helmchen, and W. Denk, "Fluctuations and stimulus-induced changes in blood flow observed in individual capillaries in layers 2 through 4 of rat neocortex," *Proceedings of the National Academy of Sciences of the United States of America*, vol. 95, pp. 15741-15746, Dec 22 1998.
- [4] E. M. C. Hillman, A. Devor, M. B. Bouchard, A. K. Dunn, G. W. Krauss, J. Skoch, B. J. Bacskai, A. M. Dale, and D. A. Boas, "Depth-resolved optical imaging and microscopy of vascular compartment dynamics during somatosensory stimulation," *Neuroimage*, vol. 35, pp. 89-104, Mar 2007.

- [5] R. U. Maheswari, H. Takaoka, H. Kadono, R. Homma, and M. Tanifuji, "Novel functional imaging technique from brain surface with optical coherence tomography enabling visualization of depth resolved functional structure in vivo," *Journal of neuroscience methods*, vol. 124, pp. 83-92, Mar 30 2003.
- [6] J. Seki, Y. Satomura, Y. Ooi, T. Yanagida, and A. Seiyama, "Velocity profiles in the rat cerebral microvessels measured by optical coherence tomography," *Clinical Hemorheology and Microcirculation*, vol. 34, pp. 233-239, 2006.
- [7] A. D. Aguirre, Y. Chen, J. G. Fujimoto, L. Ruvinskaya, A. Devor, and D. A. Boas, "Depth-resolved imaging of functional activation in the rat cerebral cortex using optical coherence tomography," *Optics Letters*, vol. 31, pp. 3459-3461, Dec 1 2006.
- [8] H. Girouard and C. Iadecola, "Neurovascular coupling in the normal brain and in hypertension, stroke, and Alzheimer disease," *Journal of Applied Physiology*, vol. 100, pp. 328-335, Jan 2006.